Praseodymia on non-passivated and passivated Si(111) surfaces

Dissertation (kumulativ)

zur Erlangung des Grades eines
Doktors der Naturwissenschaften (Dr. rer. nat.)

dem Fachbereich Physik der Universität Osnabrück
vorgelegt von

Sebastian Gevers, Dipl. Phys.

Osnabrück, Dezember 2010

Contents

1 Introduction

Rare earth oxides (REOs) take up an important role in today's research efforts since they are of interest in many fields of technology. They are particularly discussed for applications in microelectronics [1], electro-optics [2] as well as heterogeneous catalysis [3, 4].

In this context, praseodymia is of special interest for several reasons. It is an ideal candidate for applications in heterogeneous catalysis because it is known to be catalytically active in a variety of reactions [3, 5, 6, 7]. Its high oxygen mobility and storage capability [8] are especially advantageous for catalytic applications according to the Mars-van-Krevelen mechanism. Furthermore, ultra-thin crystalline praseodymia films with high quality can be grown on Si substrates. The structure of these film can be influenced afterwards by post deposition annealing (PDA) processes so that films with hexagonal [9], bixbyite [10], or fluorite [11] structure can be generated. These films are discussed as highly functional buffer layers to integrate alternative semiconductors on the technologically dominating Si platform [12]. Here, especially germanium-on-insulator (GeOI) systems are promising to boost the sub-45 nm complementary metal oxide (CMOS) technologies [13]. These composite GeOI systems are also interesting for the global and cost effective integration of III-V optoelectronic materials like GaAs on the Si wafer platform [14].

In all mentioned applications, PDA of the praseodymia films is necessary either to drive the catalytic reactions [15] or to grow for example crystalline Ge films on top of them [16]. These PDA processes are accompanied by gradual changes of the oxygen content within the oxide films and by the undesired formation of an amorphous Pr-silicate interface layer. Those effects have a strong impact on the catalytic activity [17] as well as the electrical [18] and structural properties [19], which may have a negative influence on the desired applications. Therefore, it is important to investigate the PDA processes of praseodymia films and to establish new techniques to prevent the interface formation. Regarding the catalytic applications, it is further interesting to obtain praseodymia films with the highest oxidation state (PrO_2) to provide a maximum of mobile lattice oxygen for the catalytic reactions.

The theoretical background, the investigated materials and the experimental setup of the presented work are introduced in chapters 2, 3 and 4. A detailed classification of the results within the scientific context is given in chapter 5. These results are divided into three main topics. In the first part, the PDA process of praseodymia films on Si(111) is presented. Here, PDA of films with fluorite structure at different temperature regions is described in chapters 6 and 7. In chapter 8, the PDA of films with bixbyite structure is discussed. The second part deals with the oxygen plasma treatment of praseodymia films on Si(111) to obtain the highest oxidation state. First, a summary of former results from this new technique using X-ray photoelectron spectroscopy and low energy electron diffraction is given in chapter 9. This is followed by the results of X-ray diffraction and X-ray reflection measurements in chapter 10 which were obtained in the course of the presented thesis. In the third part, a promising technique to prevent the silicate interface formation during epitaxy and PDA of praseodymia films is described and first results from this new technique using chlorine passivated substrates are presented. Finally, the most important results of this thesis and a brief outlook on future investigations are given in chapter 12.

2 Theoretical background

This chapter sheds light on the theoretical background of the methods and materials used in the presented thesis. First, the theoretical aspects of crystalline structures are presented. This is followed by the theory of X-ray and electron diffraction as well as X-ray reflection and X-ray standing waves. A brief introduction into the theory of X-ray spectroscopy is given at the end of this chapter.

2.1 Crystal structures

Main subject of this thesis are crystalline films on single-crystalline substrates. Therefore, the principles of two- and three-dimensional lattices defining the obtained crystal structures are shown in the following chapter which are determined by bulk sensitive as well as surface sensitive methods.

2.1.1 Bulk lattices

Each crystal structure can be described as a set of atoms located upon each point of a mathematical lattice with long range order and symmetry. This arrangement forms a periodic array of identical structures being repeated in all spatial directions. The smallest periodically repeated structure is called unit cell. It is defined by its lattice parameters, the length of the cell edges and the angles between them (cf. figure 2.1). The positions of the atoms inside the unit cell are described by the set of atomic positions which have their origin in a lattice point. The whole crystal structure can be built up with a single unit cell and translation operations

$$\boldsymbol{T} = n_1\boldsymbol{a} + n_2\boldsymbol{b} + n_3\boldsymbol{c} \ , \tag{2.1}$$

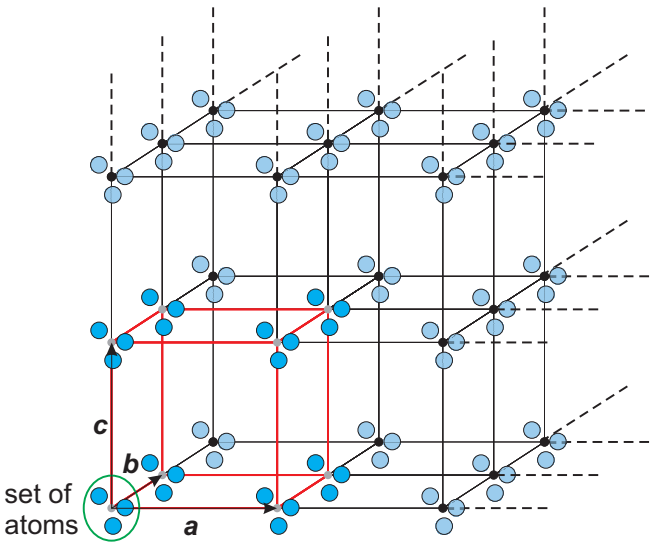

Figure 2.1: Elements und arrangements of the crystal structure. A set of atoms (green oval) is located on each point of the crystal lattice (black dots) which is repeated in every spatial direction. The whole crystal structure can be described with a single unit cell (red lines) and a set of fundamental translation vectors $\boldsymbol{a}$, $\boldsymbol{b}$ and $\boldsymbol{c}$ (arrows).

with fundamental translation vectors $\boldsymbol{a}$, $\boldsymbol{b}$ and $\boldsymbol{c}$ and n_1, n_2, $n_3 \in \mathbb{Z}$. Furthermore, the crystal

lattice has to be invariant against translation operations so that

$$\boldsymbol{r} = \boldsymbol{r'} + \boldsymbol{T} \ . \tag{2.2}$$

This means, that a position vector of a lattice point $\boldsymbol{r}$ can be obtained from any other position vector $\boldsymbol{r'}$ and a corresponding translation operation.

Including rotation operations, BRAVAIS showed in 1894 that only 14 different crystal lattices are possible. These BRAVAIS-lattices can be assigned by their symmetry properties to seven different crystal systems (cf. figure 2.2). Within these systems crystal lattice planes are

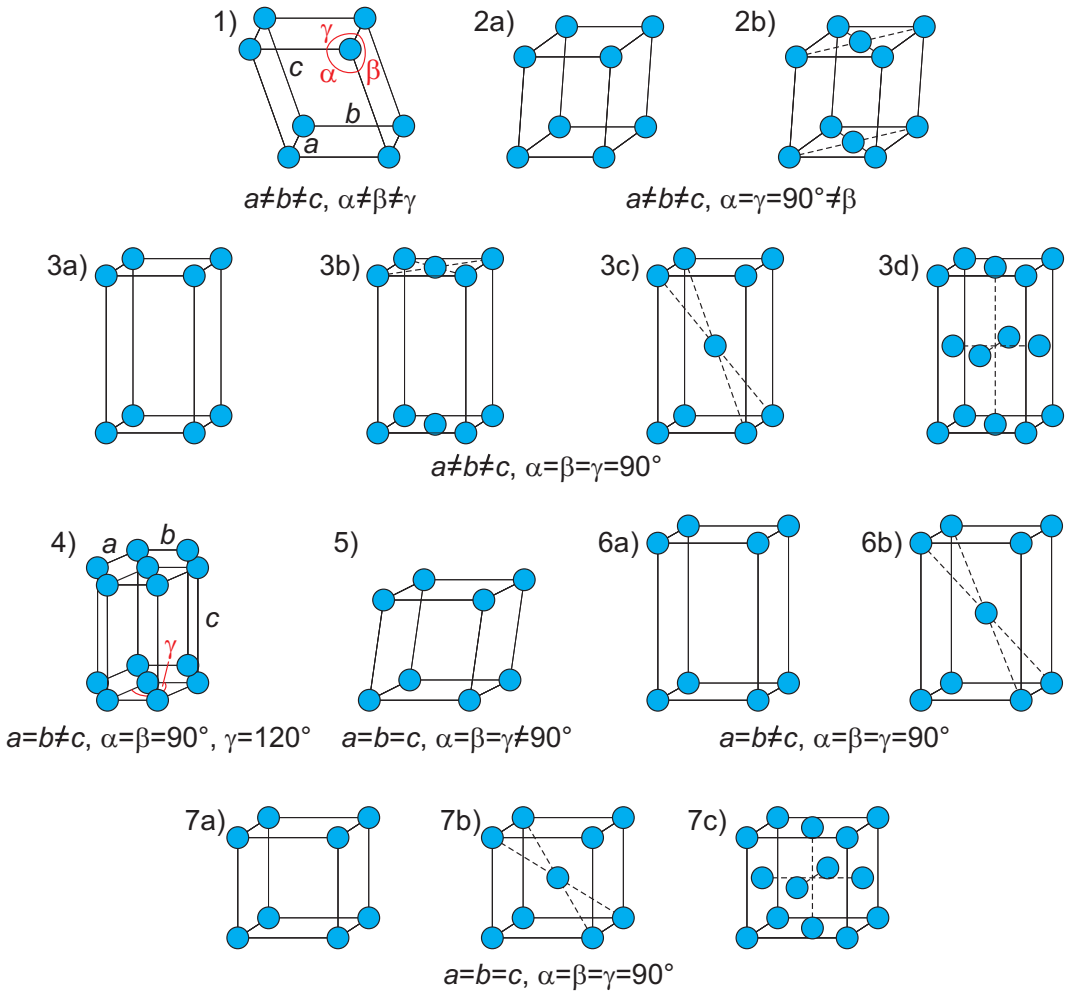

Figure 2.2: The 14 three-dimensional BRAVAIS-lattices with lattice parameters a, b and c and the corresponding angles α, β and γ. (1) triclinic, (2a) simple monoclinic, (2b) base-centered monoclinic, (3a) simple orthorombic, (3b) base-centered orthorombic, (3c) body-centered orthorhombic, (3d) face-centered orthorombic, (4) hexagonal, (5) rhombohedral, (6a) simple tetragonal, (6b) body-centered tetragonal, (7a) simple cubic, (7b) body-centered cubic, (7c) face-centered cubic.

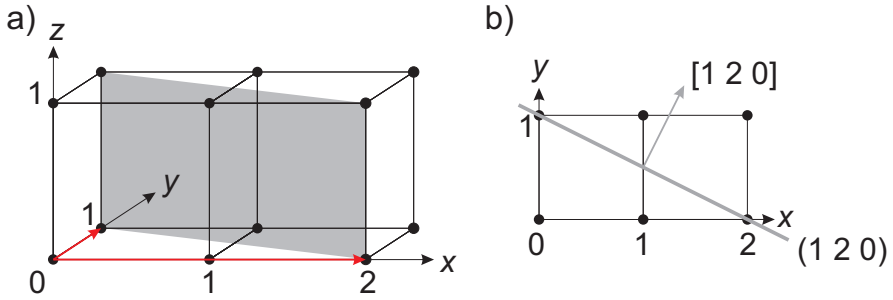

Figure 2.3: (a) An exemplary crystal plane parallel to the z-axis, which intersects the lateral axis at $(x, y) = (2, 1)$ (red arrows). (b) Denotation of the crystal plane and the corresponding crystal direction with MILLER indices.

defined by three lattice points with the integer MILLER indices (h, k, l). These are given by the intersection points of the crystal planes with the three crystal axis of (x, y, z). The values are inversed and multiplicated with the lowest common multiple of the denominator n_{comm}.

Figure 2.3 shows a simple example how the Miller indices are obtained. The crystal plane intersects the lateral crystal axis at $(x, y) = (2, 1)$, the vertical axis is parallel to the crystal plane. Therefore, no intersection point is obtained so that $z = \infty$. The Miller indices are given as

$$(h, k, l) = (1/x, 1/y, 1/z) \cdot n_{\text{comm}} = (1/2, 1, 0) \cdot 2 = (1, 2, 0) \equiv (1\ 2\ 0)\ . \tag{2.3}$$

Directions within the crystal lattices are indicated by vectors perpendicular to the corresponding lattice planes and labeled with square brackets (cf. figure 2.3(b)).

2.1.2 Surface lattices

The physical and chemical properties of an infinite crystal are identical in every point of the crystal structure. By cleaving such an ideal crystal, two semi-infinite crystals with unsaturated atomic bonds at the cleaving edges are obtained. In these areas, the properties of the topmost atomic layers are necessarily different compared to the bulk structure. Therefore, this region is defined as the surface of the crystal. The region beyond the surface, where the properties are again identical with the bulk properties, is called substrate.

According to three-dimensional crystal structures, the surface is described with a set of atoms located at the points of a *two*-dimensional lattice. The corresponding translation operations are

$$\boldsymbol{T} = n_1\boldsymbol{a} + n_2\boldsymbol{b}\ . \tag{2.4}$$

In contrast to three-dimensional crystal structures, only five BRAVAIS-lattices are possible in two dimensions, which are presented in figure 2.4. However, reconstruction processes occur at the surface if the bulk structure is not energetically favorable due to the unsaturated atomic bonds. In this case, the surface structure is no longer identical with the substrate structure

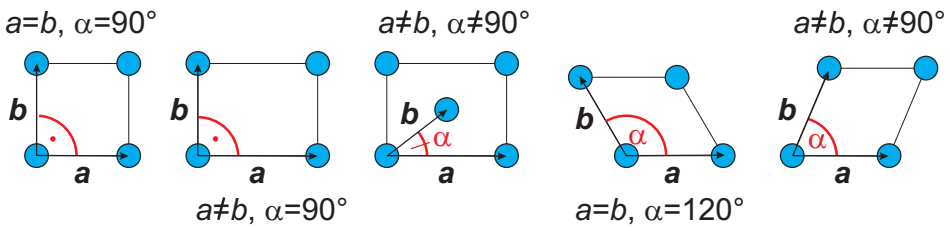

Figure 2.4: The five two-dimensional BRAVAIS-lattices. Square, rectangular, centered rectangular, hexagonal, and oblique. The primitive translation vectors the angle between them are denoted as $\boldsymbol{a}$, $\boldsymbol{b}$ and *alpha*.

and a so-called superstructure is generated. It is useful to introduce two different structures with fundamental vectors ($\boldsymbol{a}$,$\boldsymbol{b}$) and ($\boldsymbol{a'}$,$\boldsymbol{b'}$) for substrate and surface as well as appropriate translation operations

$$\boldsymbol{T}_{\text{substrate}} = n_1\boldsymbol{a} + n_2\boldsymbol{b} \tag{2.5}$$

and

$$\boldsymbol{T}_{\text{surface}} = n'_1\boldsymbol{a'} + n'_2\boldsymbol{b'} \ . \tag{2.6}$$

To describe these reconstructed surfaces, two nomenclatures were developed which establish a relation between substrate and surface lattices. Here, WOOD's notation [20] provides a simple way to describe these structures giving the expression

$$R\,(hkl)\left(\frac{a'}{a} \times \frac{b'}{b}\right) / \,\alpha \ , \tag{2.7}$$

with the substrate material R, the MILLER indices (hkl) of the crystal plane parallel to the surface and the angle α if substrate and surface vectors are rotated against each other.

WOOD's notation is inapplicable if substrate and surface lattices are incommensurable, which means that the angles between the fundamental vectors of substrate and surface are not identical. In this case, the matrix notation according to PARK and MADDEN [21] has to be used. The fundamental vectors of the surface are attached to the fundamental vectors of the substrate via

$$\boldsymbol{a'} = m_{11}\boldsymbol{a} + m_{12}\boldsymbol{b} \tag{2.8}$$

and

$$\boldsymbol{b'} = m_{21}\boldsymbol{a} + m_{22}\boldsymbol{b} \tag{2.9}$$

with $m_{ij} \in \mathbb{Z}$. This can also be expressed in matrix notation as

$$\begin{pmatrix} \boldsymbol{a'} \\ \boldsymbol{b'} \end{pmatrix} = \begin{pmatrix} m_{11} & m_{12} \\ m_{21} & m_{22} \end{pmatrix} \begin{pmatrix} \boldsymbol{a} \\ \boldsymbol{b} \end{pmatrix} \ . \tag{2.10}$$

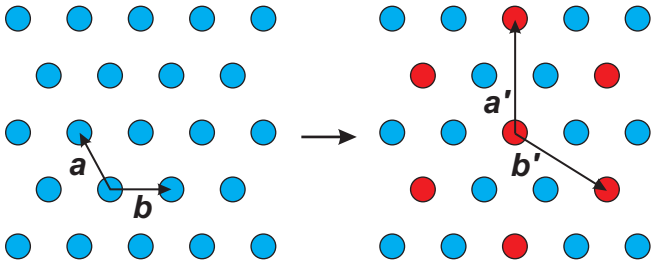

Figure 2.5: Surface reconstruction of Si(111) by adsorption of boron (red atoms). The reconstruction is related to the primitive translation vectors $\boldsymbol{a}$ and $\boldsymbol{b}$ of the *unreconstructed* Si(111) surface.

Reconstruction of the surface also occurs if additional foreign atoms are adsorbed at the surface. These reconstructions can be described with the notations mentioned above, but they are not called superstructures since they are not induced by simply generating a surface from a bulk material. In WOOD's notation, this is indicated by mentioning the adsorbed material at the end of the expression. In this case, the notations are always related to the *unreconstructed* substrate structure.

By way of illustration, both notations are shown in the following for the boron induced reconstruction of the Si(111) surface (cf. figure 2.5). In WOOD's notation the obtained surface structure can be written as

$$\mathrm{Si}(111)(\sqrt{3}\times\sqrt{3})/R30^\circ - \mathrm{B} \tag{2.11}$$

and the matrix notation gives

$$\begin{pmatrix} \boldsymbol{a'} \\ \boldsymbol{b'} \end{pmatrix} = \begin{pmatrix} 2 & 1 \\ 1 & -1 \end{pmatrix} \begin{pmatrix} \boldsymbol{a} \\ \boldsymbol{b} \end{pmatrix} . \tag{2.12}$$

2.2 Principles of diffraction

In general, diffraction occurs if wave fronts encounter an obstacle, which is for example a pinhole aperture. If the pinhole is assumed to be a mathematical point, a secondary radial wave (HUYGENS wavelet) is formed here according to the HUYGENS-FRESNEL principle (cf. figure 2.6(a)). If the pinhole size is increased, additional wavelets emerge from each point of the wavefront within the aperture. Subsequent propagation and addition of all these radial waves form a new wavefront (cf. figure 2.6(b)). In this case, interference effects occur since the individual waves are phase-shifted to each other depending on the propagation direction. The interference between two secondary waves is constructive if the phase-shift is an integral multiple of the wavelength $n \cdot \lambda$ and destructive if it is a half-integral multiple $n/2 \cdot \lambda$.

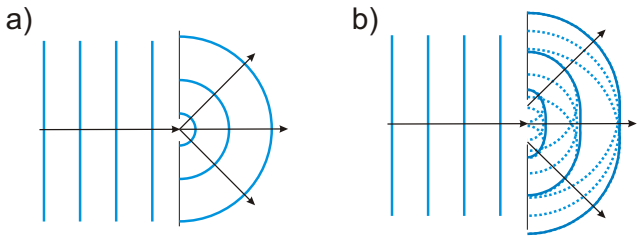

Figure 2.6: Diffraction of a wave (maxima are indicated by blue lines) passing through a pinhole aperture. (a) The pinhole is assumed to be a mathematical point and (b) the pinhole has a finite size (the HUYGENS wavelets are dotted and the resulting wavefront is indicated with solid lines).

2.3 X-ray diffraction

X-ray diffraction is used to investigate the structure of solid state materials. Here, X-ray waves are diffracted at electrons which are bound at the atoms in a solid. A random distribution of these atoms, however, lead to a white noise signal, since no defined phase-dependence is obtained between the secondary X-ray waves. Therefore, periodically distributed atoms as they can be found in crystalline structures (cf. chapter 2.1) are necessary to observe constructive interference. Depending on the size and orientation of these structures characteristic diffraction patterns occur. The wavelength of the X-ray photons has to be of the same order as the structures of the investigated crystalline materials. Since the distances between atoms in a solid are in the order of $1 \cdot 10^{-10}$m, the photon energies used to measure these crystalline structures are in the region of 10 keV, which corresponds to a wavelength of 1.24 Å.

2.3.1 Kinematic diffraction theory

The kinematic diffraction theory was developed to analyze the complex crystalline structures of real samples by calculation of the diffracted intensity from pre-defined model systems. It is based on three fundamental simplifications of the diffraction process.

1. Multiple scattering processes are neglected according to the first BORN approximation.
2. Absorption of the incident beam is ignored. This means that the intensity of the incident beam is the same for each crystalline layer independent of its position within the crystal. It is, however, important to note that this approximation is only true for thin film structures and sufficient high incident angles, since the X-ray photons exhibit large penetration depths (e.g. several μm for Si). In the presented work, this approximation can only be applied to the exclusion of the substrate. Furthermore, it is necessary that the X-ray photon energy does not correspond with the absorption edges of the investigated materials, which is also fulfilled by the investigated samples.
3. Refraction effects are not taken into account. This is because the material dependent change of the refractive index is rather small as mentioned in chapter 2.5.1. However,

this requires measurements at incident angles above the critical angle to avoid total reflection.

2.3.2 Scattering at a single electron

An electromagnetic wave is scattered at a single electron. According to the FRAUNHOFER diffraction theory, this wave can be considered as a plane wave, if the distance between the source of the wave and the electron is very large. In this case, the amplitude of the scattered plane wave can be written as

$$A(\boldsymbol{q}) = A_0 \frac{e^2}{m_e c^2} \frac{1}{R_0} \, e^{\,i \, \boldsymbol{q} \cdot \boldsymbol{r}_e} \,, \tag{2.13}$$

with the location of the electron $\boldsymbol{r}_e$, the distance between the detector and the electron R_0, the elementary charge e, the electron mass m_e and the speed of light c. The scattering vector $\boldsymbol{q}$ is the difference between incident wave vector and scattered wave vector. The constant parameters R_0, e, m_e and c are combined to a single parameter C so that

$$A(\boldsymbol{q}) = A_0 \, C \, e^{\,i \, \boldsymbol{q} \cdot \boldsymbol{r}_e} \tag{2.14}$$

according to the THOMSON formula.

2.3.3 Scattering at a single atom

To describe the scattering process at a single atom, it is necessary to summarize all waves diffracted at the electrons of the atom. In doing so, the phase relation of the individual waves has to be taken into account. Therefore, the amplitude of the scattered wave is given as

$$A(\boldsymbol{q}) = A_0 \, C \int d^3 r \rho\,(\boldsymbol{r}) \; e^{\,i \, \boldsymbol{q} \cdot \, (\boldsymbol{r}_a + \boldsymbol{r})} \tag{2.15}$$

with the position of the atom $\boldsymbol{r}_a$. The individual diffraction processes at the atomic electrons are considered by integrating the charge density distribution $\rho\,(\boldsymbol{r})$ over the volume of the atom. This part can be separated so that

$$A(\boldsymbol{q}) = A_0 \, C \, f(\boldsymbol{q}) \, e^{\,i \, \boldsymbol{q} \cdot \boldsymbol{r}_a} \;\;, \tag{2.16}$$

where the *atomic form factor* $f(q)$ corresponds to the Fourier transformed electron distribution of the atom and can be written as

$$f(\boldsymbol{q}) = \int d^3 r \rho\,(\boldsymbol{r}) \; e^{\,i \, \boldsymbol{q} \cdot \boldsymbol{r}} \;\;. \tag{2.17}$$

It only depends on the absolute scattering vector since the atomic electron shells are assumed to be of spherical symmetry. In this case, $f(q)$ can be described by four GAUSSIAN functions

$$f(q) = \sum_{i=1}^{4} a_i \;\; e^{\,-b_i \left(\frac{q}{4\pi}\right)^2} + c \;. \tag{2.18}$$

The corresponding values for the parameters a_i, b_i and c can be found in [22].

2.3.4 Scattering at a single unit cell

As described in chapter 2.1.1 unit cells are the smallest, periodically repeated structures in a crystalline system. To describe the scattering process at such a structure, the individual scattering processes at the atoms, on which the unit cell is build up, have to be summarized. Depending on the relative atomic positions and the scattering vector destructive and constructive interference occur due to the phase relation of the diffracted waves. Therefore, the total amplitude of the diffracted wave is written as

$$A(\boldsymbol{q}) = A_0 \, C \sum_{j=1}^{N} f_j \left(q\right) \, e^{\,i \, \boldsymbol{q} \cdot \, (\boldsymbol{r}_n + \boldsymbol{r}_j)} \tag{2.19}$$

$$= A_0 \, CF \left(\boldsymbol{q}\right) \, e^{\,i \, \boldsymbol{q} \cdot \boldsymbol{r}_n} \ . \tag{2.20}$$

Here, the number of atoms within the unit cell is given by N and the position of the atoms $\boldsymbol{r}_n + \boldsymbol{r}_j$ is composed of the unit cell position $\boldsymbol{r}_n$ and the atomic positions $\boldsymbol{r}_j$ in relation to the unit cell. Furthermore, the *structure factor*

$$F \left(\boldsymbol{q}\right) = \sum_{j=1}^{N} f_j \left(q\right) \, e^{\,i \, \boldsymbol{q} \cdot \boldsymbol{r}_j} \tag{2.21}$$

is the fourier transformed atomic distribution of the unit cell. It depends on the scattering *vector* $\boldsymbol{q}$ and not only on its absolute value, since the atomic distribution of the unit cell is not assumed to be spherically symmetric as it was assumed for the electron distribution of one single atom.

2.3.5 Diffraction at single crystalline structures

A crystalline structure consists of unit cells which are periodically repeated in all three spatial directions. The size of the periodic structures are in the range of the De-Broglie wavelength of X-ray photons. Therefore, the crystal lattice planes of the crystalline structure act as diffraction gratings and the Bragg condition plays an important role. This marks the transition from scattering to diffraction processes. Again, diffraction is described by phase correct summation of the individual waves diffracted at each unit cell. The total amplitude of the diffracted wave is

$$A \left(\boldsymbol{q}\right) = A_0 \, C \sum_{n} F_n \left(\boldsymbol{q}\right) \, e^{\,i \, \boldsymbol{q} \cdot \boldsymbol{r}_n} \ . \tag{2.22}$$

As mentioned in chapter 2.1.1, the periodic ordering of the crystalline structure can be described with simple translation operations. The diffracted amplitude of a crystal structure

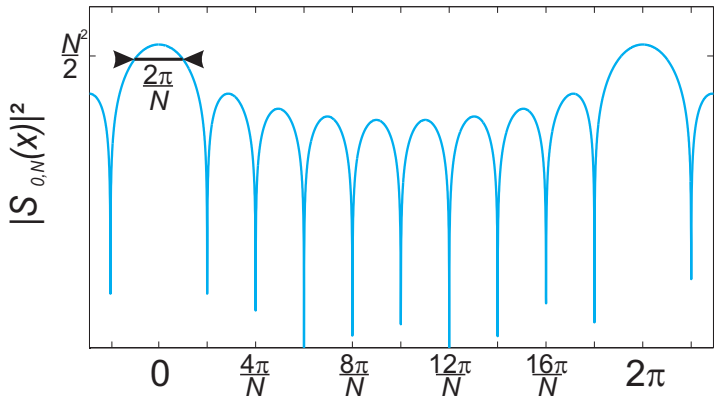

Figure 2.7: Intensity distribution obtained from diffraction at a grating with $N = 10$ slits, which are separated by 2π. $N-2$ additional oscillations (fringes) occur between the main diffraction peaks.

with a finite three dimensional array of N_1, N_2 and N_3 unit cells can be expressed as

$$A(\mathbf{q}) = A_0\, C\, F(\boldsymbol{q}) \sum_{n_1=0}^{N_1-1} \sum_{n_2=0}^{N_2-1} \sum_{n_3=0}^{N_3-1} e^{i\boldsymbol{q}\cdot\,(n_1\boldsymbol{a}+n_2\boldsymbol{b}+n_3\boldsymbol{c})} \tag{2.23}$$

$$= A_0\, C\, F(\boldsymbol{q}) \sum_{n_1=0}^{N_1-1} e^{i\,n_1\,\boldsymbol{q}\cdot\boldsymbol{a}} \sum_{n_2=0}^{N_2-1} e^{i\,n_2\,\boldsymbol{q}\cdot\boldsymbol{b}} \sum_{n_3=0}^{N_3-1} e^{i\,n_3\,\boldsymbol{q}\cdot\boldsymbol{c}}\ . \tag{2.24}$$

This can also be written as

$$A(\mathbf{q}) = A_0\, C\, F(\boldsymbol{q}) \cdot G(\boldsymbol{q}) \tag{2.25}$$

where $G(\boldsymbol{q})$ denotes the *lattice factor*.
The sum of the unit cells in one dimension corresponds to a geometric series, respectively. Assuming a crystal with a one dimensional array of unit cells, one has

$$S_{0,N}(\boldsymbol{q}) = \sum_{n=0}^{N-1} e^{i\,n\,\boldsymbol{q}\cdot\boldsymbol{a}} \tag{2.26}$$

$$= \frac{1-e^{i\,N\,\boldsymbol{q}\cdot\boldsymbol{a}}}{1-e^{i\,\boldsymbol{q}\cdot\boldsymbol{a}}}\ . \tag{2.27}$$

By simplifying this formula with $\boldsymbol{q}\cdot\boldsymbol{a} = x$, the square of the absolute intensity gives

$$|S_{0,N}|^2 = \frac{\sin^2(N\,x/2)}{\sin^2(x/2)}\ . \tag{2.28}$$

In general, this formula known as the N-slit function describes the intensity distribution of a wave diffracted at a grating. Figure 2.7 shows a typical diffraction pattern obtained from

a grating with $N = 10$ slits, which are separated by 2π. The distance of the slits can be determined from the distance between the main intensity maxima and the number of slits from its FWHM. Furthermore, additional characteristic intensity oscillations (fringes) occur between the main maxima. Their periodicity also gives information about the number of slits. Transfered to XRD measurements, mainly the distance and number of the unit cells in one dimension can be derived from these diffraction patterns.

Assuming an infinite number of scattering centers ($N_1 = N_2 = N_3 = \infty$), the N-slit function leads to a δ-like distribution of the diffracted intensity. In this case, however, the correct normalization is ignored so that the corresponding amplitude can be expressed as

$$A(\boldsymbol{q}) \propto A_0\, C\, F(\boldsymbol{q}) \sum_h \sum_k \sum_l \delta(\boldsymbol{q}\cdot\boldsymbol{a} - 2\pi\, h)\, \delta(\boldsymbol{q}\cdot\boldsymbol{b} - 2\pi\, k)\, \delta(\boldsymbol{q}\cdot\boldsymbol{c} - 2\pi\, l)\ . \tag{2.29}$$

Regarding the amplitude of an infinite crystal structure, the well known Laue conditions

$$\boldsymbol{q}\cdot\boldsymbol{a} = 2\pi\cdot h\ , \tag{2.30}$$

$$\boldsymbol{q}\cdot\boldsymbol{b} = 2\pi\cdot k \tag{2.31}$$

and

$$\boldsymbol{q}\cdot\boldsymbol{c} = 2\pi\cdot l \tag{2.32}$$

with integer h, k, and l values are obviously deduced. These conditions state that the diffracted intensity can only be observed if the scattering vector $\boldsymbol{q}$ is oriented in a specific direction in relation to the primitive vectors $\boldsymbol{a}$, $\boldsymbol{b}$ and $\boldsymbol{c}$ of the crystal lattice. No intensity is, however, observed if the scattering vector is otherwise oriented. The periodicity of the diffracted intensity is described in the *reciprocal* space, which can be generated by the primitive vectors a, b and c of the real space unit cell and its volume $V_E = \boldsymbol{a}\cdot(\boldsymbol{b}\times\boldsymbol{c})$. The resulting primitive vectors of the unit cell in reciprocal space are

$$\boldsymbol{a}^* = \frac{2\pi}{V_E}(\boldsymbol{b}\times\boldsymbol{c})\ , \tag{2.33}$$

$$\boldsymbol{b}^* = \frac{2\pi}{V_E}(\boldsymbol{c}\times\boldsymbol{a}) \tag{2.34}$$

and

$$\boldsymbol{c}^* = \frac{2\pi}{V_E}(\boldsymbol{a}\times\boldsymbol{b})\ . \tag{2.35}$$

According to the lattice vector in real space, the scattering vector in reciprocal space is a linear combination of these primitive vectors and can be written as

$$\boldsymbol{q} = H\,\boldsymbol{a}^* + K\,\boldsymbol{b}^* + L\,\boldsymbol{c}^*\ . \tag{2.36}$$

Using the Laue conditions, one can determine the periodicity of the scattering centers in real space from the periodicity of the diffracted intensity in the reciprocal space. It is further notable that the intensity maxima are also called Bragg peaks, because the Bragg condition is fulfilled for the respective scattering vectors, too.

2.3.6 Diffraction at a semi-infinite crystal

The theoretical idea of infinite crystals is insufficient to model the diffracted intensity distribution obtained from real crystals with XRD. This is mainly because real samples have to be considered as semi-infinite in one dimension, since they possess a surface where the X-rays penetrate the crystal. In the other two dimensions they are, however, still considered to be infinite. Furthermore, the penetration depth of X-ray photons into bulk materials like the substrate of a thin film system is small against the size of the crystals due to absorption effects. The contribution of photons scattered at atoms deeper in the crystal is therefore weaker compared to scattering in the surface near region. This leads to significant changes in the diffraction pattern as it is shown in figure 2.8. As mentioned above, diffraction at infinite crystals leads to a δ distribution of the diffracted intensity (cf. 2.8(a)). If a semi-infinite crystal is assumed, so called crystal truncation rods (CTR) appear since additional intensity occurs perpendicular to the surface between the diffraction peaks (cf. 2.8(b)). The (theoretical) intensity at the exact position of the peak is, however, still infinite. Taking absorption effects into account, this intensity becomes finite and a LORENTZIAN intensity distribution occurs close to the peak position (cf. 2.8(c)).

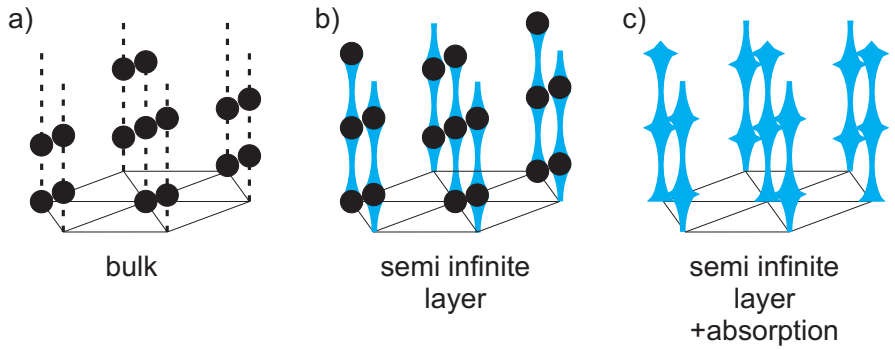

Figure 2.8: Diffraction patterns from an infinite bulk crystal (a), a semi-infinite crystal (b) and a semi-infinite crystal taking absorption effects into account (c).

Since the crystal is assumed to be infinite parallel to the surface, the total diffracted amplitude is given as

$$A(\boldsymbol{q}) = A_0\, C\, F(\boldsymbol{q}) \sum_{n_1=-\infty}^{\infty} e^{i\, n_1\, \boldsymbol{q}\cdot\boldsymbol{a}} \sum_{n_2=-\infty}^{\infty} e^{i\, n_2\, \boldsymbol{q}\cdot\boldsymbol{b}} \sum_{n_3=-\infty}^{N_3(n_1,n_2)} e^{i\, l\, \boldsymbol{q}\cdot\boldsymbol{c}}\, e^{i\, l\epsilon} \tag{2.37}$$

$$= A_0\, C\, F(\boldsymbol{q}) \sum_{n_1=-\infty}^{\infty} e^{i\, n_1\, \boldsymbol{q}\cdot\boldsymbol{a}} \sum_{n_2=-\infty}^{\infty} e^{i\, n_2\, \boldsymbol{q}\cdot\boldsymbol{b}} \sum_{n_3=-\infty}^{N_3(n_1,n_2)} e^{i\, l\, (\boldsymbol{q}\cdot\boldsymbol{c}+\epsilon)}. \tag{2.38}$$

where summation of the unit cells perpendicular to the surface is described with the third sum. Here, absorption effects are also included in the last exponential function containing the damping factor ϵ . Surface roughness is also taken into account, since the number of unit

cells perpendicular to the surface is given for each lateral position (n_1, n_2) as illustrated in figure 2.9. Because the crystal is assumed to be infinite in parallel direction, the diffracted

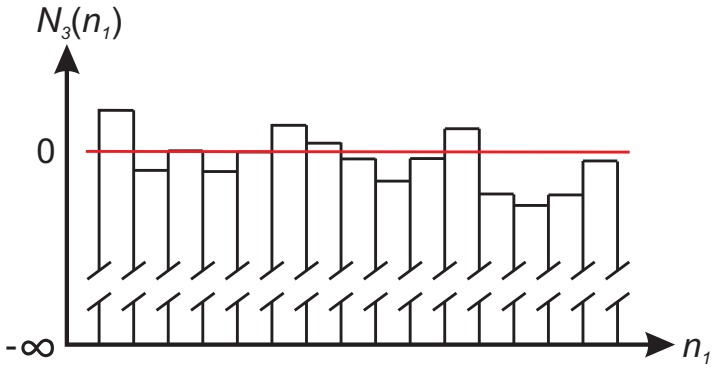

Figure 2.9: Scheme of a two dimensional semi-infinite crystal. At each lateral position (n_1) a particular number of unit cells N_3 perpendicular to the surface is considered to model the surface roughness.

intensity is located exclusively at the CTRs. Therefore, only the CTRs are considered in the following to calculate the total diffracted amplitudes. In this case on has $\boldsymbol{q}\cdot\boldsymbol{a} = 2\pi h$ and $\boldsymbol{q}\cdot\boldsymbol{b} = 2\pi k$ according to the LAUE conditions, so that the amplitude is given as

$$A(\boldsymbol{q}) = A_0\, C\, F(\boldsymbol{q}) \sum_{n_1=-\infty}^{\infty} 1 \sum_{n_2=-\infty}^{\infty} 1 \sum_{n_3=-\infty}^{N_3(n_1,n_2)} e^{\,i\, n_3\, (\boldsymbol{q}\cdot\boldsymbol{c}+\epsilon)} \tag{2.39}$$

$$= A_0\, C\, F(\boldsymbol{q}) \sum_{n_1=-\infty}^{\infty} \sum_{n_2=-\infty}^{\infty} \frac{e^{\,i\, N_3(n_1,n_2)\, (\boldsymbol{q}\cdot\boldsymbol{c}+\epsilon)}}{1 - e^{\,-(i\,\boldsymbol{q}\cdot\boldsymbol{c}+\epsilon)}} \tag{2.40}$$

$$= A_0\, C\, F(\boldsymbol{q}) \frac{\left\langle e^{\,i\, N_3(n_1,n_2)\, (\boldsymbol{q}\cdot\boldsymbol{c}+\epsilon)} \right\rangle_{n_1,n_2}}{1 - e^{\,-(i\,\boldsymbol{q}\cdot\boldsymbol{c}+\epsilon)}} \,. \tag{2.41}$$

Here, the brackets $\langle\rangle_{n_1,n_2}$ denote averaging with respect to n_1 and n_2. We assume that the position of the topmost unit cell perpendicular to the surface is GAUSSIAN distributed with an average position $\bar{N}_3$ and a standard deviation σ, which corresponds to the rms roughness of the surface. Thus, we can express the averaging part of equation 2.41 with

$$\left\langle e^{\,i\, N_3(n_1,n_2)\, (\boldsymbol{q}\cdot\boldsymbol{c}+\epsilon)} \right\rangle_{n_1,n_2} \equiv \int_{-\infty}^{\infty} dn_3 \frac{1}{\sigma\sqrt{2\pi}}\, e^{\,-\frac{\left(n_3-\overline{N_3}\right)^2}{2\sigma^2}}\; e^{\,n_3\,(i\,\boldsymbol{q}\cdot\boldsymbol{c}+\epsilon)} \tag{2.42}$$

$$= e^{\,-\frac{\sigma^2(\boldsymbol{q}\cdot\boldsymbol{c})^2}{2}}\; e^{\,\overline{N_3}\,(i\,\boldsymbol{q}\cdot\boldsymbol{c}+\epsilon)} \,. \tag{2.43}$$

Within the coordinate system, the arbitrary position of the topmost unit cell is defined as zero (cf. figure 2.9). This simplifies equation 2.43 and the diffracted amplitude can be written

as

$$A(\boldsymbol{q}) = A_0\, C\, F(\boldsymbol{q})\, \frac{e^{-\sigma^2 (1-\cos(\boldsymbol{q}\cdot\boldsymbol{c}))}}{1 - e^{-(i\,\boldsymbol{q}\cdot\boldsymbol{c}+\epsilon)}}\ . \tag{2.44}$$

2.3.7 Diffraction at a thin film

To describe the diffraction at ultra-thin films, which are mainly investigated in the presented thesis, the concept of semi-infinite crystals has to be restricted by assuming a finite number of unit cells perpendicular to the surface. As mentioned in chapter 2.3.1, no damping effects occur within these films, since they are small against the penetration depth of the X-rays. This also includes the first layers below the thin films (e.g. the topmost layers of the substrate). However, roughness of the film has to be taken into account for both the top side and the bottom side of the film (cf. figure 2.10). Since only the diffracted intensity at the CTRs is

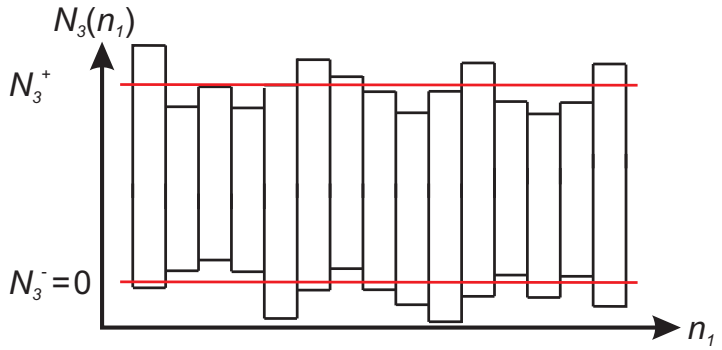

Figure 2.10: Scheme of a two dimensional thin film. At each lateral position (n_1) a particular number of unit cells perpendicular to the surface is considered to model the surface roughness. Here, roughnesses occur at both the top side and the bottom side of the film.

considered, the amplitude of a wave diffracted at a thin film is described as

$$A(\boldsymbol{q}) = A_0\, C\, F(\boldsymbol{q}) \sum_{n_1=-\infty}^{\infty} 1 \sum_{n_2=-\infty}^{\infty} 1 \sum_{n_3=N_3^-(n_1,n_2)}^{N_3^+(n_1,n_2)} e^{i\, n_3 \boldsymbol{q}\cdot\boldsymbol{c}}\ . \tag{2.45}$$

Here, $N_3^-(n_1,n_2)$ and $N_3^+(n_1,n_2)$ denote the positions of the bottommost and topmost unit cell, respectively. According to the semi-infinite crystal, these positions are assumed to be Gaussian distributed with the average position of the bottommost unit cell defined as zero. According to chapter 2.3.6, we get an amplitude of the diffracted wave of

$$A(\boldsymbol{q}) = A_0\, C\, F(\boldsymbol{q})\, \frac{e^{-\sigma_-^2 (1-\cos\boldsymbol{q}\cdot\boldsymbol{c})} - e^{i\,\overline{N_3}\,\boldsymbol{q}\cdot\boldsymbol{c}}\, e^{-\sigma_+^2 (1-\cos\boldsymbol{q}\cdot\boldsymbol{c})}}{1 - e^{i\,\boldsymbol{q}\cdot\boldsymbol{c}}}\ . \tag{2.46}$$

2.3.8 Diffraction at crystalline film systems

The samples investigated in this thesis are always composed of a crystalline substrate with one or more crystalline films on top. Furthermore, amorphous interfaces with random distribution of the scattering centers may occur between those crystalline parts. These interfaces simply act as spacers between the crystalline parts since diffraction methods are insensitive to amorphous structures (cf. chapter 2.3). Assuming pseudomorphical film growth, the lateral size of substrate and film unit cells are identical as well as the positions of substrate and film CTRs. To describe the amplitude of waves diffracted at these crystalline film systems, the diffracted amplitudes of the substrate (equation 2.44) and the individual thin films (equation 2.46) are added up coherently to

$$A(\boldsymbol{q}) = A_0\, C \left(F_0(\boldsymbol{q})\, \frac{e^{-\sigma^2 (1-\cos(\boldsymbol{q}\cdot\boldsymbol{c}))}}{1 - e^{-(i\,\boldsymbol{q}\cdot\boldsymbol{c}+\epsilon)}} + \sum_{m=1}^{M} \theta_m\, e^{i\,\boldsymbol{q}\cdot\boldsymbol{p_m}}\, F_m(\boldsymbol{q}) \right.$$
$$\left. \cdot\, \frac{e^{-\sigma^2_{-,m}(1-\cos\boldsymbol{q}\cdot\boldsymbol{j_m})} - e^{i\,\overline{N_{3m}}\,\boldsymbol{q}\cdot\boldsymbol{j_m}} \cdot e^{-\sigma^2_{+,m}(1-\cos\boldsymbol{q}\cdot\boldsymbol{j_m})}}{1 - e^{i\,\boldsymbol{q}\cdot\boldsymbol{j_m}}} \right), \tag{2.47}$$

with M different crystalline films m and the vertical unit cell vector $\boldsymbol{j_m}$ giving the distance between the layers of the film.

Here, the term

$$\sum_{m=1}^{M} \theta_m\, e^{i\,\boldsymbol{q}\cdot\boldsymbol{p_m}}\, F_m(\boldsymbol{q}) \tag{2.48}$$

contains the fill factor θ_m, which is mainly used to describe cavities inside the films caused by incompletely closed layers during film growth. It can further be used to describe the decreased contribution of the diffracted film intensity to the total diffracted signal of the crystalline system if substrate and film CTRs exhibit slightly different lateral positions. This is caused for example by non-pseudomorphical film growth and the fact that the intensity is always calculated at the positions of the film CTRs.

Furthermore, the phase vector

$$\boldsymbol{p_m} = \boldsymbol{g_m} + \sum_{m'=1}^{m-1} \boldsymbol{g_{m'}} + \overline{N_{3m'}}\boldsymbol{j_{m'}} \tag{2.49}$$

in equation 2.48 gives the phase of the current film. It depends on the interface distance vector $\boldsymbol{g_m}$ and on the phase shifts $\boldsymbol{g_{m'}} + \overline{N_{3m'}}\boldsymbol{j_{m'}}$ originating from the crystalline parts below (the substrate and additional films).

2.4 Electron diffraction

Low energy electron diffraction (LEED) is used to investigate the structure and morphology of crystalline surfaces. For this purpose, the surfaces are irradiated with electrons in the

energetic region of 20 eV up to 500 eV since these electrons exhibit De Broglie wavelengths similar to the size of the investigated structures. Due to their small penetration depth of about 10 Å into solid state materials, these electrons are sensitive only to the surface of the crystalline structure. The main advantage of this method in contrast to imaging techniques like scanning tunneling microscopy (STM) is that statistic statements about large parts of the structure can be made. In contrast to this imaging techniques give exact information about the structure, but only for small parts of the surface.

2.4.1 Kinematic theory of electron diffraction

To describe the diffraction of electrons at surfaces, we can use the knowledge of (X-ray) diffraction presented in chapters 2.2 and 2.3. However, electrons show significantly different properties regarding the interaction with matter compared to X-ray photons. Since electrons are negatively charged particles, they interact with atoms through the Coulomb forces. Thus, they feel the influence of both the nuclei and the electron shell. Furthermore, strong electron-electron interactions result in a large cross section of electrons scattered at atoms, so that multi scattering processes cannot be excluded. The kinematic diffraction theory presented in chapter 2.3.1 is therefore only roughly valid for electron diffraction.

Because of the deviations from the kinematic diffraction theory, only statements about positions and profiles of the diffracted intensity peaks can be derived exactly from the calculation. It is, however, not possible to determine the exact total intensities of the diffracted peaks. For this purpose the dynamic electron diffraction theory has to be used. For the interpretation of the experimental data investigated in the presented thesis, it is still sufficient to use the kinematic theory since the total intensities of are not considered.

As shown in chapter 2.3.5, the amplitude of X-rays diffracted at single crystalline structures with N unit cells n can be written as

$$A\left(\boldsymbol{q}, \boldsymbol{k}_i\right) = A_0\, C \sum_n F(\boldsymbol{q}, \boldsymbol{k}_i)_n\, e^{\,i\,\boldsymbol{q}\,\cdot\,\boldsymbol{r}_n} \quad . \tag{2.50}$$

In general, the scattering vector $\boldsymbol{q}$ is called $\boldsymbol{K}$ in electron diffraction, but for reasons of consistency with the theory of X-ray diffraction it is still labeled as $\boldsymbol{q}$ in the theoretical background. However, due to the nature of electron radiation mentioned above, the constant parameter C and the structure factor $F(\boldsymbol{q}, \boldsymbol{k}_i)$ for electron diffraction are different compared to X-ray diffraction and cannot be determined exactly in the kinematic theory. In the case of electron diffraction, significant changes of the *atomic form factor* $f\left(\boldsymbol{q}, \boldsymbol{k}_i\right)$ can also be observed for equal atoms integrated into different environments in the crystal. Thus, atoms at step edges exhibit for example other atomic form factors than atoms at the step centers. The contribution of these variations to the total diffracted signal are considerable due to the strong electron-electron interactions and the small electron penetration depths. Therefore, each unit cell has its particular structure factor $F(\boldsymbol{q}, \boldsymbol{k}_i)_n$.

This problem can be solved by the introduction of column-shaped unit cells reaching deep into the crystal (cf. figure 2.11). This leads to structures with equal environments and it can be assumed that each atom exhibits an identical atomic form factor. Furthermore, multi

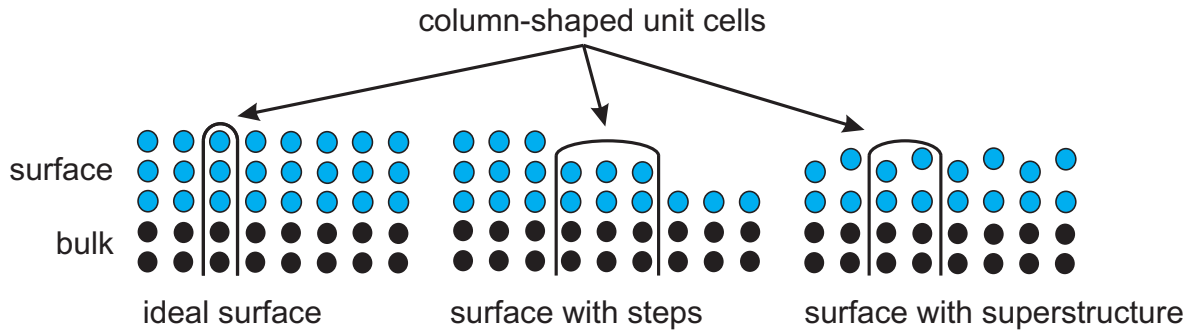

Figure 2.11: Several examples for column-shaped unit cells in the kinematic electron diffraction.

scattering processes are included in these unit cells via spatial averaging [23]. Thus, the amplitude of an electron wave diffracted at a surface can be described as

$$A\left(\boldsymbol{q},\boldsymbol{k}_i\right) \propto A_0 \underbrace{\sum_j f_j\left(\boldsymbol{q},\boldsymbol{k}_i\right) e^{\,i\,\boldsymbol{q}\cdot\boldsymbol{r}_j}}_{F(\boldsymbol{q},\boldsymbol{k}_i)} \cdot \underbrace{\sum_n e^{\,i\,\boldsymbol{q}\cdot\boldsymbol{r}_n}}_{G(\boldsymbol{q})} \ . \tag{2.51}$$

Here, the constant C is ignored since it cannot be determined exactly without taking the dynamic diffraction theory into account. The amplitude can be separated into lattice factor $G(\boldsymbol{q})$ and the dynamical form factor $F(\boldsymbol{q},\boldsymbol{k}_i)$. The lattice factor describes the shape and lateral position of the diffracted intensity peaks and can be used to determine the crystalline structure and morphology. The dynamical form factor determines the absolute intensities of the diffraction peaks and contains dynamical processes like multi scattering. As mentioned above, it is only roughly described by the kinematic diffraction theory.

For the next steps, the diffracted intensities are calculated by squaring the amplitudes and we get

$$I\left(\boldsymbol{q},\boldsymbol{k}_i\right) = \left|A\left(\boldsymbol{q},\boldsymbol{k}_i\right)\right|^2 = A\left(\boldsymbol{q},\boldsymbol{k}_i\right) A\left(\boldsymbol{q},\boldsymbol{k}_i\right)^* \propto A_0^2 \cdot \left|F(\boldsymbol{q},\boldsymbol{k}_i)\right|^2 \cdot \left|G(\boldsymbol{q})\right|^2 \ . \tag{2.52}$$

As mentioned above, the structure factor cannot be described exactly by the kinematic theory. Therefore, only the lattice factor is considered in the following. It can be written as

$$\left|G(\boldsymbol{q})\right|^2 = G(\boldsymbol{q})G(\boldsymbol{q})^* = \sum_n \sum_m e^{\,i\,\boldsymbol{q}\cdot\boldsymbol{r}_n}\, e^{\,-i\,\boldsymbol{q}\cdot\boldsymbol{r}_m} = \sum_{n,m} e^{\,i\,\boldsymbol{q}\cdot\left(\boldsymbol{r}_n - \boldsymbol{r}_m\right)} \ . \tag{2.53}$$

Assuming that the scattering centers are located at lattice positions, the position vectors

$$\boldsymbol{r_n} = \boldsymbol{a}n_1 + \boldsymbol{b}n_2 + \boldsymbol{d}h(n_1,n_2) \ . \tag{2.54}$$

are described by the primitive lattice vectors $\boldsymbol{a}$ and $\boldsymbol{b}$ parallel to the surface and the step translational vector $\boldsymbol{d}$ as well as the integer coefficients n_1, n_2 and $h(\boldsymbol{n})$. Here, the coefficient

$h(\boldsymbol{n})$ with $\boldsymbol{n} = (n_1, n_2)$ is the height function for the surface unit cell at position (n_1, n_2). For simplicity reasons, a square lattice with d perpendicular to the surface and a layer distance d is assumed so that the lattice parameter results in

$$|G(\boldsymbol{q})|^2 = \sum_{\boldsymbol{n}} \left\langle e^{\,i\,\boldsymbol{q}_\perp \cdot (h(\boldsymbol{n}+\boldsymbol{m}) - h(\boldsymbol{m}))} \right\rangle_{\boldsymbol{m}} e^{\,i\,\boldsymbol{q}_{||} \cdot (\boldsymbol{a} n_1 + \boldsymbol{b} n_2)} \ , \tag{2.55}$$

according to [24]. The brackets $\langle\rangle_{\boldsymbol{m}}$ denote averaging with respect to $\boldsymbol{m} = (m_1, m_2)$. Assuming ideal surfaces without height differences between the surface unit cells, the term between the brackets becomes unity and the lattice factor is described by

$$|G(\boldsymbol{q})|^2_{ideal} = \sum_{\boldsymbol{n}} e^{\,i\,\boldsymbol{q}_{||} \cdot (\boldsymbol{a} n_1 + \boldsymbol{b} n_2)} \ . \tag{2.56}$$

Since the two-dimensional Laue conditions are fulfilled for the lateral position vectors $\boldsymbol{r}_{\boldsymbol{n},||}$, the lattice factor represents a summation of δ functions with

$$|G(\boldsymbol{q})|^2_{ideal} = \sum_{\boldsymbol{n}} \delta(\boldsymbol{q}_{||} - \boldsymbol{r}_{\boldsymbol{n},\,||}) \ . \tag{2.57}$$

This δ distribution corresponds to the two-dimensional diffraction pattern obtained from an ideal surface.

2.4.2 The scattering phase S

The scattering phase S is a dimensionless and system independent parameter. It indicates if the interference of electron waves diffracted at different steps of a crystalline surface is constructive or destructive. This is illustrated by figure 2.12, where two electron waves diffracted at different steps are shown. Due to the geometry of the scattering process, a path difference of

$$\Delta g = S\lambda = 2d \cdot \cos(\Theta) \tag{2.58}$$

occurs, which corresponds to the Bragg condition. Here, d is the step height and Θ denotes the incident angle of the electron waves exhibiting a De Broglie wavelength of λ. By inserting the wave number definition $|\boldsymbol{k}| := 2\pi/\lambda$ into equation 2.58, the definition of the scattering phase

$$S = |\boldsymbol{k}_\perp|\, d/2\pi \tag{2.59}$$

with $|\boldsymbol{k}_\perp| = 2\,|\boldsymbol{k}| \cdot \cos(\Theta)$ is obtained. Constructive interference occurs if the scattering phase is an integral number, according to the Bragg condition. The interference is destructive if S is a half integral number. Furthermore, the scattering phase can be associated with the electron energy E. This is done by inserting the De Broglie wavelength

$$\lambda = \frac{h}{p} = \frac{2\pi\hbar}{\sqrt{2 m_e E}} \tag{2.60}$$

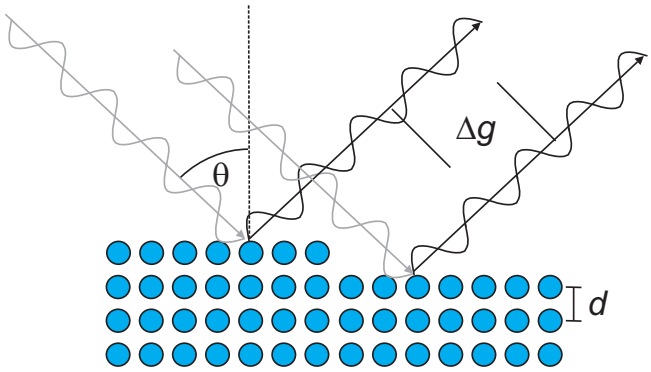

Figure 2.12: Path difference Δg of two electron waves with a De Broglie wavelength of λ diffracted at steps with different step height d. The incident angle is denoted as θ.

into equation 2.58. This results in an electron energy dependent scattering phase

$$S = \frac{d \cos\Theta \sqrt{2 m_e E}}{\pi \hbar} \ . \tag{2.61}$$

Therefore, it is possible to adjust the desired scattering phase by choosing the corresponding electron energy. It is, however, necessary to know the step height of the investigated system.

2.4.3 Mono atomic steps

In chapter 2.4.1 only ideal surfaces were considered to describe the diffraction patterns obtained from electron waves diffracted at crystalline surfaces. In the following, mono atomic steps, as they where already introduced in the previous chapter, are included in these calculations. These defects can be described as translations of the surface unit cells by multiples of the layer distances $\boldsymbol{d} \cdot h(\boldsymbol{n})$ in vertical direction. However, these unit cells are still located at lattice points after translation. Thus, the lattice factor in equation 2.55 cannot be simplified and has to be described as

$$|G(\boldsymbol{q})|^2 = \sum_{\boldsymbol{n}} \left\langle e^{\,i\,\boldsymbol{q}_\perp \cdot (h(\boldsymbol{n}+\boldsymbol{m}) - h(\boldsymbol{m}))} \right\rangle_{\boldsymbol{m}} e^{\,i\,\boldsymbol{q}_{||} \cdot (\boldsymbol{a} n_1 + \boldsymbol{b} n_2)} \tag{2.62}$$

$$= \sum_{\boldsymbol{n}} \Phi(\boldsymbol{n}, \boldsymbol{q}_\perp)\, e^{\,i\,\boldsymbol{q}_{||} \cdot (\boldsymbol{a} n_1 + \boldsymbol{b} n_2)} \ . \tag{2.63}$$

$\Phi(\boldsymbol{n}, \boldsymbol{q}_\perp)$ denotes the phase correlation and can be regarded as the Fourier transformed height distribution of the surface unit cells. By substituting the vertical scattering vector $\boldsymbol{q}_\perp$ with the scattering phase S it can be written as

$$\Phi(\boldsymbol{n}, S) = \sum_{h=-\infty}^{\infty} C(\boldsymbol{r}_{(\boldsymbol{n},||)}, h) \cdot e^{i 2\pi S h} \tag{2.64}$$

which is associated with the pair correlation $C(\vec{r}_{(\boldsymbol{n},||)}, h)$. The pair correlation gives the probability to find two scattering centers with a lateral distance of $\boldsymbol{r}_{\boldsymbol{n},||}$ and a vertical distance

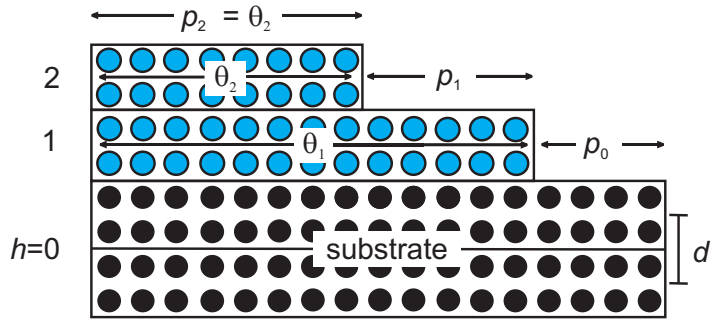

Figure 2.13: Model of a surface with mono atomic steps. The substrate is partially covered by two layers Θ_1 and Θ_2. The visible parts of the layers are denoted by p_h. In general, the topmost layer is completely visible which results in $\Theta_H = p_H$.

of $\boldsymbol{d} \cdot h(\boldsymbol{n})$. Since the lattice factor is the FOURIER transformation of the pair correlation, the profiles of the diffracted intensity peaks are determined by the appearance of the correlation function $C(\vec{r}_{(\boldsymbol{n},||)}, h)$.

The other way around, information about distribution and sizes of the mono atomic steps can be made by profile analysis of the diffraction spots. Thus, models can be established to characterize the surface morphology. A simple model, which can be used to describe these mono atomic steps, is shown in figure 2.13. Here, a substrate is covered by two mono atomic layers with coverages of Θ_1 and Θ_2. The visible parts of the layers are denoted by p_h, which also gives the probability of an electron wave to find a scattering center at the h th layer.

Taking this into account, the behavior of $C(\vec{r}_{(\boldsymbol{n},||)}, h)$ at the boundaries can be described as

$$C(\boldsymbol{r}_{(\boldsymbol{n},||)}, h) \rightarrow \begin{cases} \sum_h p_{(l+h)} p_h \cdot [1 - \varphi_h(\boldsymbol{r}_{(\boldsymbol{n},||)})] & \text{for h}\neq 0 \\ \\ 1 - \sum_{h\neq 0} C(\boldsymbol{r}_{(\boldsymbol{n},||)}, h) & \text{for h=0,} \end{cases} \tag{2.65}$$

according to [25]. Here, $\varphi_h(\boldsymbol{r}_{(\boldsymbol{n},||)})$ equals one at the origin ($r = 0$) and zero when the distance between two scattering centers become infinity ($r \rightarrow \infty$). In this case, the probability to find two scattering centers with the height difference h depends on the visible coverages p_h. Between these border cases $\varphi_h(\boldsymbol{r}_{(\boldsymbol{n},||)})$ is determined by the terrace width distribution. Back-transformation of the pair correlation results in the lattice factor

$$\left|G(S, \boldsymbol{q}_{||})\right|^2 = \underbrace{G_0(S)\delta(\boldsymbol{q}_{||})}_{peak} + \underbrace{[1 - G_0(S)]\Phi_{shoulder}(S, \boldsymbol{q}_{||})}_{shoulder} \tag{2.66}$$

with

$$G_0(S) = \sum_h C_h \cos(2\pi h S) \ . \tag{2.67}$$

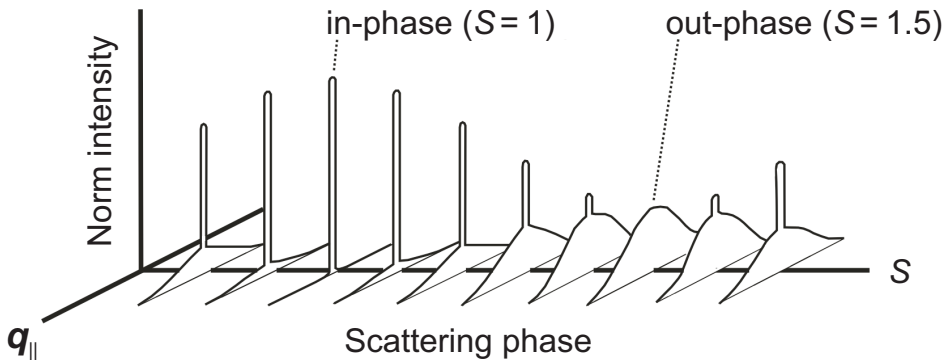

Figure 2.14: The lateral intensity distribution in dependence of the scattering phase S. Here, the electron wave is diffracted at a surface with mono atomic steps.

In this case, the intensity distribution can be described by two parts, the central *peak* and the diffuse *shoulder*. Whereas the peak intensity is δ-distributed, the intensity profile of the shoulder is the FOURIER transformation of the terrace width distribution. Both parts are dependent on the scattering phase as it is shown in figure 2.14. At in-phases or out-phases only the central peak or the shoulder can be observed, respectively. Between these cases the intensity distribution is determined by the superposition of both parts.

As mentioned above, the lateral morphology of the surface can be determined by analyzing the diffuse shoulder profile. This was mainly performed in the presented thesis, except the analysis of diffracted intensity positions in the two-dimensional diffracted pattern. Therefore, the method used to analyze the diffuse shoulder is presented in the following, whereas the analysis of the central peak is not considered.

2.4.4 H(S)-analysis

This method describes the scattering phase dependent analysis of the FWHM of the diffuse shoulder intensity. To apply the H(S)-analysis to the data, obtained from the investigated samples it is necessary to make several assumptions. On the one hand, a geometric terrace width distribution described by

$$P(\Gamma) = Ne^{-\frac{\Gamma}{N}} \tag{2.68}$$

with $N = \langle\Gamma\rangle^{-1}$ as normalization constant is assumed. This means that the probability of terraces decreases exponentially with increasing terrace width. On the other hand, very rough surfaces are considered, which leads to a distribution $P_{steps}(h)$ of the terrace heights in addition to the geometric terrace width distribution.

According to [26], the diffracted intensity profile of the diffuse shoulder results in

$$\Phi_{shoulder}(\boldsymbol{q}_{||}) = \frac{1}{2[1-cos(qa)]}\left[\frac{(1-\beta_S)(1-\beta_T)}{(1-\beta_S\beta_T)} + ...\right] , \tag{2.69}$$

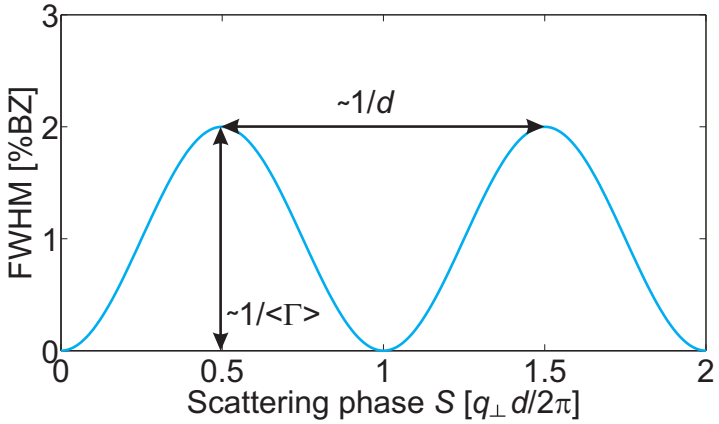

Figure 2.15: FWHM of the diffuse shoulder depending on the scattering phase for very rough surfaces. The vertical layer distance d can be determined by the distance between the maxima of the FWHM and the mean terrace width $\langle\Gamma\rangle$ can be calculated from the difference of maxima and minima.

with the lateral lattice constant a and FOURIER transformed distributions of terrace heights

$$\beta_S = \sum_h P_S(h) e^{i2\pi Sh} \tag{2.70}$$

as well as terrace widths

$$\beta_T = \sum_\Gamma P_T(\Gamma) e^{iaq_{||}\Gamma} \ . \tag{2.71}$$

Assuming a symmetrical distribution of the terrace heights, the intensity distribution of the diffuse shoulder can be described with a LORENTZIAN function and

$$\Phi_{shoulder}(\boldsymbol{q}_{||}) \propto \frac{1}{\kappa^2 + (a\boldsymbol{q}_{||})^2} \quad \text{with} \quad \kappa = \frac{1-\beta_S(\boldsymbol{q}_\perp)}{\langle\Gamma\rangle} \ . \tag{2.72}$$

The corresponding FWHM is determined by

$$a\Delta\boldsymbol{q}_{||} = \frac{2(1-\beta_S(S))}{\langle\Gamma\rangle} \Rightarrow a\Delta\boldsymbol{q}_{||} = \frac{2(1-\cos(2\pi S))}{\langle\Gamma\rangle} \ . \tag{2.73}$$

The experimental data always gives the distance between the diffraction spots in percent of the BRILLOUIN-zone which is the distance between the next neighbor reflex positions. Therefore, it is useful to convert the FWHM of the reflex profile into units of [%BZ]. The FWHM normalized to units of [%BZ] can be expressed as

$$\Delta\tilde{q}_{||} = \frac{a\Delta\boldsymbol{q}_{||}}{2\pi} \cdot 100\% = \frac{100\%BZ}{\pi} \cdot \frac{1-\cos(2\pi S)}{\langle\Gamma\rangle}. \tag{2.74}$$

The approximation of the terrace heights distribution with a cosine function, as mentioned above, is only true for single steps at the surface. For illustration, the scattering phase dependency of the FWHM of the diffuse shoulder is shown in figure 2.15. Here, it can be seen that the FWHM is maximal with integer scattering phase and minimal if S is a half integer value. From this dependency, the vertical layer distance d can be determined by the distance between the maxima of the FWHM and the mean terrace $\langle\Gamma\rangle$ width can be calculated from the difference of maxima and minima.

2.4.5 Influence of mosaics without preferred orientation on the spot profiles in electron and X-ray diffraction

Mosaics are formed if small areas of the crystal (crystallites) are tilted against each other (cf. figure 2.16(b)). Thus, the crystal lattices of the crystallites are tilted accordingly so that the scattering centers are not located at lattice points any longer. Since the diffraction rods are oriented perpendicular to the surface, they are also tilted corresponding to the crystal lattice. If the mosaics do not exhibit a preferred orientation, the crystallites can be tilted in every lateral direction, whereas the tilting angle exhibits a GAUSSIAN-shaped distribution with a standard deviation $\Delta\theta \neq 0$. This leads to an increase of the diffraction rod FWHM $\Delta q_{||}$ with increasing vertical scattering vector $\Delta q_{\perp}$ as it is shown in figure 2.16. These mosaics occur for example during thermal treatment of the substrate or during heteroepitaxy. Here, mosaics are formed to reduce strain caused by the lattice mismatch between film and substrate. The standard deviation of the mosaic spread for electron diffraction measurements can be derived by

$$\frac{\Delta \boldsymbol{q}_{||}}{2 \cdot |\boldsymbol{q}_{\perp}|} = \tan\left(\frac{\Delta\theta}{2}\right) \approx \frac{\Delta\theta}{2} \,, \tag{2.75}$$

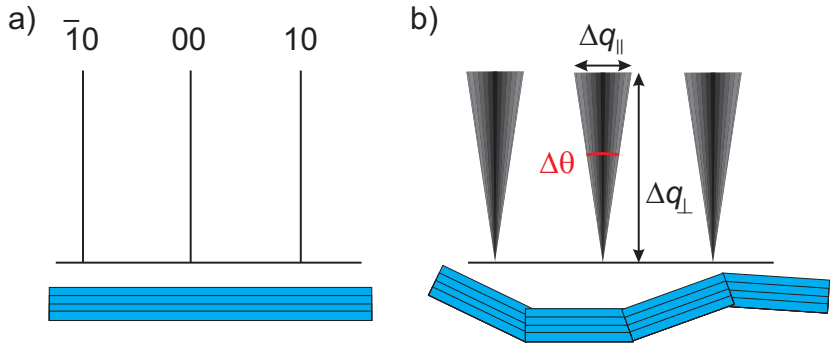

Figure 2.16: (a) Ideal surface and corresponding diffraction rods. (b) Surface with mosaics and corresponding diffraction rods exhibiting a linear increase of the FWHM. The mean mosaic spread angle is $\Delta\theta = \Delta q_{||}/\Delta q_{\perp}$.

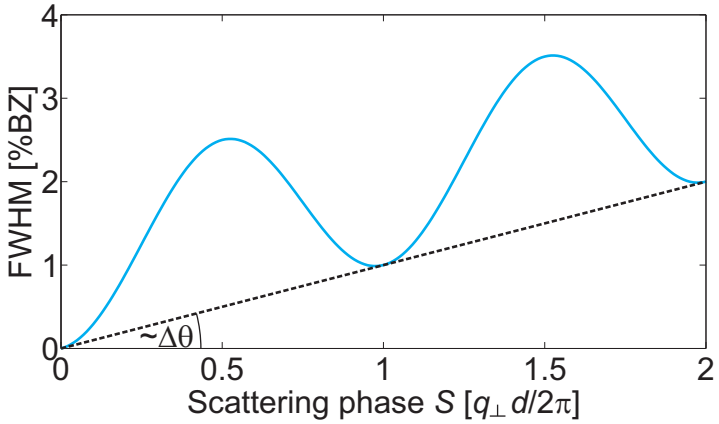

Figure 2.17: FWHM of the diffuse shoulder depending on the scattering phase for very rough surfaces and additional mosaic spread. The mean mosaic spread $\Delta\theta$ can be determined by the angle between the straight line through the minima of the FWHM and the abscissae.

using the small angle approximation. Taking the definitions of the scattering phase and the BRILLOUIN-zone into account $\Delta\theta$ can be written as

$$\frac{\Delta\theta}{2} \approx \frac{2\pi \cdot \Delta\tilde{q}_{||}}{a \cdot 100\%BZ} \cdot \frac{d}{4\pi S} = \frac{d \cdot \Delta\tilde{q}_{||}}{a \cdot 200\%BZ \cdot S} \ , \tag{2.76}$$

where d and a denote the layer distance and the next neighbor distance of the investigated material, respectively. Since distances within the measurements of both X-ray and electron diffraction are normalized to the substrate, the lattice parameters of Si ($d = 3.1356\,\text{Å}$ and $a = 3.8401\,\text{Å}$; cf. chapter 3) are used to calculate the mean mosaic spreads in the presented thesis. To determine the lateral morphology of the surface by analyzing the scattering phase dependent FWHM of the diffraction spots, the mosaic spread is taken into account by adding a linear function to equation 2.74. The FWHM of the diffraction spot is described as

$$\Delta\tilde{q}_{||,total} = 100\%BZ \left[\frac{1}{\pi}\frac{1-\cos(2\pi S)}{\langle\Gamma\rangle} + \sqrt{2}\Delta\theta \cdot S\right] \ . \tag{2.77}$$

The influence of mosaics without preferred orientation at the surface on the FWHM of the diffraction spot depending on the scattering phase is shown in figure 2.17.

For X-ray diffraction a similar influence of mosaics without preferred orientation on the lateral FWHM of the CTRs can be observed. However, the diffracted X-ray intensity is mainly concentrated at the BRAGG peaks and only small intensity can be observed between them. Therefore, it is necessary to determine the lateral FWHM of several BRAGG peaks at a CTR to precisely calculate the mean mosaic spread. As shown in figure 2.18, the FWHM of the BRAGG peak obtained at the bottom of the CTR can be used to calculate the lateral crystallite size $D_{||}$.

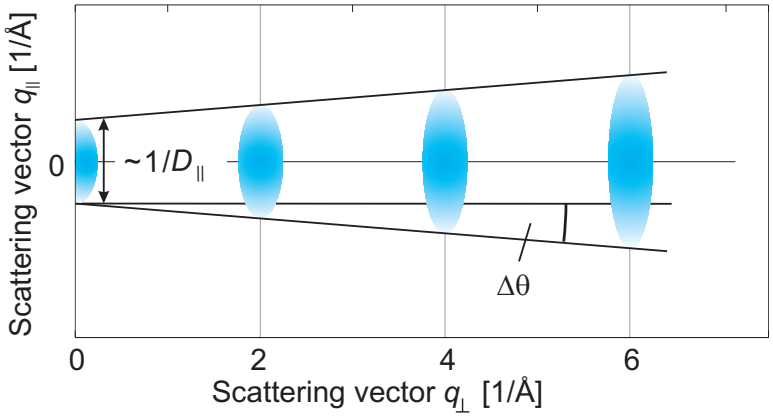

Figure 2.18: FWHM of the BRAGG peaks at the specular CTR. The FWHM increases linearly with increasing total value of the vertical scattering vector $q_\perp$ due to mosaics without preferred orientation. From this behavior, the mean mosaic spread $\Delta\theta$ and the lateral crystallite size $D_{||}$ can be derived.

2.5 X-ray reflection

X-ray reflectometry (XRR) is a powerful tool to characterize thin films, multilayer structures as well as interface roughnesses. The samples are irradiated with electromagnetic (EM) waves in the X-ray wavelength region at small incident angles of $\alpha_i < 5°$. These waves are partially reflected at the sample surface at an angle of $\alpha_f = \alpha_i$. In contrast to conventional optics where angles are measured between the direction of propagation and the surface normal, the angles in X-ray reflectometry are measured between the direction of propagation and the surface.

2.5.1 Basic principles

The reflectivity at interfaces between two materials depends on the incident angle and the indices of refraction n_i of the involved materials (cf. figure 2.19). By measurement of the reflected intensity during variation of the incident angle, information about interface roughness, layer thickness and refractive index of the individual materials can be determined.

EM plane waves with an electric field vector $\boldsymbol{E}(\boldsymbol{r}) = \boldsymbol{E_0} \exp(i\,\boldsymbol{k_i} \cdot \boldsymbol{r})$ propagating in a medium, which is characterized by the refractive index $n(\boldsymbol{r})$, are described according to the HELMHOLTZ equation

$$\Delta \boldsymbol{E}(\boldsymbol{r}) + k^2 n^2(\boldsymbol{r}) \boldsymbol{E}(\boldsymbol{r}) = 0 \ , \tag{2.78}$$

where $k = 2\pi/\lambda$ is the absolute value of the wave vector $\boldsymbol{k}_i$ and λ denotes the wavelength of the EM wave. To describe the refractive index, it is assumed that atoms are harmonic oscillators with resonance frequencies ω_j. For an arrangement of N atoms per unit volume

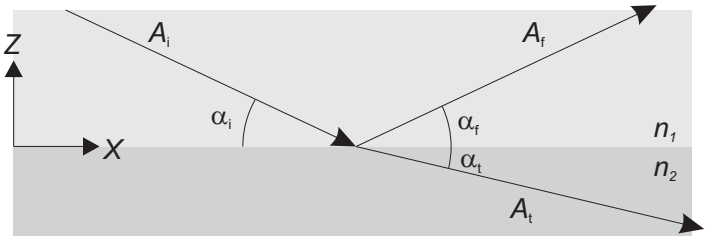

Figure 2.19: X-ray reflection and refraction at an interface between two materials with the refraction indices n_1 and n_2. One part A_f of the incoming X-ray beam A_i is reflected at the interface at an angle of reflection α_f identical to the incident angle α_i. The remaining part A_t is refracted and transmitted at an angle α_t.

the refractive index can be expressed as

$$n^2(\boldsymbol{r}) = 1 + N\frac{e^2}{\epsilon_0}m_e \sum_{j=1}^{N} \frac{f_j}{\omega_j^2 - \omega^2 - 2i\omega\eta_j} \ , \tag{2.79}$$

with the electron charge e and mass m_e, the electric constant ϵ_0, the frequency of the incoming EM wave ω and damping factors η_j. The forced oscillation strength of the electrons of each atom is denoted as f_j. Values of f_j are complex numbers, $f_j = f_j^0 + f_j'(E) + if_j''(E)$, where $f_j'(E)$ and $f_j''(E)$ contain dispersion and absorption corrections, respectively. These corrections depend on the radiation energy E. If $\omega > \omega_j$, which is true for X-ray photons, the refractive index can be written as

$$n(\boldsymbol{r}) = 1 - \delta(\boldsymbol{r}) + i\beta(\boldsymbol{r}) \ , \tag{2.80}$$

with the terms of dispersion

$$\delta(\boldsymbol{r}) = \frac{\lambda^2}{2\pi}\, r_e\rho(\boldsymbol{r}) \sum_{j=1}^{N} \frac{f_j^0 + f_j'(E)}{Z} \tag{2.81}$$

and absorption

$$\beta(\boldsymbol{r}) = \frac{\lambda^2}{2\pi}\, r_e\rho(\boldsymbol{r}) \sum_{j=1}^{N} \frac{f_j''(E)}{Z} = \frac{\lambda}{4\pi}\mu(\boldsymbol{r}) \ . \tag{2.82}$$

Here, the classical electron radius $r_e = e^2/(4\pi\epsilon_0 m_e c^2) = 2.814 \cdot 10^{-5}$Å is introduced in equation 2.81 and equation 2.82 as well as the electron density $\rho(\boldsymbol{r})$ depending on the spatial coordinates $\boldsymbol{r} = (x, y, z) = (r_{||}, z)$ and the linear absorption coefficient $\mu(\boldsymbol{r})$. The total number of electrons is denoted as $Z = \sum_j Z_j$ whereas each material component contributes with a particular number of electrons Z_j, respectively.

The linear component of the forced oscillation strength f_j^0 depends on the scattering vector $\boldsymbol{q} = \boldsymbol{k}_f - \boldsymbol{k}_i$. Since incident and reflected angles are very small during XRR measurements,

the absolute value of $\boldsymbol{q}$ is also small and does not change significantly. Therefore, f_j^0 can be approximated with high accuracy by $f_j^0 \approx Z_j$. The refractive index can now be simplified to

$$n = 1 - \frac{\lambda^2}{2\pi} r_e \rho + i \frac{\lambda}{4\pi} \mu \tag{2.83}$$

$$= 1 - \delta + i\beta \ , \tag{2.84}$$

assuming a homogeneous medium and X-ray photon energies far away from absorption edges. It should be emphasized that δ is always positive and that it is zero in vacuum and usually in the range of 10^{-6} and 10^{-4} in solid materials [22]. Therefore, the real part of the refractive index is slightly smaller than unity. Furthermore, the absorption coefficient β is usually one or two orders of magnitude smaller than the dispersion coefficient δ.

If an X-ray wave hits a vacuum/medium interface under a sufficiently small angel, it is totally reflected because the refractive index of the medium is smaller than the one of the vacuum. Due to the low density of air, this can also be approximated for real experiments since δ_{air} is very small and, thus, the refractive index of air is close to unity as well. In this case, the law of refraction gives $\cos\alpha_i = (1-\delta)\cos\alpha_t$. Total diffraction occurs at transmission angles α_t (cf. figure 2.19) smaller than zero. Therefore, the TAYLOR series expansion for small angles results in $\cos\alpha \approx 1 - \alpha^2/2$, which gives the critical angle

$$\alpha_c \approx \sqrt{2\delta} \ . \tag{2.85}$$

For a vacuum (air)/medium interface, α_c is typically below 1°.

2.5.2 Reflection at a single surface

To calculate the X-ray reflection at multilayer systems, it is useful to start with the reflectivity of an air/medium interface (cf. figure2.19), which will be presented in the following.

The electric field of an EM plane wave propagating in air is described by

$$\boldsymbol{E}_i(\boldsymbol{r}) = (0,\ A_i,\ 0)\ \exp(i\ \boldsymbol{k}_i \cdot \boldsymbol{r}) \ , \tag{2.86}$$

with the incident wave vector $\boldsymbol{k}_i = k\,(\cos\alpha_i,\ 0,\ -\sin\alpha_i)$. If the EM wave hits the air/medium interface, it is partly reflected and transmitted and the corresponding electric fields can be written as

$$\boldsymbol{E}_r(\boldsymbol{r}) = (0,\ A_r,\ 0)\ \exp(i\ \boldsymbol{k}_f \cdot \boldsymbol{r}) \tag{2.87}$$

and

$$\boldsymbol{E}_t(\boldsymbol{r}) = (0,\ A_t,\ 0)\ \exp(i\ \boldsymbol{k}_t \cdot \boldsymbol{r}) \ , \tag{2.88}$$

respectively. Here, $\boldsymbol{k}_f = k\,(\cos\alpha_i,\ 0,\ \sin\alpha_i)$ and $\boldsymbol{k}_t = (k_{t,x},\ 0,\ k_{t,z})$ denote the wave vectors of reflected and transmitted beams, whereas components of $\boldsymbol{k}_t$ are determined by the law of refraction. Considering an s-polarized EM wave, the electric field vector is perpendicular to

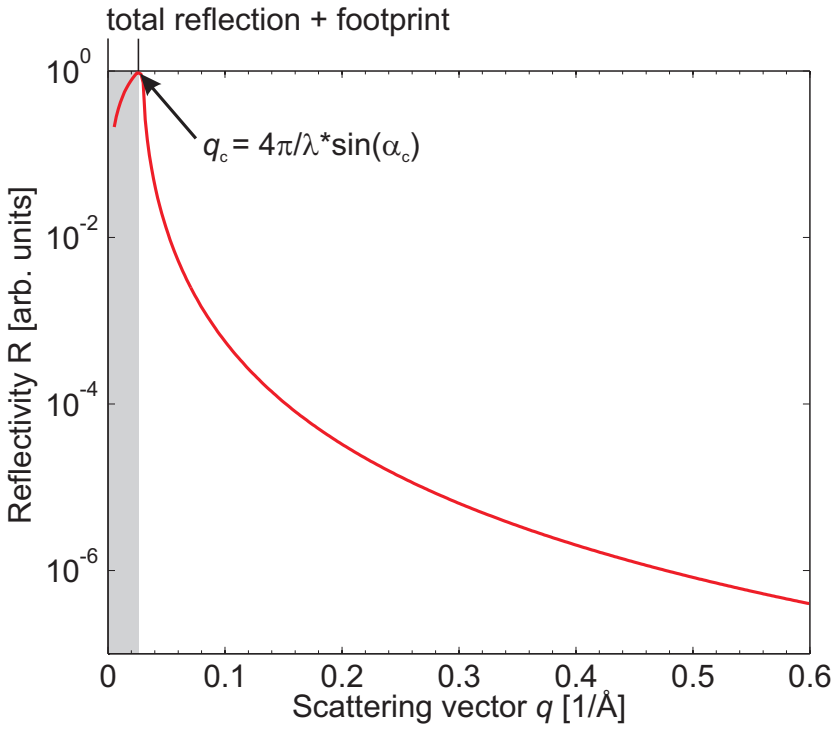

Figure 2.20: Calculated reflectivity of an EM wave reflected at an air/Si interface (10 keV photon energy). The reciprocal space region of total reflection up to the critical value q_c of the scattering vector is indicated in light gray. The linear increase of the intensity with small scattering vectors due to the three-demensional extension of the beam and the finite size of the sample is also included. This effect is called *footprint*.

the scattering plane (x,z; cf figure 2.19). In this case, the reflectivity coefficient $r_s = A_r/A_i$ and the transmission coefficient $t_s = A_t/A_i$ are described by the FRESNEL formulas [27] since the tangential components of the electric and magnetic field must be continuous at the surface (z=0). The FRESNEL formulas are given as

$$r_s = \frac{k_{i,z} - k_{t,z}}{k_{i,z} + k_{t,z}} \tag{2.89}$$

and

$$t_s = \frac{2k_{i,z}}{k_{i,z} + k_{t,z}} \ , \tag{2.90}$$

with $k_{t,z} = nk \sin \alpha_t = k\sqrt{n^2 - \cos^2 \alpha_i}$. The FRESNEL formulas of p-polarized EM waves, where the electric field vector is parallel to the scattering plane, are written as

$$r_p = \frac{k_{i,z} - k_{t,z}}{k_{i,z} + k_{t,z}} \tag{2.91}$$

and

$$t_p = \frac{2k_{i,z}}{k_{i,z} + k_{t,z}} \ . \tag{2.92}$$

In the case of X-ray reflectometry, however, the refractive index n can be approximated by unity and therefore s-polarized and p-polarized EM waves can be regarded in good approximation as identical. In the following only s-polarized X-ray photons will be considered, where the total reflectivity R of the reflected wave is $|r_s|^2$. Figure 2.20 shows a theoretically calculated intensity distribution of the reflection at a single air/Si interface depending on the scattering angle which is converted to the scattering vector

$$q = \frac{4\pi}{\lambda} \cdot \sin(\alpha). \tag{2.93}$$

2.5.3 Reflection at multilayer systems

Figure 2.21 shows a multilayer system with sharp boundary interfaces consisting of N layers with thickness d_n and a substrate (labeled as layer $N+1$) with infinite thickness. To calculate the total reflection at this multilayer system, an exact recursive approach was established by Parratt in 1954 [28] . Regarding the reflection at the interface z_{j-1}, the continuity of the tangential components of the electric field vector can be expressed as

$$a_{j-1}T_{j-1} + a_{j-1}^{-1}R_{j-1} = \quad a_j^{-1}T_j + a_jR_j \tag{2.94}$$

$$\left(a_{j-1}T_{j-1} - a_{j-1}^{-1}R_{j-1}\right) f_{j-1}k = \quad \left(a_j^{-1}T_j - a_jR_j\right) f_jk \tag{2.95}$$

with the respective amplitudes of reflected part R_j and R_{j-1} and transmitted part T_j and T_{j-1}. The phase factor

$$a_j = \exp\left(-ik_1f_j\frac{d_j}{2}\right) \tag{2.96}$$

is introduced since the amplitudes are defined for half the perpendicular layer depth d_n. Taking the boundary condition for the tangential components of the electric vectors into account, the parameter f_jk_1 gives the absolute value of the z-component of the wave vector $\boldsymbol{k}_j$ via

$$f_jk_1 = k_{z,j} = k_1\sqrt{\left(n_j^2 - \cos^2\alpha_i\right)} \ , \tag{2.97}$$

with the absolute value of the incident wave vector k_1. A recursive formula can be obtained from the simultaneous Eqs. 2.94 and 2.95 by dividing their difference by their sum [28], which results in

$$R_{j-1,j} = a_{j-1}^4\frac{R_{j,j+1} + F_{j-1,j}}{1 + R_{j,j+1}F_{j-1,j}} \tag{2.98}$$

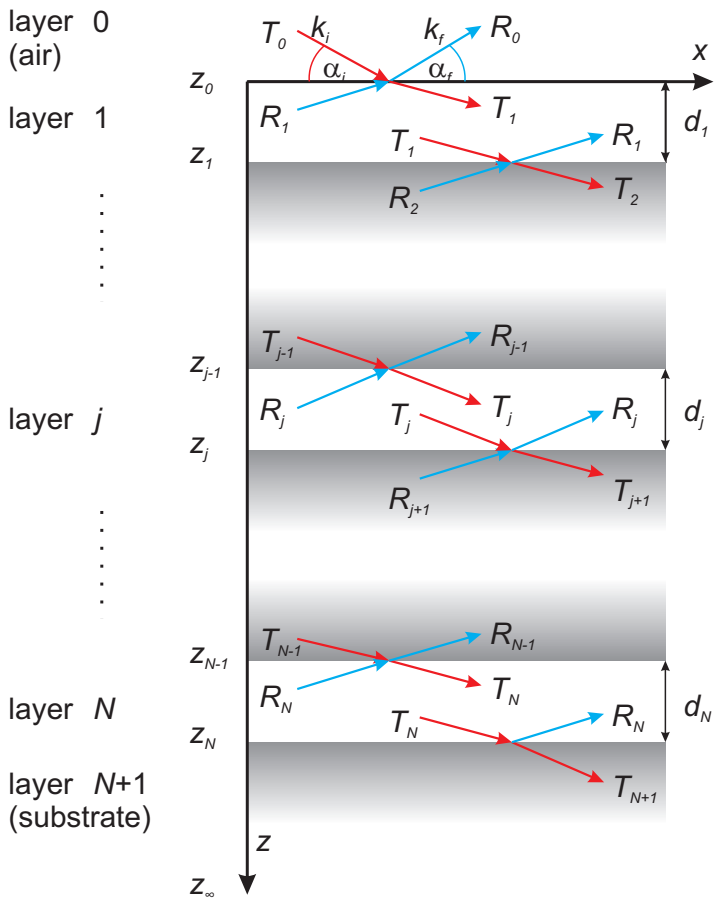

Figure 2.21: X-ray reflection at a multilayer system consisting of N layers on a substrate (labeled as layer $N+1$), image adapted from [29]. Beams (T_j) transmitted at the interfaces z_{j-1} are indicated in red, reflected beams ($R_j - 1$) in blue.

with

$$R_{j,j+1} = a_j^2 \, (R_j / T_j) \tag{2.99}$$

and

$$F_{j-1,j} = \frac{f_{j-1} - f_j}{f_{j-1} + f_j} = \frac{k_{z,j-1} - k_{z,j}}{k_{z,j-1} + k_{z,j}}, \tag{2.100}$$

with the scattering vector $(k_i - k_f) = 2\, k_{z,j}$. A detailed derivation of the recursive formula can also be seen in [30].

The starting point of the recursive calculation of the reflected intensity is the interface at the bottom of the substrate $R_{N+1,\infty}$. Since an infinite layer thickness d_{N+1} of the substrate is assumed, no reflected intensity comes from the bottom of the substrate and $R_{N+1,\infty} = 0$ (all intensity is absorbed in the substrate). Therefore, the reflectivity at the interface of layer N and the substrate layer $N+1$ results in

$$R_{N,N+1} = \frac{k_{z,N} - k_{z,N+1}}{k_{z,N} + k_{z,N+1}} \, . \tag{2.101}$$

The reflected amplitudes at the following interfaces are recursively calculated by

$$R_{j-1,j} = \frac{R_{j-1,j} + R_{j,j+1} \cdot a_j}{1 + R_{j-1,j} R_{j,j+1} \cdot a_j} \tag{2.102}$$

until the interface between layer 0 (air) and layer 1 is reached and the angle dependent reflectance coefficient is derived by

$$R = \frac{I_r}{I_0} = \left| \frac{R_0}{T_0} \right|^2 = |R_{0,1}|^2 \ . \tag{2.103}$$

Here, the phase factor of layer 0 is defined as $a_0 = 1$ and the incoming wave amplitude is normalized to $T_0 = 1$ [29].

Figure 2.22(a) shows the simulated intensity of a sample with a Si substrate and a 10 nm praseodymia layer on top. Intensity oscillations occur due to alternately appearing constructive and destructive interference, which is caused by the path difference of the reflected beams at the air/praseodymia and the praseodymia/silicon interface. The BRAGG condition using the example of X-ray reflectivity is shown schematically in figure 2.22(b) for clarification. Here, the path difference between the waves (black arrows) reflected at the bottom and top interface is $\delta = 2D \sin\alpha$ with the distance between the layers d and the incident angle Θ. If this incident angle dependent path difference is a multiple of the wavelength, constructive interference occurs. The layer thickness of the praseodymia film may be estimated from the intensity oscillation period via $D = 2\pi/\Delta q_z$.

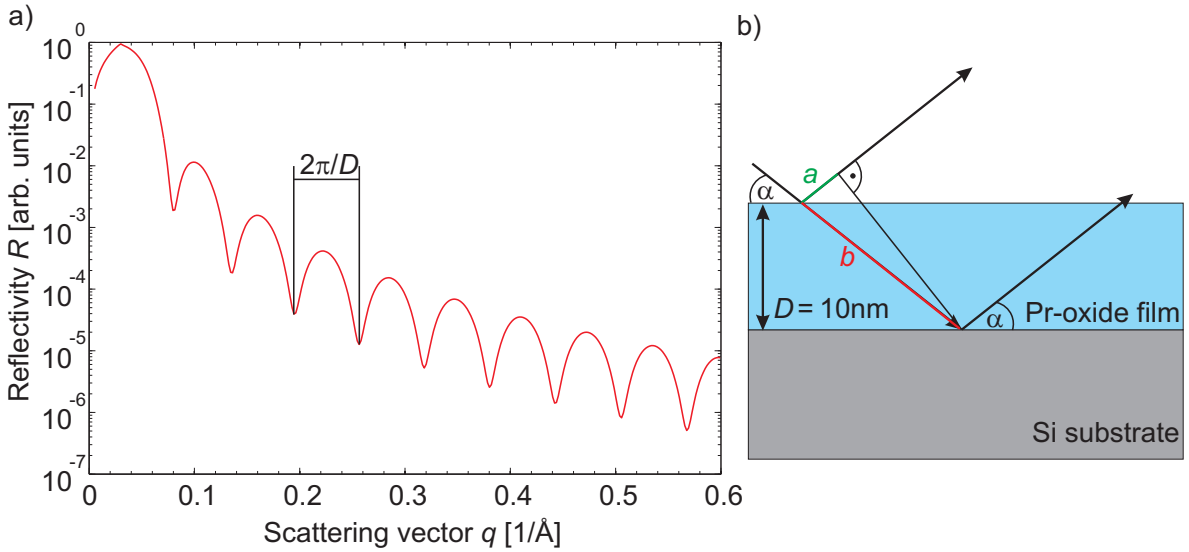

Figure 2.22: (a) Simulated reflectivity of an EM wave at a substrate with 10 nm praseodymia on top and a perfectly sharp interface between film and substrate (photon energy 10 keV). (b) BRAGG condition using the example of X-ray reflectivity with layer thickness D, incident angle α and the path difference $\Delta g = b - a$.

2.5.4 Surface roughness in XRR

Up to now, only reflection at perfectly sharp interfaces was considered. In nature, surfaces as well as interfaces are rough, which may be expressed as (quadratic) deviation from a mean height value z_j (rms-roughness). In this case, the rough interface can be replaced by an ensemble of sharp interfaces with certain z coordinates $z_j + z$, weighted by a probability density $P_j(z)$ (cf. figure 2.23(a)).

For this reason, an abrupt transition from refractive index n_{j+1} to n_j at a certain value z_j, which is assumed for smooth interfaces, cannot be obtained here. To estimate the influence of rough surfaces on the reflectivity, the refraction index is expressed as a continuous variation $n_j(x, y, z)$. Since only the specular reflectivity is of interest, the wave vector transfer $\boldsymbol{q} = \boldsymbol{k}_f - \boldsymbol{k}_i$ has no lateral (x,y) component. Therefore, the structure is laterally averaged and one-dimensional, continuous refractive index profiles

$$n_j(z) = \int\int n_j(x, y, z)\,\mathrm{d}y\,\mathrm{d}x \tag{2.104}$$

are considered.

Assuming a GAUSSIAN probability density of the interface heights

$$P_j(z) = \frac{1}{\sqrt{2\pi}\sigma_j}\, e^{-\frac{z^2}{2\sigma_j^2}}\ , \tag{2.105}$$

with the standard deviation σ_j, a continuous refractive-index profile between layers j and $j+1$ of

$$n_j(z) = \frac{n_j + n_{j+1}}{2} - \frac{n_j - n_{j+1}}{2}\ \mathrm{erf}\left(\frac{z - z_j}{\sqrt{2}\sigma_j}\right) \tag{2.106}$$

with the error function

$$\mathrm{erf}(z) = \frac{2}{\sqrt{\pi}} \int_0^z e^{-t^2}\, dt \tag{2.107}$$

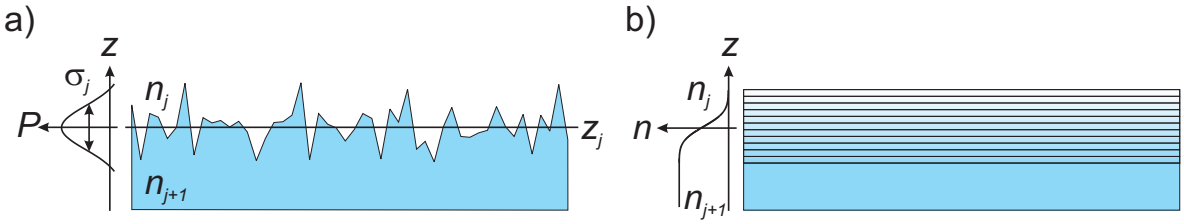

Figure 2.23: (a) Rough interface with mean interface height z_j and variations of the height $z(x, y)$ around this value. The probability P of a certain layer height is assumed to be GAUSSIAN distributed with the standard deviation σ_j. (b) Corresponding continuous (laterally averaged) refractive index distribution from n_j to n_{j+1}.

results (cf. figure 2.23(b)). This finally yields the modified FRESNEL coefficient

$$\tilde{R}_{j,j+1} = R_{j,j+1} \cdot e^{-2k_{z,j}k_{z,j+1}\sigma_j^2}, \tag{2.108}$$

describing the reflectivity of a single interface, where the exponential function is also known as NEVOT-CROCET-factor [31].

2.6 X-ray standing waves

The X-ray standing wave (XSW) technique is used to study the element specific structure of surface adsorbates with mono layer or thin film thicknesses. For this purpose, a standing X-ray wave field is generated in the surface near region of the sample and moved in a controlled way. Thus, the spatial distribution of the specific elements within the adsorbed material can be derived for example by measurement of the characteristic photoelectron emission, which is induced in the range of the interference field. In the following, the theoretical background of the XSW method is introduced. For further information, a detailed description can be found in [32].

2.6.1 Generation of X-ray standing waves

A standing wave field can be formed by interference of two coherent X-ray waves with identical wavelength λ. The usual method to obtain these waves is to perform X-ray diffraction close to the BRAGG peak conditions (cf. chapter 2.3.5) where incident and diffracted X-ray waves interact with each other at the location of the sample (cf. figure 2.24). Thus, a standing field is generated, which exhibits a wavelength of the distance $d_{\boldsymbol{q}}$ of the chosen BRAGG diffraction planes.

In general, the time dependent electric fields of incident and diffracted EM-wave at the location $\boldsymbol{r}$ are described by

$$E_i = E_i^0 e^{i(\omega t - \boldsymbol{k}_i \cdot \boldsymbol{r})} \tag{2.109}$$

and

$$E_f = E_f^0 e^{i(\omega t - \boldsymbol{k}_f \cdot \boldsymbol{r} + \nu)} \tag{2.110}$$

where E_i^0 and E_f^0 denote the amplitudes of the respective waves. The frequency is given by ω and the wave vectors of incident and diffracted waves are labeled as $\boldsymbol{k}_i$ and $\boldsymbol{k}_f$. A constant phase-relation ν occurs between both waves due to their coherence.

The electric field force E_{SW} of the emerging standing wave field is determined by the sum of incident and diffracted electric field forces. Taking the reflectivity R of the sample into account, the electric field amplitude of the diffracted wave can be expressed as $E_f^0 = \sqrt{R} \cdot E_i^0$ and the electric field of the standing wave results to

$$E_{SW} = E_i + E_f = E_i^0 e^{i(\omega t)} \left(e^{-i\boldsymbol{k}_i \cdot \boldsymbol{r}} + \sqrt{R} e^{-i\boldsymbol{k}_f \cdot \boldsymbol{r} + i\nu} \right). \tag{2.111}$$

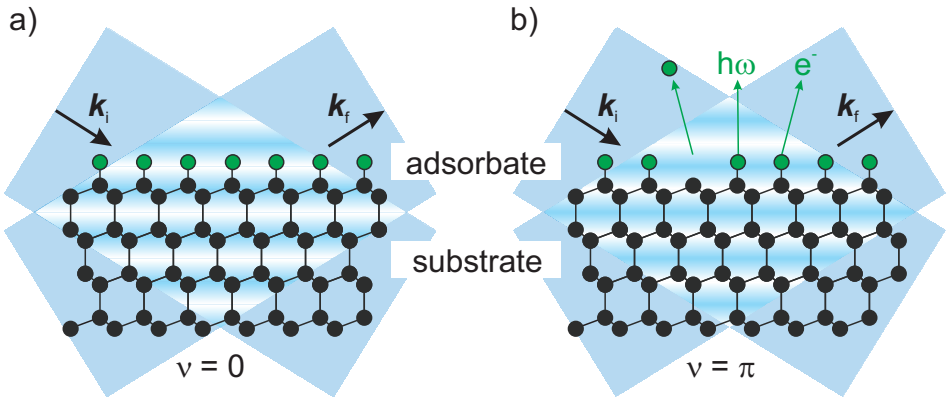

Figure 2.24: Principle of XSW generation using the diffraction of X-rays close to BRAGG peak conditions where incident wave and diffracted wave ($\boldsymbol{k}_i$ and $\boldsymbol{k}_i$) form a standing wave field at the location of the sample. (a) If the phase-shift ν between incident and diffracted wave is zero, the intensity maxima (blue stripes) are located at the diffraction planes. (b) If the phase relation shifts to $\nu = \pi$, the intensity maxima are shifted accordingly. In this example they are located afterwards at the position of the adsorbates where the emission of secondary signals like photons ($h\omega$), electrons (e^-) or adsorbed atoms is induced.

The intensity of the standing wave field formed at the BRAGG peak conditions can be written as

$$I_{SW} = E_{SW} E_{SW}^* = I_0 \cdot \left[1 + R + 2\sqrt{R}\cos\left(\nu - 2\pi \boldsymbol{qr}\right)\right]. \tag{2.112}$$

Here, extinction and absorption effects are neglected, according to the kinematic diffraction theory (cf. chapter 2.3.1). Obviously, the intensity of the emerging wave field is time-independent, but modulated in the direction of the scattering wave vector $\boldsymbol{q}$, which is illustrated in figure 2.24.

The phase shift between incident and diffracted wave is given by

$$\nu = \arctan\left(\frac{\mathrm{Im}(E_f/E_i)}{\mathrm{Re}(E_f/E_i)}\right) + \begin{cases} \pi & \text{for } \mathrm{Re}\,(E_f/E_i < 0) \\ 0 & \text{for } \mathrm{Re}\,(E_f/E_i > 0) \end{cases}. \tag{2.113}$$

By scanning through the BRAGG condition, it changes from $\nu = 0$ to $\nu = \pi$. In doing so, the positions of the standing wave field intensity maxima and minima are also shifted about a half distance of the corresponding BRAGG diffraction planes in scattering wave vector direction. Here, the maxima of the standing wave field are located exactly at the diffraction planes if $\nu = 0$ (cf. figure 2.24(a)) whereas they are located exactly between them if $\nu = \pi$ (cf. figure 2.24(b)).

2.6.2 Secondary signals in XSW

Due to interaction of the standing wave field with the atoms of the sample, several secondary signals occur. The intensity of these signals is modulated according to the intensity of the

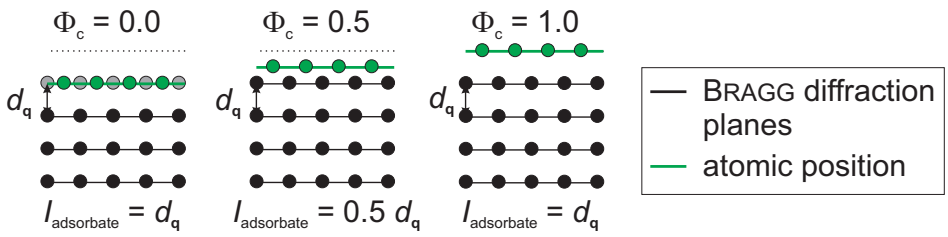

Figure 2.25: The atomic position $l_{adsorbate}$ of a specific adsorbate (green line) in relation to the diffraction plane distance $d_{\boldsymbol{q}}$ of the chosen BRAGG condition for several values of Φ_c. The atomic position can only be determined modulo $d_{\boldsymbol{q}}$.

standing wave field and therefore according to the positions of the wave field maxima and minima, which can be used to determine the atomic positions of a specific element within the sample.

The secondary signals investigated in the presented thesis are inelastic emitted photoelectrons. The corresponding secondary signal yield Y is proportional to the wave field intensity at the position of the atoms where the respective inelastic process is excited. Regarding an ensemble of N identical atoms located at the positions $\boldsymbol{r_i}$, the normalized secondary signal yield Y_N can be calculated from the superposition of all individual signals Y_i and results to

$$Y = \sum_i Y_i \propto \sum_i I_{SW}(\boldsymbol{r_i}) = 1 + R + 2\sqrt{R}\frac{1}{N}\sum_i \cos\left(\nu - 2\pi \boldsymbol{q}\cdot\boldsymbol{r}_i\right) \equiv Y_N. \tag{2.114}$$

Regarding photoelectron emission, dot-shaped atoms can be assumed, which results in an atomic distribution of

$$A(\boldsymbol{r}) = \frac{1}{N}\sum_i \delta(\boldsymbol{r} - \boldsymbol{r}_i). \tag{2.115}$$

Furthermore, the scalar product $\boldsymbol{q}\cdot\boldsymbol{r_i}$ in the argument of the cosine in equation 2.114 can be simplified to

$$\boldsymbol{q}\cdot\boldsymbol{r}_i = |\boldsymbol{q}|\, z_i^q = \Phi_c, \tag{2.116}$$

where z_i^q is the component of $\boldsymbol{r}_i$ parallel to $\boldsymbol{q}$ and Φ_c denotes the *coherent position*. Thus, the total yield can be expressed as

$$Y_N = 1 + R + 2\sqrt{R} f_c \cos\left(\nu - 2\pi\Phi_c\right), \tag{2.117}$$

with the two fitting parameters *coherent fraction* f_c and the *coherent position* Φ_c. They represent the modulus and phase of the $\boldsymbol{q}$th FOURIER component of the atomic distribution function

$$A(\boldsymbol{r}) = \sum_{\boldsymbol{q}} A(\boldsymbol{q}) e^{(-2\pi i \boldsymbol{q}\cdot\boldsymbol{r})} \tag{2.118}$$

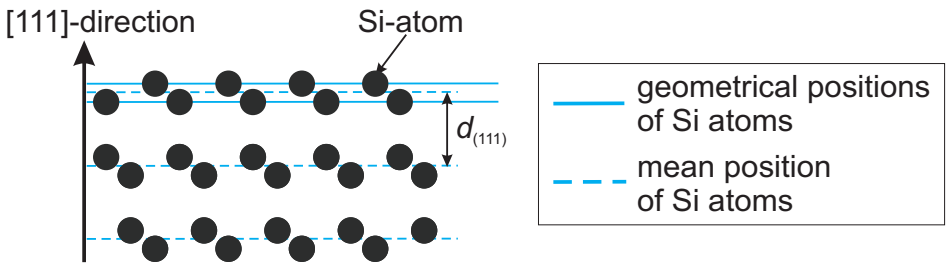

Figure 2.26: Model of a perfect Si crystal with (111) surface and the distance between the diffraction planes $d_{(111)}$. The mean position of the Si atoms is exactly at the diffraction planes, but they are geometrically located at two different sites which slightly differ from the position of the diffraction planes. This decreases the geometrical factor $a_{\boldsymbol{q}}$ of the coherent fraction.

with

$$A(\boldsymbol{q}) = \sum_i e^{(-2\pi i \boldsymbol{q} \cdot \boldsymbol{r}_i)} = f_c \cdot e^{2\pi i \Phi_c}. \tag{2.119}$$

Here, Φ_c can be interpreted as periodic position of the regarded atoms in the direction of the scattering vector $\boldsymbol{q}$. The zero point of this position ($\Phi_c = 0$) is exactly located at the BRAGG diffraction planes of the chosen BRAGG condition. If the value of Φ_c is between zero and unity, the position of the atoms is consequently located between the BRAGG diffraction planes and $l_{adsorbate} = \Phi_c \cdot d_{\boldsymbol{q}}$ gives the atomic position in relation to the corresponding distance of the diffraction planes $d_{\boldsymbol{q}}$. At $\Phi_c = 1$ the atoms are located again at the BRAGG diffraction planes. Therefore, the atomic position can only be determined modulo $d_{\boldsymbol{q}}$. To obtain unambiguous information about the position of the regarded atoms in all spatial directions, it is necessary to measure at least at three non-equivalent BRAGG conditions. Thus the positions can be triangulated from the full data set. The interpretation of the coherent position is illustrated in figure 2.25 where the atomic position of an arbitrary adsorbate is shown for several values of Φ_c.

The coherent fraction results to unity if identical atoms are located at a single bounding site (one-position model; cf. figure 2.25) and if thermal vibrations are neglected. The coherent fraction is decreased if these atoms are statistical distributed around these bonding sites. In this case f_c denotes the part of atoms, which are located exactly at the position given by Φ_c. This is, however, not correct for complicated structure models, where the atoms are located at different atomic positions. Here, the coherent fraction is given by

$$f_c = C a_{\boldsymbol{q}} D_{\boldsymbol{q}} \ , \tag{2.120}$$

where C denotes the ordered part of the atoms. Thermal lattice vibrations of the specific atoms are included by the DEBYE-WALLER factor $D_{\boldsymbol{q}}$, which results in a decrease of the coherent fraction, since the atoms oscillate around their mean position. Furthermore, $a_{\boldsymbol{q}}$ is a geometrical factor, which is used if atoms are located at several non-equivalent adsorption

sites. The influence of $a_{\boldsymbol{q}}$ can be illustrated for instance with an ideal Si crystal. Neglecting thermal vibrations, coherent fraction and position obtained at the $\mathrm{Si}(111)_{bulk}$ Bragg peak condition are $f_c^{111} = 1/\sqrt{2}$ and $\Phi_c^{111} = 0$. Although the crystal is assumed to be perfect, the coherent fraction is considerably lower than unity. This is caused by the geometrical position of the silicon atoms. As shown in figure 2.26, the *mean* atomic position is exactly at the diffraction planes ($\Phi_c^{111} = 0$), but the particular atoms are located *geometrically* at two different sites, which lowers the value of f_c^{111}.

2.7 X-ray photoelectron spectroscopy

X-ray photoelectron spectroscopy is a technique based on the photoelectric effect. The sample is irradiated with X-ray photons providing sufficient energy to excite core-level electrons until they leave the material. The kinetic energy and number of these photoelectrons is detected to determine the empirical formula as well as the chemical and electronic state of the sample. XPS is a surface sensitive method, since the mean free path of the excited photoelectrons in solid state materials is in the region of several Å to several nanometers depending on the energy of the exciting X-ray photons (up to several keV using synchrotron radiation; cf. figure 2.27). Because the XPS measurements only amount to a small proportion of the presented thesis, just a brief introduction to this technique will be given in the following.

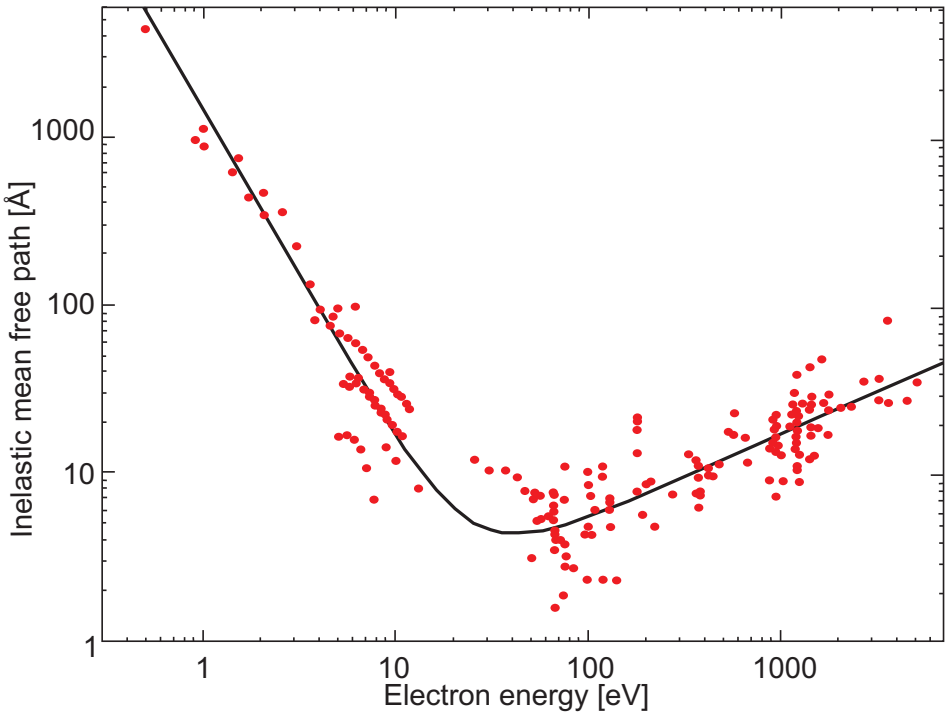

Figure 2.27: Mean free path of inelastic scattered electrons in solids depending on the electron energy. Image taken from [33].

The photoelectron excitation process is shown schematically in figure 2.28. Here, an X-ray photon is adsorbed by an atom of the solid state material and the photon energy is transferred to a core-level electron. If the photon energy E_{photon} is sufficient to overcome the effective binding energy $E_{bin,eff}$ of the electron, it is removed out of the material and the kinetic energy E_{kin} of the electron results in

$$E_{kin} = E_{photon} - E_{bin,eff}. \tag{2.121}$$

In general, $E_{bin,eff}$ is composed of the element specific binding energy of the electron in relation to the FERMI energy E_f of the material, the work function Φ of the detector and additional correction terms to include many-body effects [34]. Furthermore, $E_{bin,eff}$ is slightly shifted according to the chemical surrounding of the atom. Therefore, a sophisticated chemical analysis of the sample surface, like the elemental composition or the oxidation state of the atoms, is possible. Information about the quantity of a specific element at the sample surface can be obtained by analysis of the integral intensity of the peaks which are characteristic for the studied element.

In the presented thesis, XPS measurements are combined with the XSW technique to get both the chemical composition and the element specific structure of the thin films. For this purpose, only photoelectrons of a specific kinetic energy corresponding to the investigated element are detected during variation of the standing wave field. Thus, the positions in relation to the wave field are obtained for this specific element.

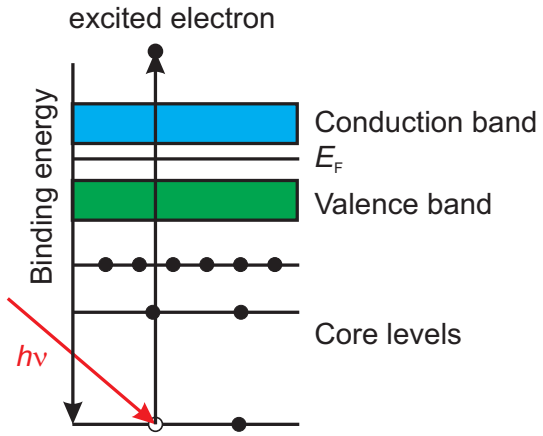

Figure 2.28: Illustration of the photoelectron excitation process, image taken from [35] and adapted. An X-ray photon is absorbed by a solid state material and the energy is transfered to a core level electron. This electron is excited and leaves the system. Here, a part of the additional energy is lost to summon the binding energy $E_{bin,eff}$ of the solid state material. The other part becomes the kinetic energy E_{kin} of this so-called *photoelectron*.

3 Investigated materials

This chapter gives an overview of the properties of the investigated materials including the silicon substrate, the praseodymia film and the chlorine adsorbate used to passivate the substrate. Furthermore, established facts about the interaction of the evaporated materials with the silicon substrate are presented. This is useful for further understanding of the obtained results.

3.1 Silicon

The element Silicon is a metalloid with the atomic number 14 and a melting point of 1414°C. It is located at the 4th main group of the periodic table and crystallizes in the diamond cubic structure which can be built up from two face-centered cubic (fcc) lattices separated by 1/4 of the unit cell in each direction (cf. figure 3.1(a)). The unit cell contains eight atoms and its lattice constant is 5.431 Å.

Ultra-pure Si presents the dominating semiconductor material platform for microelectronic applications since it provides many advantageous properties. It is the second most occurring element in the crust of earth, therefore it is easy to convey and very cheap. It keeps its semi conducting properties even at high temperatures and forms a sharp insulating native oxide layer (SiO_2) which can be used as semiconductor/dielectric interface. Furthermore, its electrical properties can be tuned in a wide range by doping with elements like boron or phosphor. Because Si is a standard material for the semiconductor industry, its structure and physical properties are well understood.

To investigate the growth of praseodymia films on passivated and non-passivated substrates, two types of boron doped Si(111) crystals were used. The first types of substrates are Si wafers of $(525 \pm 15)\mu$m thickness and a surface miscut of $(0.35 \pm 0.15)°$. The dopant dependent resistivity is between 5 Ωcm and 15 Ωcm. The second types of substrates were only used for

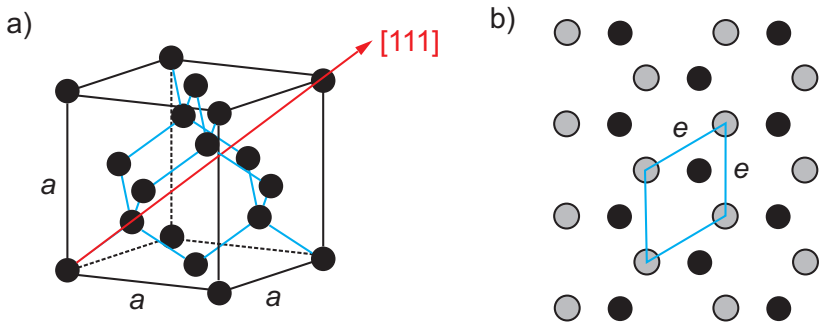

Figure 3.1: (a) Si unit cell with diamond structure and indicated $[111]_{\text{Bulk}}$-direction. (b) The unreconstructed Si(111) surface with indicated surface unit cell. The lateral lattice parameter is denoted as e. Dark colored atoms are located in the second layer underneath the surface layer.

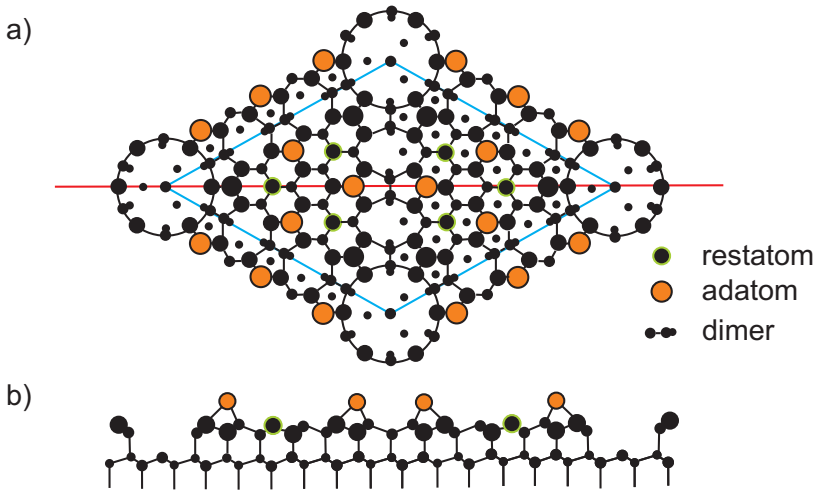

Figure 3.2: (a) Top view on the reconstructed Si(111)(7x7) superstructure (surface unit cell is indicated with blue lines). (b) Cross section through the surface unit cell (red line). Small atoms are located behind (a) or underneath (b) the bigger drawn atoms.

XSW measurements at beamline BW1 at DESY (Hamburg, Germany). Here, samples with a special geometry and a thickness of at least 2 mm were cut out of Si single crystals. This was done because thin wafers always exhibit small height variations of the atomic planes, if they are fixed on a sample holder. This is disadvantageous for XSW measurements since these height variations falsify the obtained results. Thick Si substrates are much more resistant against this effect. No defined surface miscut can be observed for this type of substrate due to the preparation method (cf. chapter 4.3). The dopant dependent resistivity is also between 5 Ωcm and 15 Ωcm.

The surface properties of the Si substrate are important to understand praseodymia film growth or adsorbation processes of chlorine. This is because surface energy, number of dangling bonds and lattice mismatch between substrate and film depend on the structure of the chosen surface. In the presented work the Si(111) surface is used as mentioned above. Its unreconstructed, rhombohedral surface unit cell with a lateral lattice parameter of $e = 3.840$ Å is shown in figure 3.1(b). The vertical lattice constant is $d = 3.136$ Å and with the [111]-direction as rotation axis, a six-fold symmetry of the surface structure can be observed. However, taking the different vertical positions of the topmost Si atoms into account, the symmetry of the surface is reduced to three-fold. This is also important regarding the performed diffraction experiments (SPA-LEED and (GI)XRD).

If clean Si(111) surfaces are prepared under UHV conditions, reconstruction of the surface takes place. This is because dangling bonds are formed at the unreconstructed surface, which is energetically unfavorable. If the sample is heated to temperatures of 380°C to 950°C the surface energy is minimized by reconstruction of the surface atoms forming a Si(111)(7x7) superstructure [36]. This structure was described first in 1986 by Takayanagi et al. [37], suggesting a dimer adatom stacking fault model (DAS-model), which is shown in figure 3.2.

Here, the unit cell contains 102 atoms in the first two atomic layers and the number of dangling bonds is reduced from 49 to 19 per unit cell. The lateral lattice parameter is $e = 27.19$ Å [38] and therefore seven times larger compared to the unreconstructed surface unit cell.

This complicated surface superstructure is negligible determining the structure of the praseodymia film grown on top of the Si(111) surface since it disappears when the oxide film is adsorbed. Here, only the lattice parameters of the unreconstructed Si(111) surface unit cell are necessary to understand the presented results. To describe the adsorption processes of single chlorine atoms, however, the location of Si adatoms and Si restatoms within the Si(111)(7x7) surface unit cell (cf. figure 3.2) is of special interest as it is shown in the following.

3.2 Praseodymia

Main subject of the presented work is the investigation of thin praseodymium oxide (also called praseodymia) films grown on Si substrates. Metallic praseodymium is a rare earth element of the lanthanide group with an atomic number of 59 and a melting point of 935°C. It is a strong oxidant and forms Pr-oxides with different stoichiometries in the range of $PrO_{1.5}$ to $PrO_{2.0}$ whereas the Pr-cations can occur in the oxidation states Pr^{3+} and Pr^{4+}.

The phase diagram of praseodymia and the three commonly mentioned *bulk* praseodymia structures PrO_2, cubic Pr_2O_3 (cub-Pr_2O_3) and hexagonal Pr_2O_3 (hex-Pr_2O_3) are shown in figure 3.3. Here, Bulk PrO_2 represents the oxide phase with highest oxygen content among all the other stoichiometries. It crystallizes in the fluorite structure with four praseodymium and eight oxygen atoms per unit cell and a lattice parameter of $a = 5.394$ Å. Here, all Pr-ions are in the Pr^{4+} oxidation state. From this fluorite structure, the other cubic and pseudo cubic

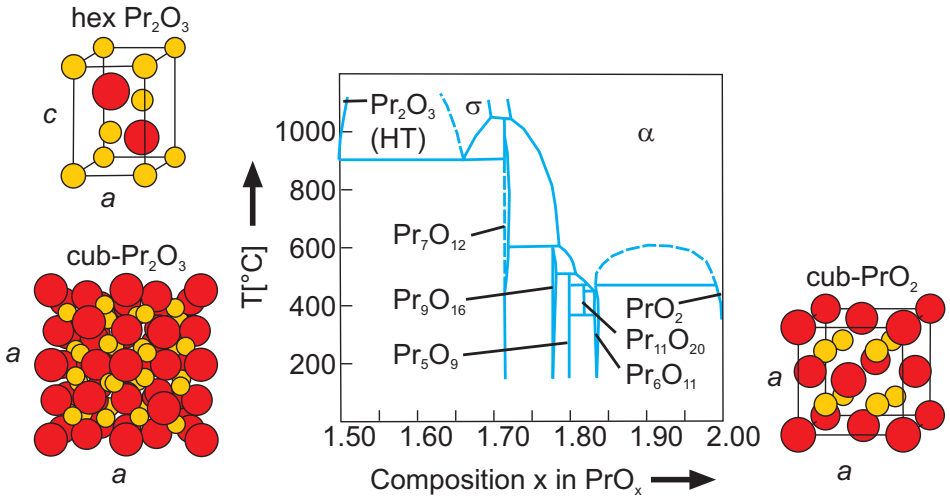

Figure 3.3: Partial phase diagram of bulk praseodymium oxide. Illustrated are the equilibrium stoichiometries, which depend on temperature and oxygen ambient pressure. Unit cells of the well-known hexagonal Pr_2O_3, cubic Pr_2O_3 and PrO_3 oxide phases can be seen at their corresponding edge of the phase diagram.

oxide phases can be deduced. The phase with the lowest oxygen content, which exhibits only Pr^{3+} ions, is the sesquioxide (Pr_2O_3). It can occur in hexagonal or cubic (bixbyite) structure whereas cub-Pr_2O_3 is irreversible transformed into hex-Pr_2O_3 at temperatures above 800°C [39]. Bulk cub-Pr_2O_3 exhibits a lattice parameter of $a = 11.152\,\text{Å}$ with 32 praseodymium and 48 oxygen atoms per unit cell. In contrast, the hex-Pr_2O_3 unit cell only contains 2 praseodymium and 3 oxygen atoms. Its lattice parameters are $a = 3.859\,\text{Å}$ and $c = 6.013\,\text{Å}$.

Further, defined oxide phases occur between the Pr-sesquioxide and the Pr-dioxide. As it is universally accepted, that these phases can be described in a homologous series using the chemical formula Pr_nO_{2n-2} ($n = 4, 7, 9, 11, 12, \infty$) [40]. In particular, in the composition range of $PrO_{1.833}$ to $PrO_{1.714}$, five different, ordered oxygen phases occur. These phases are often called non-stoichiometric due to their complex chemical formula, but the corresponding bulk structures show well defined stoichiometries (e.g. $PrO_{1.833} \rightarrow Pr_6O_{11}$) and particular crystallographic unit cells. To describe these unit cells it is useful to start with the basic fluorite structure and remove oxygen atoms in agreement with the desired stoichiometry. Thus, oxygen vacancies are formed in the unit cells, which may be arranged periodically [41]. This results in superstructures of the fluorite unit cell and reflects the high mobility of the oxygen sublattice [8]. Here, the praseodymium atoms undergo only small position variations due to the missing Pr-O bonds, reducing the crystal symmetry and forming larger unit cells as mentioned above for bulk cub-Pr_2O_3. The equilibrium oxide phase, which is obtained after oxidation or reduction processes, is determined by oxygen partial pressure, temperature and time.

Miscibility gaps can be observed between $PrO_{2.0}$ and $PrO_{1.833}$ as well as between $PrO_{1.714}$ and $PrO_{1.5}$. Whereas the first gap is well defined, former studies observed a region between $PrO_{1.714}$ and $PrO_{1.5}$ where additional non-stoichiometric, disordered oxide phases occur [42]. Finally, it was found for both extreme oxide phases that it is difficult to reach the exact chemical formulas of $PrO_{2.0}$ or $PrO_{1.5}$. For bulk praseodymia it was reported, that oxidation from $PrO_{1.833}$ to $PrO_{1.99}$ in 1 atm oxygen at 286°C takes 2000 minutes [42]. The crystallites of the praseodymia films investigated in this work are smaller (approximately 100 nm particle size) compared to the studied powder particles mentioned above so that oxidation might proceed faster, but still undesirable time scales are expected for full oxidation to $PrO_{2.0}$. Regarding the $PrO_{1.5}$ oxide stoichiometry, Rudenko et al. reported that cub-Pr_2O_3 is only energetically favorable compared to hex-Pr_2O_3 if excess oxygen is present [43]. Therefore, the reduction to an exact $PrO_{1.5}$ stoichiometry seems to be always accompanied by a phase transition from cub-Pr_2O_3 to hex-Pr_2O_3 while cub-Pr_2O_3 has to be identified actually as cub-$Pr_2O_{3+\Delta}$. Here, Δ denotes an additional amount of oxygen.

3.2.1 Praseodymia films on Si(111)

In the following, known facts about growth and structure of thin praseodymia films on Si(111) substrates are presented which are useful for the interpretation of the obtained results.

Crystalline praseodymia films with hex-Pr_2O_3 structure and (0001) orientation can be grown on Si(111) at a substrate temperature of 625°C [9, 44]. Evaporation is performed by molecular beam epitaxy (MBE) whereas high growth rates of about 0.1 nm/s are necessary to obtain

praseodymia films with crystalline quality. It was shown that lower growth rates of 0.06 nm/s lead to the formation of amorphous Pr-silicates and Pr-silicides on top of the substrate instead of a crystalline oxide layer [45].

It was further shown, that hexagonal films of 5 nm thickness can be transformed to cubic structure by post deposition annealing (PDA) in oxygen or nitrogen atmosphere. At this, partial pressures of 10^{-5} mbar oxygen or 1 atm nitrogen and annealing temperatures of 600°C up to 700°C lead to cub-Pr_2O_3 films [10, 46]. With higher oxygen pressures of 1 atm and temperatures in the range of 300°C up to 700°C cubic films close to the PrO_2 stoichiometry are formed [11]. All films are rotated by 180° with respect to the substrate structure (B-type orientation) and it applies that the film is closer to the PrO_2 stoichiometry, the higher the annealing temperature was. However, films with exact PrO_2 structure could not be observed with the used PDA parameters [47]. Detailed analysis further showed, that the films were separated into laterally coexisting oxide species with significant different oxygen content (two-column model) [47]. Below 300°C the film still exhibited hex-Pr_2O_3 structure.

Figure 3.4 shows the bulk surface unit cell structures of $PrO_2(111)$, cub-$Pr_2O_3(111)$ and hex-$Pr_2O_3(0001)$ as they are expected after film growth on Si(111) and the corresponding vertical lattice parameters. It can be observed that the size of the hex-$Pr_2O_3(0001)$ surface unit cell $a = 3.859$ Å almost matches the surface unit cell of the Si substrate (+0.5 %). In contrast, the size of the cub-$Pr_2O_3(111)$ surface unit cell ($e = 15.772$ Å) is about four times larger compared to the Si substrate due to the decreased crystall symmetry and therefore does not fit directly. However, an arrangement of four by four Si surface unit cells fits cub-$Pr_2O_3(111)$. Here, a mismatch of +2.7 % is observed. Because of that, cub-Pr_2O_3 films tend to form antiphase domain boundaries during growth on Si(111) which is disadvantageous for heteroepitaxial films. The surface unit cell of $PrO_2(111)$ amounts to $a = 3.814$ Å which is 0.7 % smaller than the Si(111) surface unit cell.

Our previous work showed that the surface unit cells of the praseodymia films grown on Si(111) exhibit hex-Pr_2O_3 lattice parameters even after phase transition to the cubic structure [11, 47]. In this case, they cannot adopt their bulk surface unit cell sizes due to the lateral pinning which results in tetragonal distortion of the oxide films. Since this effect may have a strong impact on the positions of the highly mobile oxygen atoms and vacancies in the praseodymia system, the film structures are not necessarily the same obtained in the bulk material.

Almost no silicate interface formation between oxide film and substrate was observed after the growth of hex-Pr_2O_3 films on Si(111) and even not after subsequent UHV annealing [9, 46]. However, after phase transition to cubic films by PDA in 1 atm oxygen at elevated temperatures (> 300°C), the formation of a silicate interface layer with significant thickness was reported in several works [11, 47, 48]. It was shown that this interface layer consists of two sublayers, namely a Pr-rich one close to the oxide and an SiO_2-rich one close to the substrate [47, 49]. Furthermore, the composite interface thickness increases with higher PDA temperatures or higher oxygen partial pressures during PDA. Weisemoeller et al. [47] concluded that this is mainly due to the increasing layer thickness of the Pr-rich part.

Since it was reported that the growing interface layer causes negative effects on the dielectric properties of the oxide film [18], it is of high interest to surpress the interface formation during

praseodymia film preparation. Besides the investigation of phase transitions in praseodymia films, interface formation and growth during film preparation as well as its prevention is an

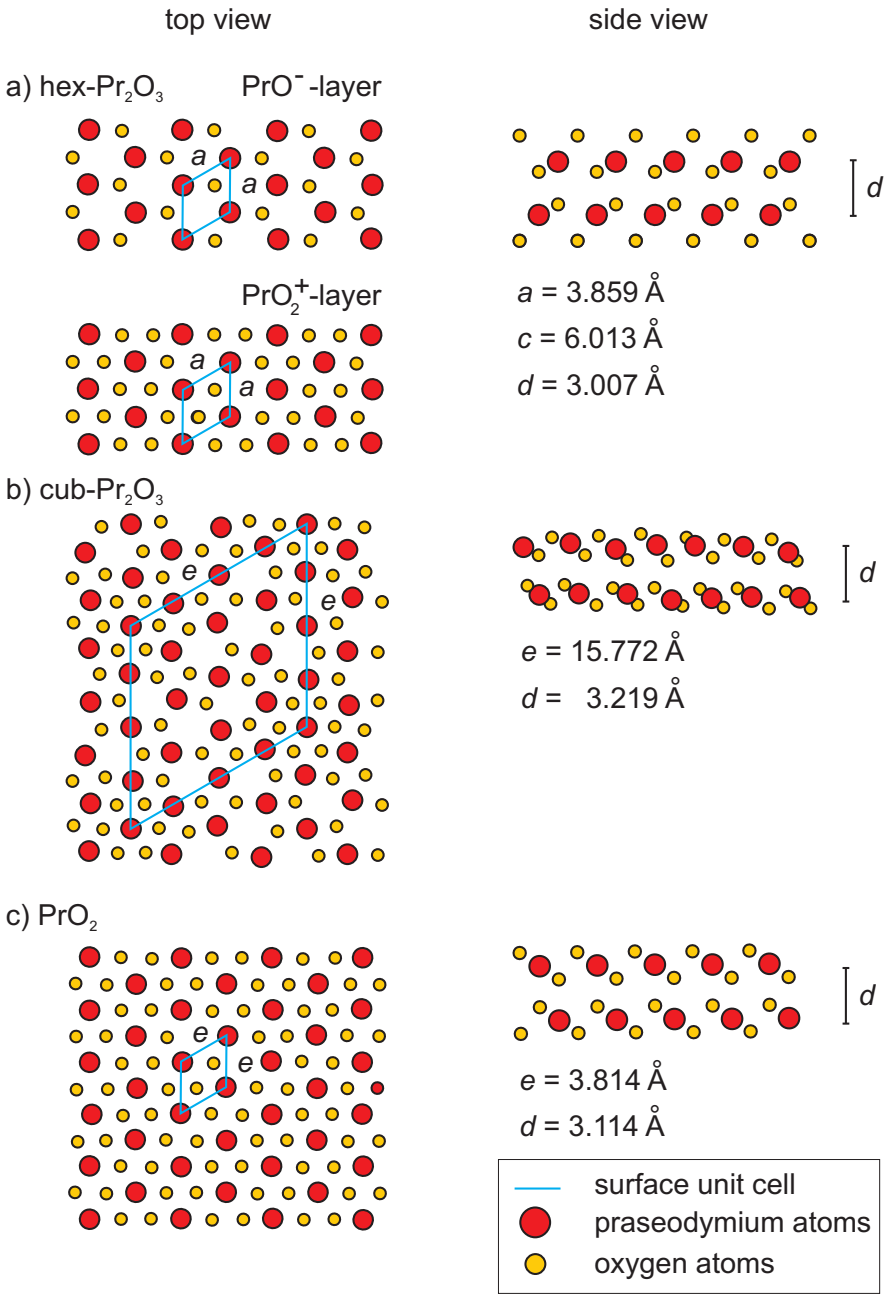

Figure 3.4: Top and side view on the (111) surfaces of the well known praseodymia phases hex-Pr_2O_3, cub-Pr_2O_3 and PrO_2. The surface unit cells are indicated with blue lines and their lateral lattice parameters are denoted as a (hexagonal phase) and e (cubic phases). The layer distances perpendicular to the [111] direction are labeled as d

additional subject of this thesis.

3.3 Chlorine adsorbates on Si(111) surfaces

As mentioned above, investigations on suppressing the interface formation during praseodymia film growth on Si(111) were performed. The silicon surface was passivated before film growth by adsorbing chlorine atoms to prevent reactions at the interface and interdiffusion of Si, Pr and O atoms.

Chlorine adsorption on Si(111) is well studied by several experimental and theoretical methods as reported by Lifshits at al. [50]. The evaporation of Cl_2 molecules on Si(111)(7x7) reconstructed surfaces first results in bonding of single Cl atoms with both Si adatoms and remaining dangling bonds of the Si surface unit cell (cf. figure 3.2). With further chemical interaction of Cl atoms with the Si surface at RT, Si-Cl_2 and Si-Cl_3 complexes are formed [51]. In doing so, the (7x7) reconstruction is retained [52], which is also supported by theoretical (ab initio) studies [53, 54].

Subsequent heating of the sample to temperatures above 400°C results in a reconstruction of the Si(111)(7x7)-Cl surface to a Si(111)(1x1)-Cl surface. This process is accompanied by stepwise forming of several intermediate surface structures [55], since dimer chains as well as the parts of the Si(111)(7x7) surface units cells with stacking fault have to be successively broken open. Whereas Si-Cl_3 complexes are removed completely from the surface at annealing temperatures of 420°C, Si-Cl_2 complexes partly remain until annealing at 680°C. After annealing, the surface is covered with one monolayer (ML) chlorine atoms located at T adsorption sites (cf. figure 3.5). The bonding length between Si and Cl atoms is in this case 2.05 ± 0.03 Å. This monolayer can be removed completely by annealing at 850°C [56].

It was found that the oxidation of reconstructed Si(111)(1x1)-Cl surfaces, which are also used in this thesis, is suppressed during heating in O_2 atmosphere compared to non passivated Si(111)(7x7) surfaces [57]. Since one can assume from results of Ono et al. [49] that oxygen diffusion into the Si substrate initiates the Pr-silicate formation, this might be an approach

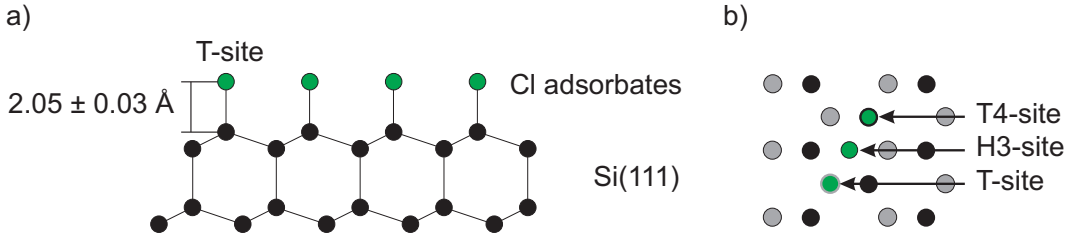

Figure 3.5: (a) Si(111)(1x1)-Cl reconstruction caused by adsorption of one monolayer chlorine on the Si(111) surface. (b) Top view on the Si(111) surface to illustrate different adsorption sites. T(op)-Site: the Cl atom is adsorbed on top of a Si atom located in the first layer; $T(op)_4$-Site: the Cl atom is adsorbed on top of a Si atom located in the second layer; $H(ollow)_3$-Site: the Cl atom is adsorbed at the center of the hexagon formed by the two topmost layers.

to suppress the formation of an interface layer. However, Florio et al. showed that 60 % of the surface coverage is lost after annealing for 30 min at 480°C [52]. Therefore it has to be taken into account that the passivation of the Si surface may not be stable at elevated evaporation temperatures and evaporation times necessary for praseodymia film growth with serveral nanometres film thickness (about 500°C and 15 min; cf. chapter 4.5.2).

4 Experimental setup

This chapter deals with the setup of the experimental methods used to prepare and investigate the samples. At first, the different setups used for sample preparation are introduced. The second part gives an overview on the setups of the experimental methods to investigate these samples and finally the software used for data analysis is presented.

4.1 Sample preparation of praseodymia films on non-passivated Si(111)

The samples used to investigate the influence of PDA and oxygen plasma treatment of praseodymia films on non-passivated Si(111) were preparated by the IHP GmbH in Frankfurt(Oder). Here, single crystalline Si-wafers provided by the Siltronic AG served as substrates. These wafers have a diameter of 4" and [111] surface orientation with $(0.35 \pm 0.15)^\circ$ miscut, which is mainly oriented in $[1\bar{1}0]$ direction. This results in mean terrace-widths of $(360 - 900)$ Å. The wafers were doped with boron, exhibiting a resistivity of $(5 - 15)\,\Omega$cm.

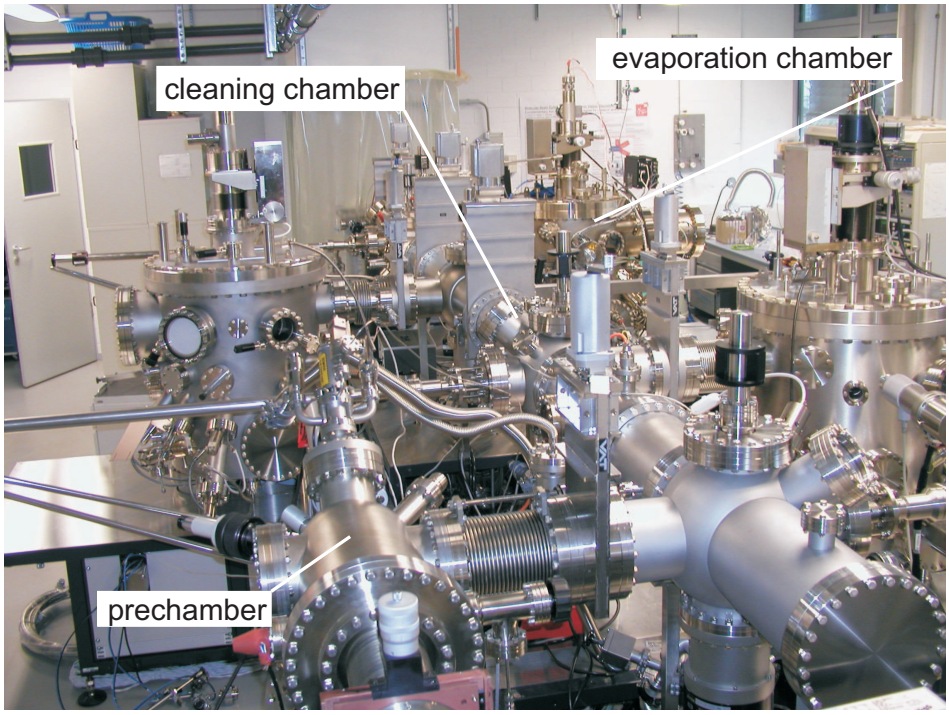

Figure 4.1: UHV chamber at the IHP in Frankfurt(Oder). The actual evaporation of praseodymium oxide takes place in the indicated evaporation chamber.

Cleaning of the samples was performed by wet-etching using a standard recipe containing several etching and cleaning steps [44] before they were transferred into the prechamber (cf. figure 4.1). Here, samples and sample-holders were degassed in the prechamber (10^{-8} mbar base pressure) by annealing at 200 °C. Afterwards, they were transferred into the cleaning chamber (10^{-10} mbar base pressure) and annealed to 700 °C, leading to a high-quality Si(111)

surface accompanied by a (7x7)-reconstruction, which was verified by LEED measurements.

Praseodymia film growth was performed via molecular beam epitaxy (MBE) after sample cleaning, which is the chosen technique for fundamental investigations regarding the behavior and practicability of material systems. This is in contrast to chemical vapor deposition (CVD), which is typically used for mass production of thin film systems. The MBE system used to prepare the samples studied in this work, was of the type DCA 600. Here, an electron beam is focused directly into a crucible, heating up the praseodymia powder (Pr_6O_{11}) to evaporation temperature, which simultaneously reduces the starting material to Pr_2O_3. A vapor pressure of about 10^{-4} mbar is reached for Pr_2O_3 at a temperature of 1400 °C [58], which is adequate for the growth process.

During the evaporation process, the growth rate of the praseodymia films was adjusted to 0.1 nm/s and praseodymia films with layer thicknesses in the range of 4 nm up to 12 nm were grown. In doing so, the substrate was heated to 625 °C and additionally rotated to avoid uneven praseodymia film thicknesses due to minor inhomogeneities of the particle beam. The background pressure during evaporation was in the range of 10^{-8} mbar.

This method leads to samples with twin-free Pr_2O_3 films of hexagonal structure. These were transferred ex situ into an oven, where they were heated for 30 min in an oxygen partial pressure of 1 atm at temperatures of 450 °C and 700 °C to obtain PrO_2 films with cubic (fluorite) structure [47] or in nitrogen of 1 atm at a temperature of 600 °C to obtain Pr_2O_3 films with cubic (bixbyite) structure [46]. In both cases, the gas flow was kept constant during annealing.

The wafers annealed in oxygen at 700 °C and those annealed in nitrogen were transported to Osnabrück. Here, samples with sizes of about 8 mm x 30 mm were cut out and transferred into a UHV chamber (10^{-10} mbar base pressure; cf. figure 4.4) where they were annealed by direct current to several temperatures up to 600 °C for 30 min. These samples were investigated in situ by SPA-LEED and ex situ by XRR, XRD and GIXRD at HASYLAB/Hamburg. The samples annealed in oxygen at 450 °C were sent to Bremen to perform oxygen plasma treatment as described in the next paragraph.

4.2 Oxygen plasma treatment of praseodymia films

Oxygen plasma treatment of the praseodymia films was performed at the IACP in Bremen to obtain fully oxidized cubic PrO_2 structures. Here, the samples (size of about 2 mm x 7 mm) are transferred to a UHV-chamber with a base pressure of 10^{-9} mbar providing a plasma source where a capacitive-coupled radio-frequency (RF) plasma field is generated (cf. figure 4.2). Details concerning operation and setup of the plasma source can be found in reference [59]. In this system, the sample serves as phase electrode so that the surface is directly exposed to the plasma field. During oxygen plasma treatment, an oxygen partial-pressure of 9 mbar with constant gas flow of 15 sccm (standard cubic centimeter per minute) was adjusted. The sample was kept for 60 minutes within the plasma field with a performance of 30 W. After plasma treatment, XPS and LEED measurements were carried out to precharacterize the samples before they were sent to HASYLAB/Hamburg under clean oxygen atmosphere. Here XRR, XRD and GIXRD measurements were performed.

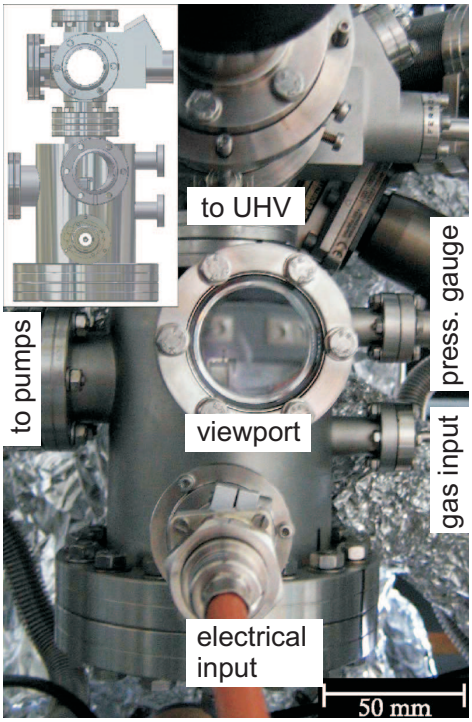

Figure 4.2: UHV-chamber with plasma source at the IACP (taken from [59]; inlet: construction view).

4.3 Sample preparation of praseodymia films on Cl-passivated Si(111)

Chlorine passivated samples were prepared in a UHV chamber at beamline BW1 at HASYLAB/Hamburg (cf. figure 4.3) . First, RCA-cleaned [1] [60] Si(111) substrates were transferred into the UHV preparation chamber and annealed by direct current at 875 °C for 5 minutes in order to remove the native SiO_2 from the surface and to get a (7x7)-reconstruction. The samples were passivated by evaporation of molecular Cl_2 from a AgCl chemical source onto the surface for 30 min at 600 °C substrate temperature. This results in a (1x1)-reconstruction at the surface, which was verified by LEED measurements.

Praseodymia film growth was performed by MBE using an evaporator with indirectly heated material (Pr_6O_{11} powder). Here, a tantalum crucible is heated up by electron bombardment at a high voltage of 1000 V, which further heats the material to evaporation temperatures above 1400 °C as explained above. The substrate temperature during film growth was kept at 500 °C, the base pressure was about 10^{-8} mbar. Due to the bad thermal conduction properties of praseodymia powder, only small growth rates of about 0.003 nm/s could be achieved. After the evaporation process, the samples were annealed for 15 minutes at 500 °C in $1.5 \cdot 10^{-7}$ mbar oxygen partial pressure. On these samples in situ LEED, XSW and high energy XPS investigations were performed complemented by ex situ XRR studies.

[1] Here, the abbreviation RCA denotes the Radio Corporation of America where this cleaning technique was developed in 1965.

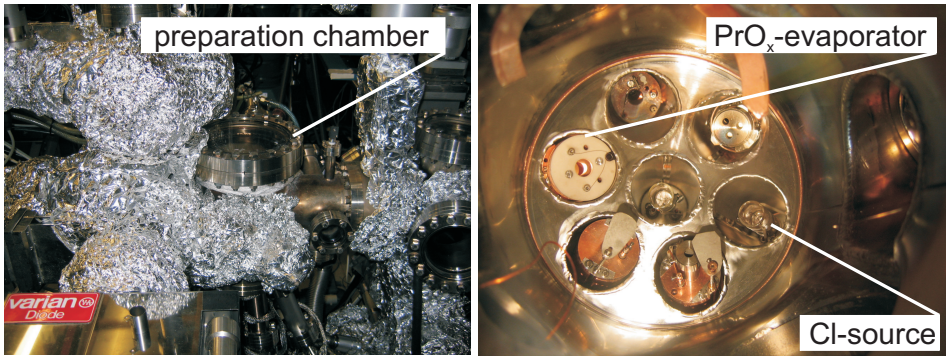

Figure 4.3: (a) Preparation chamber at the beamline BW1 at HASYLAB/Hamburg. (b) Top view into the preparation chamber.

4.4 Experimental setup in Osnabrück

All samples prepared in Osnabrück were precharacterized by spot profile analysis low energy electron diffraction (SPA-LEED) to investigate the crystallinity of the surface. The SPA-LEED device is located within the preparation chamber so that in situ investigations are possible (cf. figure 4.4). The experimental setup is described in the following.

4.4.1 SPA-LEED

The SPA-LEED device used to obtain high resolution diffraction patterns is a second generation LEYBOLD system developed from the standard LEED method [61]. In contrast to the standart LEED system, the electron source (e-gun) is located on one level with the electron detector (channeltron). Electrons are accelerated towards the sample with energies of 0 eV up to 500 eV and the incident angle of the beam with respect to the sample surface can be varied by a deflection unit (octopole; cf. figure 4.5). Whereas the incident angle is varied to scan the reciprocal space, the angle between incident and diffracted beam is kept constant during measurement so that a larger part of the reciprocal space can be measured compared to standard LEED systems. After diffraction at the sample, the electrons reenter the octopole where they are detected by the channeltron on which the electron beam is focused by a multi-lense system. Another main advantage compared to the standard LEED is that the specular surface diffraction rod is not covered by e-gun or sample holder. This allows a detailed spot profile analysis, which provides information about vertical layer distances, surface roughness and surface morphology in addition to the lateral structure and sizes of the surface unit cells. Furthermore, the transfer width of the SPA-LEED system (1000 Å) is about ten times larger compared to standard LEED methods (100 Å) allowing to investigate larger crystalline structures on the sample surface. Further details of the SPA-LEED method can be read in [61, 62, 63].

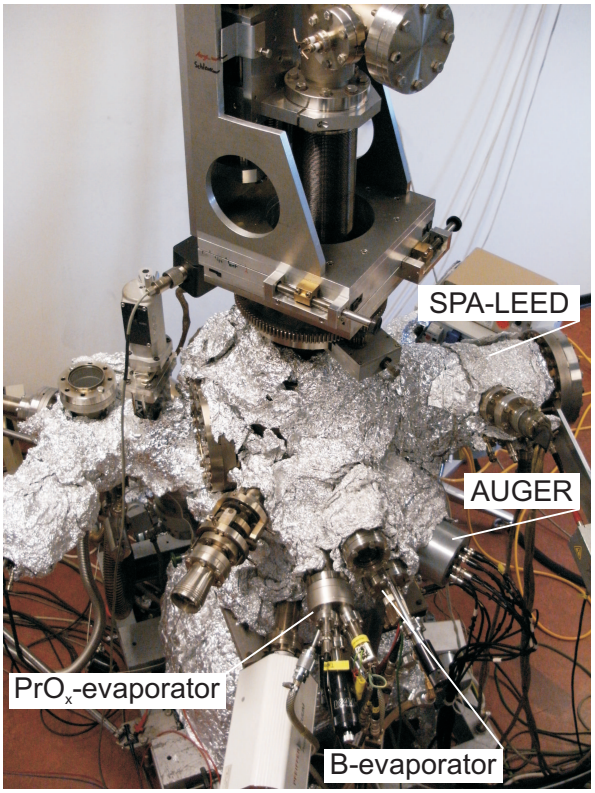

Figure 4.4: UHV chamber at Osnabrück.

4.5 Experimental setup at HASYLAB

A great deal of the measurements presented in this work (XRR, XRD, GIXRD, XSW and high-energy XPS) were performed at HASYLAB/Hamburg. Since photons in the X-ray wavelength region with high brilliance are necessary to limit the measurement time and also to offer adequate statistics, synchrotron radiation was used for the experiments. The radiation is generated by DORIS III, a second generation synchrotron, where pre-accelerated positrons are kept at an energy of 4.45 GeV and brought on a slalom course by wigglers, undulators and dipole magnets. As a result, photons in the wavelength region of X-ray and extreme hard UV are emitted, which can be used for experiments at more than 30 different beamline stations. In our work XRR, XRD and GIXRD measurements were carried out at beamlines W1 and BW2, whereas measurements using X-ray standing waves were performed at beamline BW1. A detailed description of the respective experimental setups can be found in the following chapters.

4.5.1 Setup at beamlines W1 and BW2

At beamlines W1 and BW2, synchrotron radiation is generated by wigglers consisting of linear arrays of dipole magnets, which are typically arranged in a HALBACH array. This results in

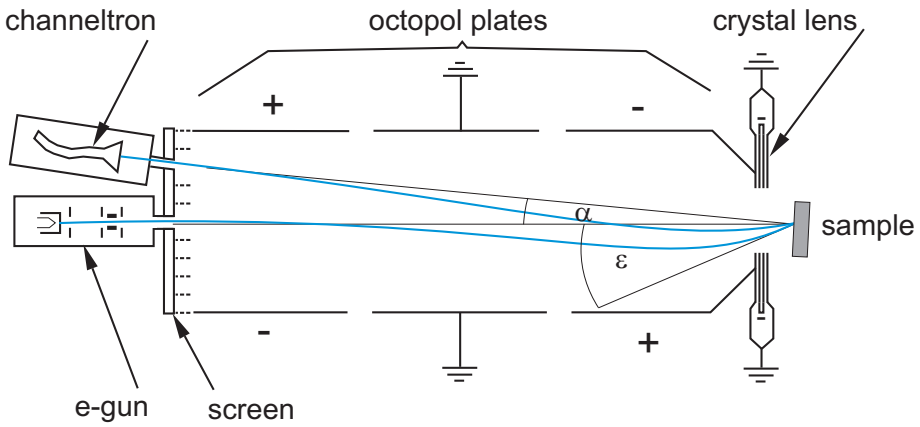

Figure 4.5: Schematic setup of the LEYBOLD SPA-LEED system. One of the possible beam paths is indicated with blue lines.

emission of divergent and broadband synchrotron radiation with high intensity. Double-crystal Si(111) monochromators are used to extract photons with a particular wavelength according to the requirements of the experiment. In our work, measurements were performed with photon energies of 10 keV and 10.5 keV, corresponding to X-ray wavelengths of 1.24 Å and 1.18 Å. A system of Au-coated mirrors focuses the beam on the position of the sample. Furthermore, a slit system can be used to adjust the size of the beam at the sample. The intensity of the beam can also be attenuated by motor controlled Al-absorbers with different thicknesses, which are moved into the beam to ensure that the diffracted intensity is always within the detector limits. The scattered photons are detected either by a NaI(Tl) point-detector or a Si-strip line-detector (MYTHEN, [64]).

The setup of both beamlines is quite similar. The main difference between beamline W1 and BW2 is the number of dipole magnets used to build up the wiggler. 32 dipole magnets (16 periods) are used for the wiggler at W1 compared to 56 dipole magnets (28 periods) of the wiggler at BW2. Since the intensity of the synchrotron radiation is proportional to the number of dipole magnets, beamline BW2 provides significantly higher intensity than beamline W1.

At both beamlines, movement of sample and detector is performed by identical six-circle diffractometers (cf. figure 4.6(a)). According to the requirements of the experiment, the sample can be mounted in different ways on the diffractometer. Three different measurement geometries were used in this work to perform XRR, XRD and GIXRD investigations:

1. horizontal alignment

   The sample is mounted on a sample holder in the pivot point of the diffractometer (cf. figure 4.6(a)) with the surface aligned parallel to the main rotation axis. During measurement only the incident angle of the beam onto the sample surface (om) and the

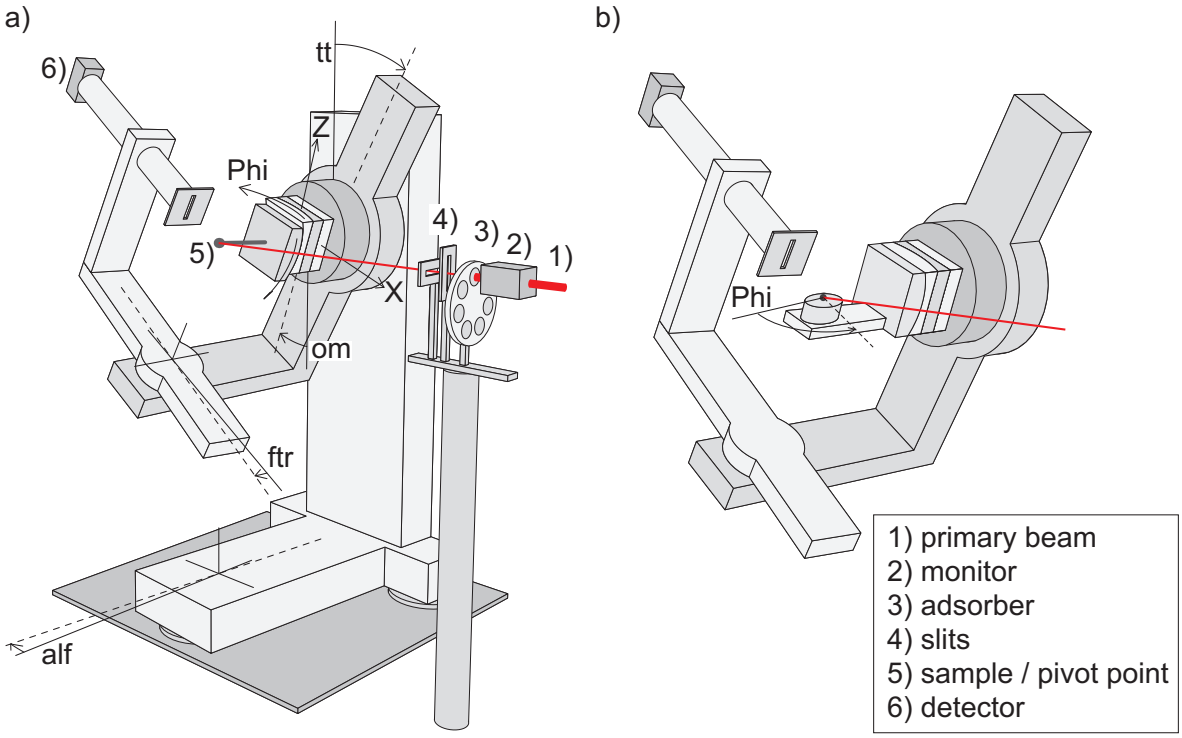

Figure 4.6: (a) Schematic setup of the identical six-circle diffractometers at beamlines W1 and BW2, image taken from reference [65] and edited. (b) Alternative diffractometer setup with additional motor to rotate the sample laterally (phi-angle).

refracted/reflected angle (tt) are varied. With this geometry XRR and XRD measurements are performed where the refracted/reflected angle is identical with the incident angle.

2. vertical alignment

   Here, the sample is mounted on the diffractometer with the surface perpendicular to the main rotation axis. The incident angle of the beam (alf) is adjusted before measurement and a small angle barely above the critical angle for total reflection is chosen. With this geometry, the specular rod is not accessible since the incident angle cannot be varied during measurement. The non-specular diffraction rods are, however, widely accessible due to the full rotation of sample and detector. Therefore, GIXRD measurements can be performed with this geometry.

3. horizontal alignment with additional phi-circle motor

   This alternative measurement geometry is similar to the horizontal alignment. Here, the sample is mounted on a motor, which offers additional lateral rotation of the sample (phi; cf. figure 4.6(b)). Therefore, it is possible to perform XRR, XRD and GIXRD measurements since both incident angle and lateral rotation of the sample can be varied

during measurement. This is favorable if many samples have to be measured because significant time can be saved during alignment.

For sample alignment, it is important to distinguish between reflectometry (XRR) and diffraction (XRD, GIXRD) measurements. On the one hand, reflection occurs at the interface between air and medium, which is defined by the topmost atoms and can be considered as the sample surface. On the other hand, diffraction is caused by the periodically arranged atoms and the reciprocal space is aligned to the crystal lattice. Since the samples exhibit a miscut of the substrate regarding the [111] direction, surface and crystal lattice are not necessarily parallel to each other (cf. figure 4.7). Therefore, reflectometry measurements have to be aligned to the actual surface whereas the diffraction measurements have to be aligned to the crystal planes.

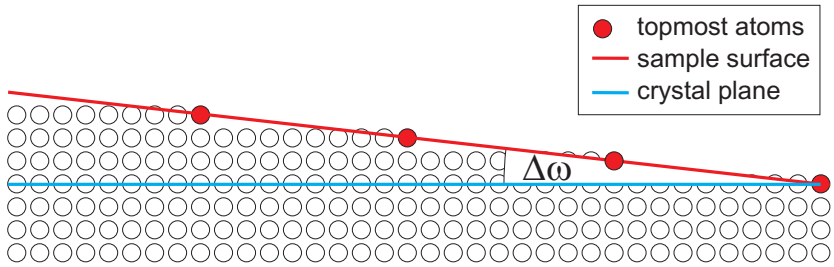

Figure 4.7: Comparison of sample surface and crystal planes. The angle $\Delta\omega$ between surface and planes is also called the miscut. In this thesis the samples exhibit a miscut of $(0.35 \pm 0.15)\,^{\circ}$.

4.5.2 Setup at beamline BW1

In contrast to the beamlines W1 and BW2, synchrotron radiation at BW1 is generated by an undulator. Here, the dipole magnets are arranged in such a way that the emitted X-ray radiation interferes coherently. Therefore, the intensity increases with the quadratic number of dipole magnets and a higher brilliance can be achieved compared to wiggler-generated X-ray radiation. Furthermore, the wavelength region of the X-ray photons is much sharper and it can be variated by the gap between the dipole magnets. However, double-crystal silicon monochromators are used as well to extract photons with certain energy. Both Si(111) and Si(220) monochromator crystals were used to offer a non-dispersive experimental setup, which suppresses signal broadening due to the wavelength broadening of the radiation source [66, 67]. Furthermore, the second crystal is cut asymmetrically to parallelize the beam by minimizing the beam divergence and a motor controlled slit system can be used to adjust the size of the beam at the sample to suppress undesired background signal from the sample holder.

Photons with energies of about 2.40 keV (5.18 Å) and 3.35 keV (3.70 Å) were used to generate the X-ray standing wave fields at the position of the sample which is fixed during the measurements. Small energy variations, necessary to scan through the Bragg diffraction conditions

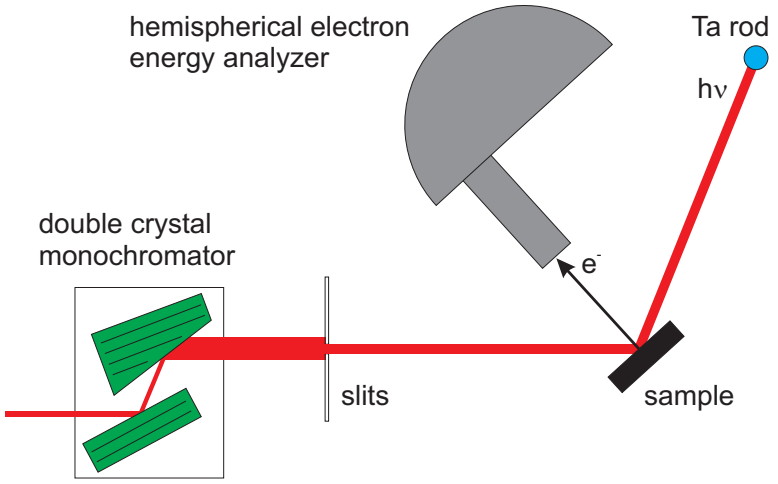

Figure 4.8: Schematical experimental setup at the beamline BW1.

and therefore to move the minima and maxima of the standing wave fields (cf. chapter 2.6.1), are performed by tilting the double crystal monochromator. The diffracted X-ray intensity during the scans through the BRAGG condition (*rocking curve*) is measured by a tantalum rod where a photo current is induced depending on the diffracted beam intensity. The photo electrons emitted from the sample are detected by a hemispherical electron analyzer (CLAM 100). Here, the energies of the emitted electrons can be discriminated.

4.6 ReflexFit - a general purpose spot profile analysis tool

ReflexFit is a useful program with graphical user interface (GUI) to analyze spot profiles. It was developed by the author [68] and further improved in the context of this thesis. Here, *ReflexFit* was used for the analysis of both SPA-LEED and XRD reciprocal space mappings. The GUI is presented in figure 4.9 by way of illustration.

The user analyzes spot profiles by fitting the measured data with up to five linearly connected GAUSSIAN or LORENTZIAN functions. For this, a set of parameters for each function is defined by the user to describe briefly the measured intensity distribution. Both function types are determined by intensity, FWHM, peak position and exponent. The transition from LORENTZIAN to GAUSSIAN function is achieved by choosing a large exponent ($> 1,5$). This means basically the larger the exponent the preciser the GAUSSIAN function is approximated. Finally, a linear background can be added to the functions.

The data is fitted by varying the parameter set using a NELDER-MEAD-SIMPLEX method [69]. Thus, various parameters can be fixed and the fitted region of the data can be chosen freely. An adjustable error function was implemented, which offers the possibility to favor low or high intensity regions during data fitting. Therefore, a mean absolute error (MAE) interacting with linear or logarithmic data was chosen, whereas the weighting between linear and logarithmic data is freely adjustable. Furthermore, the MAE function is favorable, since noised parts of the data are less incorporated during fitting. Important parameters are illustrated by several

graphic displays to give an overview about the fitting process.

A main advantage of *ReflexFit* is that a whole series of measurements consisting of hundreds of spot profiles can be fitted successively based on one predefined parameter set. This starting parameters are used to fit the first spot profile and the resulting set of parameters is further used to fit the second spot profile and so on. Since the spot profiles mainly undergo little changes from one measurement to the next, a reasonable fitting of the data is possible with this strategy.

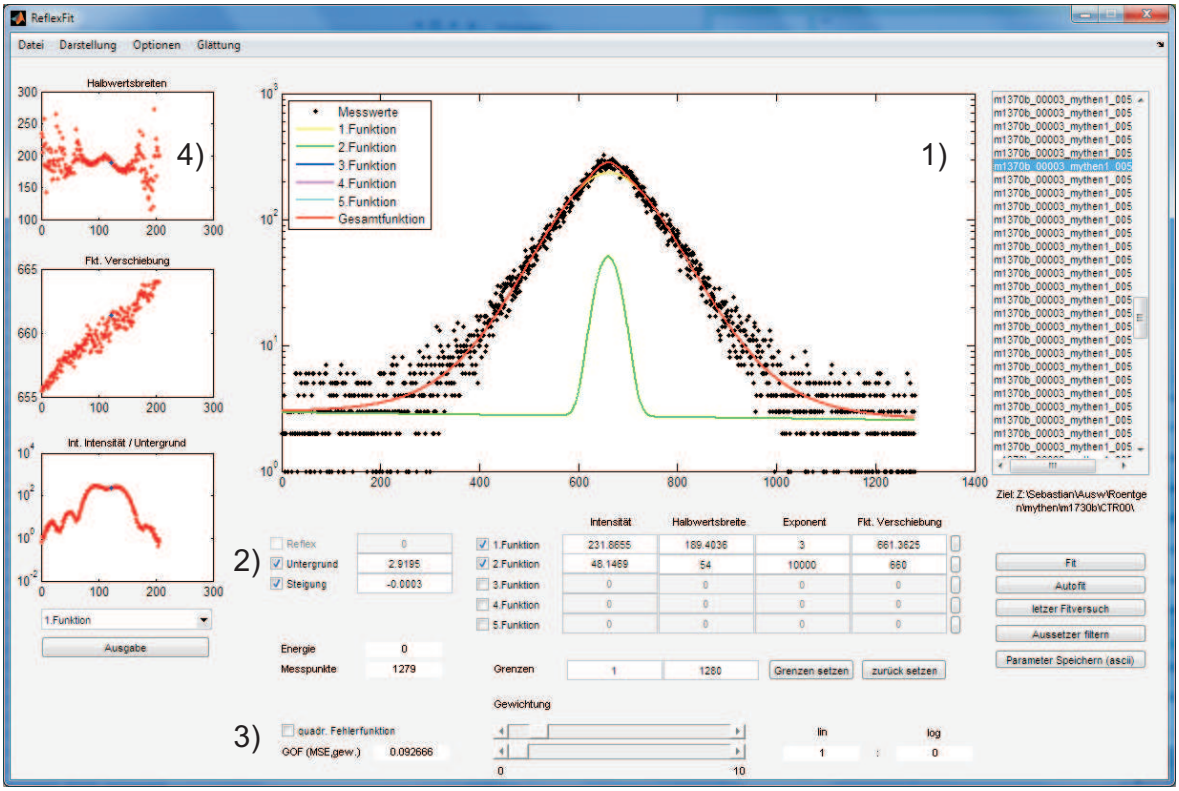

Figure 4.9: Graphical user interface of *ReflexFit*. The important components are the illustration of measured and fitted data (1), the input area for the parameter set (2), the area to adjust the error function (3) and the graphical displays for the parameters (4).

4.7 Analysis tools for X-ray diffraction and X-ray reflectivity measurements

Two other programs, which were also used to analyze the data presented in this thesis are briefly introduced in the following.

To analyze the obtained XRD and GIXRD measurements, a tool called *RodsNPlots* was used. This tool is based on a program developed by Carsten Deiter [70] and was developed and improved by Andreas Greuling and Susanne Hahne [71, 72]. *RodsNPlots* calculates the

intensity distribution of a sample caused by XRD at user defined multi-film-structure models. A model is based on a number of freely chosen crystalline films on a crystalline substrate. These structures are defined by several structure and morphology parameters as film thickness, filling factor, unit cell stretch factor, distance between the crystalline films, adsorption place as well as top and bottom rms-roughness. Furthermore, each film structure can be divided laterally into a free number of columns to model laterally coexisting species, as it is also necessary for the praseodymia films studied in this thesis [47, 11].

The calculated intensity distributions are fitted to the measured data by varying the set of parameters by different algorithms within pre-specified variation limits [71, 70]. Certain parameters and parameter limits can be coupled to handle more complex models in a limited amount of time and to reproduce natural dependencies. In this context the top roughness of one film is for example depending on the bottom roughness of the film below if the films are directly connected without an amorphous interface between them.

iXRR is a GUI based tool to calculate intensity distributions caused by XRR at multi-film-structure models. It is based on the program *RodsNPlots* mentioned above and was also developed in our work group [30]. Similar to *RodsNPlots* the model is based on several different films on a substrate, which can also be divided into laterally separated columns. It is, however, immaterial if the films are crystalline or amorphous. Each film is defined by the refractive index containing the variables *delta* and *beta* (cf. chapter 2.5.1), the layer thickness and the interface roughness at the top of the layer. To match the experimental data, the parameters are varied in the same way as in RodsNPlots regarding variation limits and fitting algorithms. A coupling of parameters or variation limits is, however, not possible.

5 Qualifying the scientific context

The presented thesis contains mainly three parts. The annealing of preoxidized praseodymia films on Si(111), the generation and investigation of praseodymia films with the highest and the lowest oxidation state and the growth of crystalline praseodymia films on passivated Si(111). Obviously, these topics are not directly associated with each other. Therefore, it makes sense to give a detailed classification of the parts with respect to the scientific context.

First investigations on the PDA of hex-Pr_2O_3 films on Si(111) in 1 atm oxygen were performed by Thomas Weisemoeller [11, 47]. One of the main goals was to obtain fully oxidized PrO_2 films with high quality. As mentioned in chapter 1, these films could be for example used as buffer layers to grow crystalline Ge films with low defect density on top [73, 16]. Furthermore, they can be used for applications in heterogeneous catalysis [8].

However, in both applications it is necessary to heat the praseodymia silicon system either to achieve *crystalline* Ge film growth [16] or to actuate the desired reactions [74, 75]. Here, information about structural changes, phase transitions and stability of the praseodymia films are very important in order to control the quality of the films grown on top of the praseodymia layers or to regulate the catalytic reactions and further to avoid the decomposition of these films during PDA treatment.

Therefore, studies on the PDA of preoxidized praseodymia films on Si(111) are presented in the first part of the thesis to get information about the behaviour of the Si-Pr system during further thermal treatment. First, an overview on the temperature region of room temperature up to 600°C is given, where structural changes of the oxide film and surface as well as the film stability are in the focus. Afterwards, a closer examination of the temperature region between RT and 300°C is presented to shed light upon phase transitions, which occur during thermal treatment. Furthermore, a first approach to identify particular oxidation states during PDA is presented. This is necessary to determine and control the amount of oxygen and oxygen vacancies within the praseodymia film which is of special interest for catalytic applications.

The second part of the thesis deals with the formation of praseodymia films on Si(111) with the highest and the lowest oxidation state. In the work of Thomas Weisemoeller [11, 47] it was already implied that PDA in 1 atm oxygen is not sufficient to obtain fully oxidized PrO_2 films. This becomes more obvious in the first part of the presented thesis. Nevertheless, it is useful to obtain homogeneous and fully oxidized films since, on the one hand, more mobile oxygen can be provided for catalytic applications, and on the other hand these praseodymia films exhibit crystallites with slightly different oxygen content and structure properties, which may cause defects at the interface between praseodymia and germanium in particular at the grain boundaries. Therefore, an alternative technique was developed by Andreas Schaefer et al. to further oxidize the praseodymia films with oxygen plasma treatment [76]. A summary of this work and the obtained results is given before a sophisticated analysis performed by the author of the presented thesis is shown. Here, the film structure is determined by detailed XRD analysis within the kinematic theory supported by XRR measurements.

The formation of praseodymia films with the lowest oxidation state (cub-Pr_2O_3) by annealing of hex-Pr_2O_3 films in 1 atm nitrogen and subsequent annealing in UHV was originally performed in the context of general structural stability of praseodymia films during thermal

treatment. However, these films and especially their surface structure are also interesting for the growth of self-assembled Ge nanocrystals to study the fundamentals of nanocrystal based nonvolatile memory effects [77].

These results are also interesting future studies to prepare the basis for the precise determination of the POISSON ratio of praseodymia which is up to now *assumed* to be 1/3 [11, 78]. The POISSON ratio is necessary to indirectly determine the oxygen content of the oxide species within thin praseodymia films by comparison of the unit cell sizes with values obtained from standard literature [79]. The reason for this is the tetragonal distortion of the oxide films grown on Si(111) as it is shown in the first part of the results. However, the oxygen content also influences the size of the unit cells and it is necessary to generate praseodymia films with a certain oxygen content to calculate the influence of the tetragonal distortion more precisely and with it the POISSON ratio. The easiest way is to generate praseodymia films with the highest or lowest oxygen content since these films mark the boundaries in the phase diagramm. As is shown in the presented thesis and in former work [47] praseodymia films tend to form laterally coexisting oxide species with different oxygen content. However, fully oxidized or reduced praseodymia films necessarily exhibit only one particular oxygen content and a homogeneous film structure which can be easily verified with XRD and GIXRD measurements. Since the oxygen content is known in these cases, the POISSON ratio can be precisely determined. Furthermore, if this is done for the highest and the lowest oxidation state, a dependency of the POISSON on the oxygen content can also be detected. However, in this thesis only vertical lattice parameters where determined for structural analysis of the films with the highest and the lowest oxidation state. Since also lateral lattice constants are necessary to precisely calculate the POISSON ratio this cannot be done in the presented thesis.

The third part is about crystalline praseodymia films grown on passivated Si(111) substrates, which is one approach to suppress amorphous interface formation between oxide film and substrate. These amorphous silicate interfaces always occur during PDA of praseodymia films in oxygen or nitrogen atmosphere [47, 80]. It was further shown that growth of ultrathin crystalline films ($< 10\,\mathrm{nm}$) on Si(111) with low deposition rates is impossible due to the formation of Pr-silicates and Pr-silicides during the evaporation process [45]. Finally, as it can be seen in the first part of the presented results, the existing interface thickness increases with further thermal treatment under UHV conditions [19] and it was also shown that even the whole film can be consumed during PDA of the sample [48]. This is a main problem in catalytic reactions, where several heating processes are applied to the catalytic material, which causes a successive decrease of the catalytically active oxide layer. Therefore, film growth on chlorine passivated substrates to suppress the formation of an amorphous interface is presented in the third part of this thesis.

For this purpose, praseodymia films where grown on passivated and non-passivated silicon substrates with low deposition rates since here, the difference between the samples regarding crystalline quality and interface thickness are very large and can easily be shown. In the first place, the validation of *crystalline* praseodymia film growth on passivated substrates is shown in the results, which can be seen as a basic research to get information about the manageability of crystalline film growth and to get the general evaporation parameters. This can be used further for systematical studies to improve the film quality.

Original publication: Journal of Physics: Condensed Matter **21**, 175408 (2009)
available at `http://dx.doi.org/10.1088/0953-8984/21/17/175408`

Structural phase transition of ultra thin PrO_2 films on Si(111)

S. Gevers*, T. Weisemoeller*, B. Zimmermann*, F. Bertram*, C. Deiter*, J. Wollschläger*, [1]

* *Department of Physics, University of Osnabrück, Barbarastrasse 7, D-49069 Osnabrück, Germany*

[1]Electronic mail: joachim.wollschlaeger@uos.de

Original publication: Journal of Physics: Condensed Matter **23** 115904 (2011)
available at http://dx.doi.org/10.1088/0953-8984/23/11/115904

Post deposition annealing of praseodymia films on Si(111) at low temperatures

S. Gevers*, T. Weisemoeller*, D. Bruns*, A. Giussani**, T. Schroeder** and J. Wollschläger* [2]

* *Department of Physics, University of Osnabrück, Barbarastrasse 7, D-49069 Osnabrück, Germany*
** *IHP, Im Technologiepark 25, 15236 Frankfurt (Oder), Germany*

[2]Electronic mail: joachim.wollschlaeger@uos.de

Original publication: Physica status solidi (c) **7**, 292 (2010)
available at `http://dx.doi.org/10.1002/pssc.200982406`

Structure and stability of cub-Pr_2O_3 films on Si(111) under post deposition annealing conditions

S. Gevers*, T. Weisemoeller*, B. Zimmermann*, C. Deiter*, J. Wollschläger*, [3]

* *Department of Physics, University of Osnabrück, Barbarastrasse 7, D-49069 Osnabrück, Germany*

[3]Electronic mail: joachim.wollschlaeger@uos.de

9 Oxygen plasma-treated praseodymia films: Previous results

The structural analysis of oxygen plasma-treated praseodymia films on Si(111) with XRR and XRD will be discussed in the following chapter. These results are based on the work of Andreas Schaefer, who applied the oxygen plasma treatment technique (cf. chapter 4.2) on praseodymia films. Afterwards, he characterized these films with XPS and LEED, which was accompanied by a first analysis of XRD measurements performed by the author of the presented thesis [76]. A brief summary of these results is given in the following.

The praseodymia films on Si(111) were prepared at the IHP GmbH according to the recipe presented in chapter 4.1 and sent afterwards to the IACP in Bremen. Here, the samples were examined by XPS before and after oxygen plasma treatment. The XPS spectra of the untreated samples showed that the surface of the praseodymia film is significantly contaminated with carbon, carbonates and Pr-hydroxides. After oxygen plasma treatment, no carbon compounds could be detected at the surface any longer and the amount of Pr-hydroxides was considerably lower. The O 1s spectrum of the XPS measurement exhibited a small shift to lower binding energies pointing to a higher oxidation state of the oxide film.

The Pr 3d spectrum showed additional interesting features after oxygen plasma treatment. The untreated samples exhibited a spectrum comparable to PrO_2 reference spectra obtained by XPS measurements on praseodymia powder pellets [81, 82]. Furthermore, a significant increase of the signal induced by Pr^{4+} ions could be observed. This also points to an increased oxidation state of the praseodymia films, because the incorporation of additional oxygen into the Pr-O system is always accompanied by the formation of Pr^{4+} ions.

Structural analysis by LEED and XRD also verifies the higher oxidation state of the plasma-treated samples compared to the samples which were oxidized by PDA in 1 atm oxygen. For the first time a (1x1) surface unit cell with three fold symmetry could be observed in the LEED patterns which is expected for the cubic PrO_2 structure. First analysis of the XRD measurements showed a shift of the vertical lattice parameters of all oxide species within the praseodymia film to lower values. This is caused by the formation of Pr^{4+} ions which have a smaller ionic radius than Pr^{3+} ions. After plasma treatment all resulting vertical lattice parameters are close to the expected value for tetragonally distorted PrO_2. This shows that the plasma-treated samples are considerable higher oxidized compared to the samples annealed in 1 atm oxygen. A detailed description of these results can be found in reference [76].

A more precise analysis of the XRD measurements using calculations of the intensity distributions within the kinematic diffraction theory are shown in the following. These studies are also supported by additional XRR measurements, which results in a more precise structure model of the plasma-treated samples compared to the first analysis.

Original publication: Physical Review B: Brief Reports **83**, 193408 (2011)
available at `http://link.aps.org/doi/10.1103/PhysRevB.83.193408`

Structure of oxygen plasma treated ultra-thin praseodymia films on Si(111)

S. Gevers*, T. Weisemoeller*, A. Schaefer**, V. Zielasek**, M. Bäumer**, and J. Wollschläger* [4]

* *Fachbereich Physik, University of Osnabrück and Center of Interface Science, Barbarastrasse 7, D-49069 Osnabrück, Germany*
** *Institute of Applied and Physical Chemistry, University of Bremen, Leobener Str. NW2, D-28359 Bremen, Germany*
*** *Institute of Solid State Physics, University of Bremen, Otto-Hahn-Allee 1, D-28359 Bremen, Germany*

[4]Electronic mail: joachim.wollschlaeger@uos.de

Original publication: Applied Physics Letters **97**, 242901 (2010)
available at `http://dx.doi.org/10.1063/1.3525175`

Improved epitaxy of ultrathin praseodymia films on chlorine passivated Si(111) reducing silicate interface formation

S. Gevers*, J. I. Flege**, B. Kaemena**, D. Bruns*, T. Weisemoeller*, J. Falta**, and J. Wollschläger* [5]

* *Department of Physics, University of Osnabrück, Barbarastrasse 7, D-49069 Osnabrück, Germany*
** *Institute of Solid State Physics, University of Bremen, Otto-Hahn-Allee 1, D-28359 Bremen, Germany*

[5]Electronic mail: joachim.wollschlaeger@uos.de

12 Summary and Outlook

The main results obtained from the presented thesis are summarized in the following chapter. Afterwards, an outlook on further investigations, which are useful in the context of these results, is given.

The first part of the thesis deals with PDA of praseodymia films with fluorite structure under UHV conditions in the temperature region from RT to 600°C. Here, a sophisticated model of the annealing process of praseodymia films is established. This is done by detailed analysis of XRD measurements using the kinematic diffraction theory in combination with the analysis of GIXRD, XRR and SPA-LEED measurements. It is shown that the untreated films, which are oxidized in 1 atm oxygen to obtain fluorite structure, do not exhibit pure PrO_2 stoichiometry as it was assumed before. Instead, they decompose into two laterally coexisting species exhibiting a PrO_2 and a $PrO_{1.833}$ oxide phase, respectively. These species are laterally pinned to the lattice parameter of bulk $PrO_{1.833}$. Homogeneous oxide films with $PrO_{1.833}$ phase can be observed after annealing at 100°C and 150°C. Here, lateral strain caused by the pinning of the species is minimized and an increase of the crystallite sizes is determined. If higher annealing temperatures are applied, the film decomposes again into two coexisting species. Finally, after annealing at 300°C, a mixed crystalline film with both $PrO_{1.5}$ and $PrO_{1.5+\Delta}$ oxide phases is formed, where Δ denotes a considerable excess of oxygen within the sesquioxide phase. Again the lateral strain increases due to the tendency of praseodymia phases to increase their lattice parameters during oxygen loss combined with the lateral pinning. This is accompanied by a decrease of crystallite sizes, which are afterwards comparable to those of the untreated films. Further annealing at temperatures above 300°C does not significantly change the structure of the oxide film. However, the increase of the amorphous Pr-silicate interface between Si substrate and oxide at the expense of the crystalline oxide can be observed after annealing at higher temperatures. Furthermore, an increased mosaic spread of the crystallites occurs, which reduces the lateral strain caused by the oxygen loss. Nevertheless, the crystalline structure is stable against further annealing up to temperatures of 600°C. Transportation of the sample under ambient conditions after annealing at 200°C and 300°C leads to the formation of an additional crystalline structure at the surface which cannot be allocated to any praseodymia phase and may be explained by the contamination of the topmost crystalline layers with Pr-hydroxides.

The results obtained from praseodymia films annealed in 1 atm nitrogen show that these films are good candidates to form homogeneous oxide films with pure cub-Pr_2O_3 structure by subsequent annealing in UHV. Here, a single oxide species is already observed after annealing at 300 °C by SPA-LEED measurements which is in contrast to praseodymia films with fluorite structure where higher annealing temperatures (600 °C) are necessary. In this case, negative effects like interface growth or increased defect density (mosaics, grain boundaries) can be minimized. This is advantageous for further applications like the growth of self assembled Ge nano dots.

Investigations on oxygen plasma-treated praseodymia films to obtain pure PrO_2 stoichiometry are presented in the second part. Oxygen plasma-treated samples are compared with samples oxidized in 1 atm oxygen regarding the structure of the crystalline film. For this purpose,

XRR and XRD measurements are performed to get structural information of the oxide film, which can be used to identify the corresponding oxide phases. Here, significantly smaller lattice constants of the crystalline oxide species can be observed after plasma treatment, which points to the incorporation of additional oxygen atoms. This verifies former studies, where a higher oxidation state of the oxide film was found by XPS measurements and it shows that plasma-treated films exhibit a higher oxidation state than films oxidized in 1 atm oxygen due to the availability of reactive atomic oxygen in the plasma. Furthermore, the Pr-silicate interface between crystalline film and Si substrate is not increased during plasma treatment. Although a small part at the bottom of the film still exhibits $PrO_{1.833}$ structure, the results indicate that this new technique is very promising to obtain praseodymia films with homogeneous fluorite structure and higher quality compared to other methods.

In the last part of the presented thesis, first results from the epitaxy of praseodymia films on Cl-passivated Si substrates are shown. The aim is to suppress the Pr-silicate formation during the growth process. Thus, praseodymia films are grown on passivated and non-passivated substrates to compare the crystallinity of both samples using XSW and LEED measurements. The structure of the oxide films on Cl-passivated Si is determined afterwards by XRR. It is shown that crystalline films with cub-Pr_2O_3 structure and several nanometer thickness can be successfully grown on Cl-passivated substrates. Here, the Pr-silicate interface layer are restricted to a single mono-layer. In contrast, the films grown on non-passivated substrates are completely amorphous containing Pr-silicates and Pr-silicides. This shows that the new method is promising to improve the quality of praseodymia films on Si substrates.

It should be mentioned that the obtained results denote the current state of knowledge within the presented investigations. Therefore, an outlook on further studies is given in the following.

Regarding the PDA process of praseodymia films in UHV, in-situ XRD, GIXRD and XRR measurements are key techniques to get a more precise view on the structural properties of the oxide films during the annealing process. This is because smaller temperature steps can be used since the data is obtained directly during PDA. Furthermore, the influence of sample transportation under ambient conditions, which is still not fully understood, can be excluded. Finally, a single sample can be used for the temperature dependent measurements instead of one sample for each annealing step. Therefore, uncertainties caused by small deviations of the oxide film properties (e.g. the film thickness) are also excluded, which may occur since the samples are cut from different parts of a wafer. In doing so, the oxygen content of the praseodymia films during PDA can be determined with higher precision than it is done up to now.

For the oxygen plasma-treated samples, a detailed analysis of additional, non-specular CTRs is necessary to determine the influence of the plasma treatment on the lateral lattice constants to get information about the unit cell volume and lateral strain effects. Furthermore, the reciprocal space mappings can be analyzed with regard to mosaic spread and crystallite sizes. These additional results are important to complete the knowledge about the influence of plasma treatment on the structure and morphology of the oxide films.

The oxygen plasma-treated praseodymia films as well as the oxide films annealed in nitrogen can be used to precisely determine the Poisson ratio as mentioned in chapter 5. The reason for this is the homogeneity of these films, which indicates that they are indeed in the highest

and the lowest oxidation state.

The results from praseodymia film epitaxy on Cl-passivated substrates showed that the growth of oxide films with crystalline quality and suppressed interface formation is possible. Here, reactive epitaxy of praseodymium in oxygen atmosphere is of advantage, since the properties of the grown praseodymia films are strongly influenced by the availability of oxygen during film growth. Direct control of this parameter may be important to further improve the quality of the oxide film. Moreover, passivation of the surface with boron instead of chlorine atoms might be useful since B-passivated surfaces are more stable against thermal treatment compared to surfaces passivated with Cl atoms [50]. Therefore, the B atoms may not segregate to the surface during praseodymia film growth as it is shown for Cl atoms.

Bibliography

[1] J. Kwo, M. Hong, B. Busch, D. A. Muller, Y. J. Chabal, A. R. Kortan, J. P. Mannaerts, B. Yang, P. Ye, H. Gossmann, A. M. Sergent, K. K. Ng, J. Bude, W. H. Schulte, E. Garfunkel, and T. Gustafsson. Advances in high κ gate dielectrics for Si and III-V semiconductors. *J. Cryst. Growth*, 251(1-4):645, 2003. Proceedings of the Twelfth International Conference on Molecular Beam Epitaxy.

[2] D. T. Bowron, G. A. Saunders, R. J. Newport, B. D. Rainford, and H. B. Senin. EXAFS studies of rare-earth metaphosphate glasses. *Phys. Rev. B*, 53(9):5268, 1996.

[3] S.K. Bhaskaran and V.T. Bhat. Catalytic activity of CeO_2 and Pr_2O_3 for the liquid-phase benzylation of o-xylene to 3,4 – dimethyldiphenylmethane. *React. Kinet. Catal. Lett.*, 75:239, 2002.

[4] R. D. Köhn, Z. Pan, J. Sun, and C. Liang. Ring-opening polymerization of $_D$, $_L$ -lactide with bis(trimethyl triazacyclohexane) praseodymium triflate. *Catal. Commun.*, 4(1):33, 2003.

[5] Y. Takasu, M. Matsui, H. Tamura, S. Kawamura, Y. Matsuda, and I. Toyoshima. Temperature-programmed desorption on the unstable lattice oxygen of praseodymium oxide. *J. Catal.*, 69:51–57, 1981.

[6] Y. Takasu, M. Matsui, and Y. Matsuda. The catalytic contribution of the lattice oxygen atoms of praseodymium oxide to the oxidation of carbon monoxide. *J. Catal.*, 76:61–64, 1982.

[7] K. Otsuka and M. Kunitomi. Direct participation of lattice oxygen atoms in catalytic oxidation of carbon monoxide over praseodymium oxides. *J. Catal.*, 105:525, 1987.

[8] G. V. Antoshin, K. M. Minachev, and D. R. Dmitriev. Mobility of oxygen and catalytic properties of rare earth oxides with respect to oxidation of hydrogen. *Russ. Chem. Bull.*, 16:1793, 1967.

[9] T. Schroeder, P. Zaumseil, G. Weidner, G. Lupina, Ch. Wenger, H.-J. Müssig, and P. Storck. Structure, twinning behavior, and interface composition of epitaxial Si(111) films on hex-Pr_2O_3(0001)/Si(111) support systems. *J. Appl. Phys.*, 98(12):123513, 2005.

[10] T. Schroeder, P. Zaumseil, G. Weidner, Ch. Wenger, J. Dabrowski, H.-J. Müssig, and P. Storck. On the epitaxy of twin-free cubic (111) praseodymium sesquioxide films on Si(111). *J. Appl. Phys.*, 99(1):014101, 2006.

[11] T. Weisemoeller, C. Deiter, F. Bertram, S. Gevers, A. Giussani, P. Zaumseil, T. Schroeder, and J. Wollschlaeger. Epitaxy of single crystalline PrO_2 films on Si(111). *Appl. Phys. Lett.*, 93(3):032905, 2008.

[12] T. Schroeder, A. Giussani, J. Dabrowski, P. Zaumseil, H.-J. Müssig, O. Seifarth, and P. Storck. Engineered Si wafers: On the role of oxide heterostructures as buffers for the integration of alternative semiconductors. *Phys. Status Solidi C*, 6(3):653–662, 2009.

[13] S.W. Bedell, A. Reznicek, K. Fogel, J. Ott, and D.K. Sadana. Strain and lattice engineering for Ge FET devices. *Mater. Sci. Semicond. Process.*, 9:423, 2006.

[14] H. Tanoto, S. F. Yoon, W. K. Loke, E. A. Fitzgerald, C. Dohrman, B. Narayanan, M. T. Doan, and C. H. Tung. Growth of GaAs on vicinal Ge surface using low-temperature migration-enhanced epitaxy. *J. Vac. Sci. Technol.*, 24:152, 2006.

[15] A. M. Gaffney, C. A. Jones, J. J. Leonard, and J. A. Sofranko. Oxidative coupling of methane over sodium promoted praseodymium oxide. *Journal of Catalysis*, 114(2):422, 1988.

[16] A. Giussani, P. Rodenbach, P. Zaumseil, J. Dabrowski, R. Kurps, G. Weidner, H.-J. Muessig, P. Storck, J. Wollschlaeger, and T. Schroeder. Atomically smooth and single crystalline Ge(111)/cubic-Pr2O3(111)/Si(111) heterostructures: Structural and chemical composition study. *J. Appl. Phys.*, 105(3):033512, 2009.

[17] P. Sonström, J. Birkenstock, Y. Borchert, L. Schilinsky, P. Behrend, K. Gries, K. Müller, A. Rosenauer, and M. Bäumer. Nanostructured praseodymium oxide: Correlation between phase transitions and catalytic activity. *ChemCatChem*, 2:694–704, 2010.

[18] O. Seifarth, Ch. Walczyk, G. Lupina, J. Dabrowski, P. Zaumseil, G. Weidner, H-J. Müssig, and T. Schroeder. Dielectric properties of single crystalline PrO_2(111) / Si(111) heterostructures: Amorphous interface and electrical instabilities. *J. Appl. Phys.*, 106:104105, 2009.

[19] S. Gevers, T. Weisemoeller, B. Zimmermann, F. Bertram, C. Deiter, and J. Wollschlaeger. Structural phase transition of ultra thin PrO_2 films on Si(111). *J. Phys.: Condens. Matter*, 21(17):175408, 2009.

[20] E. A. Wood. Vocabulary of surface crystallography. *J. Appl. Phys.*, 35:1306, 1964.

[21] Jr. Strozier, J.A., D.W. Jepsen, and F. Jona. *Surface Physics of Materials*, chapter Surface Crystallography, pages 1–77. Academic Press, 1975.

[22] A. J. C. Wilson and V. Geist. *International Tables for Crystallography*. Kluwer Academic Publishers, Dordrecht/Boston/London, 1992.

[23] T. Schmidt. *Strukturelle Untersuchungen zur homoepitaxie auf Pt(111)*. PhD thesis, University of Hannover, 1994.

[24] M. Horn von Hoegen. Growth of semiconductor layers studied by spot profile analysing low energy electron diffraction. *Kristallogr.*, 214:1–75, 1999.

[25] C.S. Lent and P.I. Cohen. Diffraction from stepped surfaces. *Surface Science*, 139:121–154, 1984.

[26] J. Wollschläger. *Ordnungsvorgänge in einatomaren Metallschichten auf hochindizierten Metallschichten*. PhD thesis, University of Hannover, 1990.

[27] M. Born and E. Wolf. *Principles of Optics*. Pergamon, Oxford (1993), 1993.

[28] L. G. Parratt. Surface studies of solids by total refelection of X-Rays. *Physical Review*, 95(2):359, 1954.

[29] M. Tolan. *X-ray Scattering from Soft-Matter Thin Films, Materials Science and Basic Research*. Springer, 1998.

[30] F. Bertram. Röntgenreflektometrie an ultradünnen Schichten, 2007. Bachelor thesis.

[31] L. Névot and P. Croce. Charactization of surfaces by grazing X-ray reflection. Application to the study of polishing some silicate glasses. *Revue de Physique Appliquee*, 15(3):761, 1980.

[32] J. Zegenhagen, G. Materlik, and W. Uelhoff. X-ray standing wave analysis of highly perfect Cu crystals and electrodeposited submonolayers of Cd and Tl on Cu surfaces. *J. X-Ray Sci. Technol.*, 2:214, 1990.

[33] M. P. Seah and W. A. Dench. Quantitative electron spectroscopy of surfaces: A standard data base for electron inelastic mean free paths in solids. *Surf. Interface Anal.*, 1:2–11, 1979.

[34] H. Lüth. *Surfaces and Interface of Solid Materials*. Springer-Verlag Berlin Heidelberg New York, third edition edition, 1998.

[35] M. Räkers. An X-ray spectroscopic study of novel materials for electronic applications, 2009. PhD thesis.

[36] D. Haneman. Surfaces of silicon. *Rep. Prof. Phys.*, 50:1045–1086, 1987.

[37] K. Takayanagi, Y. Tanishiro, and M.Takahashi. Structure analysis of Si(111)-7x7 reconstructed surface by transmission electron diffraction. *Surf. Sci.*, 164:367, 1985.

[38] G. Binnig, Ch. Rohrer, and E. Weibel. 7 x 7 Reconstruction on Si(111) Resolved in Real Space. *Phys. Rev. Let.*, 50:120–125, 1983.

[39] G. Adachi and N. Imanaka. The binary rare earth oxides. *Chem. Rev.*, 98:1479, 1998.

[40] L. Gmelin. *Handbook of Inorganic and Organometallic Chemistry*. Verlag Chemie, Berlin, 8 edition, 1993.

[41] C. N. R. Rao and B. Raveau. *Transition Metal Oxides*. Wiley-VCH, New York, 1998.

[42] B. G. Hyde, D. J. M. Bevan, and L. Eyring. On the Praseodymium+Oxygen System. *Philosophical Transactions of the Royal Society of London. Series A, Mathematical and Physical Sciences*, 259(1106):583, 1966.

[43] V. S. Rudenko and A. G. Boganov. Reduction cycle $MO_2 \rightarrow M_2O_3$ for cerium, praseodymium, and terium oxides. *Inorg. Mater. (USSR) (Engl. Transl.)*, 7:98, 1971.

[44] T. Schroeder, T.-L. Lee, L. Libralesso, I. Joumard, J. Zegenhagen, P. Zaumseil, C. Wenger, G. Lupina, G. Lippert, J. Dabrowski, and H.-J. Müssig. Structure and strain relaxation mechanisms of ultrathin epitaxial Pr_2O_3 films on Si(111). *J. Appl. Phys.*, 97(7):074906, 2005.

[45] A. Schaefer, V. Zielasek, Th. Schmidt, A. Sandell, M. Schowalter, O. Seifarth, L. E. Walle, Ch. Schulz, J. Wollschläger, T. Schroeder, A. Rosenauer, J. Falta, and M. Bäumer. Growth of praseod oxide on Si(111) under oxygen-deficient conditions. *Phys. Rev. B.*, 80:045414, 2009.

[46] J. P. Liu, P. Zaumseil, E. Bugiel, and H. J. Osten. Epitaxial growth of Pr_2O_3 on Si(111) and the observation of a hexagonal to cubic phase transition during postgrowth N_2 annealing. *Appl. Phys. Lett.*, 79:671, 2001.

[47] T. Weisemoeller, F. Bertram, S. Gevers, A. Greuling, C. Deiter, H. Tobergte, M. Neumann, J. Wollschläger, A. Giussani, and T. Schroeder. Postdeposition annealing induced transition from hexagonal Pr_2O_3 to cubic PrO_2 films on Si(111). *J. Appl. Phys.*, 105(12):124108, 2009.

[48] A. Sakai, S. Sakashita, M. Sakashita, Y. Yasuda, S. Zaima, and S. Miyazaki. Praseodymium silicate formed by postdeposition high-temperature annealing. *Appl. Phys. Lett.*, 85(22):5322, 2004.

[49] H. Ono and T. Katsumata. Interfacial reactions between thin rare-earth-metal oxide films and Si substrates. *Appl. Phys. Lett.*, 78(13):1832, 2001.

[50] V. G. Lifshits, A. A. Saranin, and A. V. Zotov. *Surface Phases on Silicon.* John Wiley & Sons, New York, 1994.

[51] J. J. Boland and J. S. Villarrubia. Identification of the products from the reaction of chlorine with the silicon(111)-(7x7) surface. *Science*, 840:838–840, 1990.

[52] J. V. Florio and W. D. Robertson. Chlorine reactions on the Si(111) surface. *Surf. Sci.*, 18:398–427, 1969.

[53] M. W. Radny, P. V. Smith, and P. L. Cao. An ab initio Hartree-Fock/density functional study of the simulated Si(111)7x7:Cl adsorption system. *Surf. Sci*, 365:15–28, 1996.

[54] A. Ricca and C. B. Musgrave. Theoretical study of the Cl-passivated Si(111) surface. *Surf. Sci*, 430:116–125, 1999.

[55] J. J. Boland and J. S. Villarrubia. Formation of Si(111)-(1x1)Cl. *Phy*, 41:9865–9870, 1990.

[56] N. Aoto, E. Ikawa, T. Kikkawa, and Y. Kurogi. Chlorine/silicon surface reactions under heating. *Surf. Sci*, 250:235–242, 1991.

[57] N. Aoto, E. Ikawa, T. Kikkawa, and Y. Kurogi. Influence of O_2 and oxide on Cl/Si surface reactions. *Surf. Sci*, 247:21, 1991.

[58] Thin Film Evaporation - Common Materials Reference and Guide. `http://ee.byu.edu/cleanroom/TFE_materials.phtml`, 17.06.2009.

[59] B. Gehl, U. Leist, V. Aleksandrovic, P. Nickut, V. Zielasek, H. Weller, K. Al-Shamery, and M. Bäumer. Design of a UHV-compatible rf plasma source and its application to self-assembled layers of CoPt3 nanoparticles. *Rev. Sci. Instrum.*, 77:083902, 2006.

[60] W. Kern. Purifying Si and SiO2 surfaces with hydrogen peroxide. *Semicond. Int.*, 7:294, 1984.

[61] U. Scheithauer, G. Meyer, and M. Henzler. A new LEED Instrument for Quantitative Spot Profile Analysis. *Surface Sciene*, 178:441–451, 1986.

[62] M. Henzler. Measurement of surface defects by low-energy electron diffraction. *Appl. Phys. A*, 34:205, 1984.

[63] J. Wollschläger, J. Falta, and M. Henzler. Electron diffraction at stepped homogeneous and inhomogeneous surfaces. *Appl. Phys. A*, 50:57, 1990.

[64] W. Caliebe, U. Brüggmann, M. Lohmann, and P. Machek. New Equipment at W1. Technical report, HASYLAB @ DESY, 2007.

[65] E. Fendt. Strukturuntersuchungen an dünnen Flüssigkeitsfilmen, 2003. Diplomarbeit.

[66] J. I. Flege. *Untersuchung der Photonen-stimulierten Desorption an Chlor auf Silizium(111) mit stehenden Röntgenwellenfeldern.* PhD thesis, Fachbereich Physik, Hamburg, 2000.

[67] T. Gog, A. Hille, D. Bahr, and G. Materlik. Dispersive X-ray standing waves measurements. *Rev. Sci. Instrum.*, 66:1522–1524, 1995.

[68] S. Gevers. SPA-LEED-Untersuchungen von Praseodymoxidschichten auf Si(111)-Substraten, 2007. Diplomarbeit.

[69] J. A. Nelder and R. Mead. A simplex method for function minimization. *Comp. Journal*, 7:308–313, 1965.

[70] C. Deiter. Röntgenstrukturanalyse von Halbleiter-Isolator-Schichtsystemen, 2005. PhD thesis.

[71] A. Greuling. Röntgenstrukturanalyse von Isolatorschichten, 2007. Master thesis.

[72] S. Hahne. Strukturanalyse von Praseodymoxidschichten mit Röntgenbeugung, 2008. Bachelor thesis.

[73] A. Giussani, O. Seifarth, P. Rodenbach, H.-J. Müssig, P. Zaumseil, T. Weisemoeller, C. Deiter, J. Wollschläger, P. Storck, and T. Schroeder. The influence of lattice oxygen on the initial growth behavior of heteroepitaxial Ge layers on single crystaline PrO_2(111)/Si(111) support systems. *J. Appl. Phys.*, 103(8):084110, 2008.

[74] K. Asami, K. Kusakabe, N. Ashi, and Y. Ohtsuka. Synthesis of ethane and ethylene from methane and carbon dioxide over praseodymium oxide catalysts. *Applied Catalysis A-General*, 156(1):43–56, AUG 14 1997.

[75] M. G. Poirier, R. Breault, S. Kaliaguine, and A. Adnot. Oxidative coupling of methane over praseodymium oxide catalysts. *Applied Catalysis*, 71:103–122, 1991.

[76] A. Schaefer, S. Gevers, V. Zielasek, T. Schroeder, J. Falta, J. Wollschläger, and M. Bäumer. Photoemission study of praseodymia in its highest oxidation state: The necessity of in situ plasma treatment. *J. Chem. Phys.*, accepted:n.a., 2010.

[77] T. Schroeder, I. Costina, A. Giussani, G. Weidner, O. Seifarth, Ch. Wenger, P. Zaumseil, C. Mocuta, T. H. Metzger, D. Geiger, and H. Lichte. Self-assembled Ge nanocrystals on high-k cubic Pr_2O_3 (111)/Si(111) support systems. *J. Appl. Phys.*, 102(3):034107, 2007.

[78] P. Zaumseil. X-ray measurement of the tetragonal distortion of the oxide buffer layer in Ge/Pr_2O_3/Si(111) heteroepitaxial structures. *J. Phys. D: Appl. Phys.*, 41(13):135308, 2008.

[79] W. Pies and A. Weiss. *Landolt-Börnstein - Group III Condensed Matter Numerical Data and Functional Relationships in Science and Technology. In: Crystal Structure Data of Inorganic Compounds*. Springer, 1975.

[80] S. Gevers, T. Weisemoeller, B. Zimmermann, C. Deiter, and J. Wollschläger. Structure and stability of cub-Pr_2O_3 films on Si(111) under post deposition annealing conditions. *Phys. Status Solidi C*, 7:292, 2010.

[81] A. Bianconi, A. Kotani, K. Okada, R. Giorgi, A. Gargano, A. Marcelli, and T. Miyahara. Many-body effects in praesodymium core-level spectroscopies of PrO_2. *Phys. Rev. B*, 38:3433–3437, 1988.

[82] S. Lütkehoff, M. Neumann, and A. Ślebarski. 3d and 4d x-ray-photoelectron spectra of Pr under gradual oxidation. *Phys. Rev. B*, 52(19):13808, 1995.

List of Figures

List of peer-reviewed publications

- T. Weisemoeller, C. Deiter, F. Bertram, S. Gevers, A. Giussani, P. Zaumseil, T. Schroeder, J. Wollschläger
  Epitaxy of single crystalline PrO_2 films on Si(111)
  Applied Physics Letters **93**, 032905 (2008).
  available at `http://dx.doi.org/10.1063/1.2958227`

- S. Gevers, T. Weisemoeller, B. Zimmermann, F. Bertram, C Deiter, J. Wollschläger
  Structural phase transition of ultra thin PrO_2 films on Si(111)
  Journal of Physics: Condensed Matter **21**, 175408 (2009).
  available at `http://dx.doi.org/10.1088/0953-8984/21/17/175408`

- T. Weisemoeller, F. Bertram, S. Gevers, C. Deiter, A. Greuling, J. Wollschläger
  Effect of amorphous interface layers on crystalline thin-film X-ray diffraction
  Physical Review B **79**, 245422 (2009).
  available at `http://dx.doi.org/10.1103/PhysRevB.79.245422`

- T. Weisemoeller, F. Bertram, S. Gevers, A. Greuling, C. Deiter, H. Tobergte, M. Neumann, A. Giussani, T. Schroeder, J. Wollschläger
  Post deposition annealing induced transition from hexagonal Pr_2O_3 to cubic PrO_2 films on Si(111)
  Journal of Applied Physics **105**, 124108 (2009).
  available at `http://dx.doi.org/10.1063/1.3152796`

- S. Gevers, T. Weisemoeller, B. Zimmermann, C. Deiter, J. Wollschläger
  Structure and stability of cub-Pr_2O_3 films on Si(111) under post deposition annealing conditions
  Phys. Status Solidi C **7**, 292 (2010).
  available at `http://dx.doi.org/10.1002/pssc.200982406`

- S. Gevers, J.I. Flege, B. Kaemena, D. Bruns, T. Weisemoeller, J. Falta, J. Wollschläger,
  Improved epitaxy of ultra-thin praseodymia films on chlorine passivated Si(111) reducing silicate interface formation
  Applied Physics Letters **97**, 242901 (2010).
  available at `http://dx.doi.org/10.1063/1.3525175`

- A. Schaefer, S. Gevers, V. Zielasek, T. Schroeder, J. Falta, J. Wollschläger, M. Bäumer
  Photoemission study of praseodymia in its highest oxidation state: the necessity of in situ plasma treatment
  Journal of Chemical Physics **134**, 054701 (2011).
  available at `http://dx.doi.org/10.1063/1.3516953`

- D. Bruns, S. Gevers, J. Wollschläger
  Formation and morphology of step-bunches during B-segregation on Si(111): A SPA-LEED survey

Surface Science **605**, 861 (2011).
available at http://dx.doi.org/10.1016/j.susc.2011.01.013

- J.I. Flege, B. Kaemena, S. Gevers, F. Bertram, T. Wilkens, D. Bruns, J. Wollschläger, J. Falta
Silicate-free growth of high-quality ultra-thin ceria films on Si(111)
Physical Review B: Rapid Communications (Submitted).

- S. Gevers, T. Weisemoeller, D. Bruns, A. Giussani, T. Schroeder and J. Wollschläger
Post deposition annealing of praseodymia films on Si(111) at low temperatures
Journal of Physics: Condensed Matter **23** 115904 (2011).
available at http://dx.doi.org/10.1088/0953-8984/23/11/115904

- S. Gevers, T. Weisemoeller, A. Schaefer, V. Zielasek, M. Bäumer, J. Falta, T. Schroeder, and J. Wollschläger
Structure of oxygen-plasma treated ultra thin praseodymia films on Si(111)
Physical Review B: Brief Reports **83** 193408 (2011).
available at http://link.aps.org/doi/10.1103/PhysRevB.83.193408

Acknowledgement

Finally, I would like to express my gratitude to those who supported me during the development of this thesis.

First of all, my thesis advisor Prof. Dr. Joachim Wollschläger should be mentioned, who was always willing to discuss experimental and technical problems, which occurred during my work. In all cases, his knowledge and good advise helped me to overcome this difficulties.

I would like to thank Prof. Dr. Michael Reichling for filling the role of the secondary advisor, which is always accompanied by a considerable effort of time.

I also acknowledge the Deutsche Forschungsgemeinschaft (DFG) via Graduate College 695 and its chair man apl. Prof. Dr. Klaus Betzler for financial support.

Many thanks to our cooperative partners, which contributed to the development of this thesis. They are namely Dr. Thomas Schröder and Alessandro Giussani from IHP for kindly providing the investigated samples. Dr. Andreas Schäfer from the workgroup of Prof. Dr. Marcus Bäumer from IHCP, who performed the oxygen-plasma treatment. Jan-Ingo Flege and Björn Kaemena from the workgroup of Prof. Dr. Jens Falta at the university of Bremen, who supported me during the measurements and analysis of the XSW data.

This thesis was also directly supported from various members of our workgroup. Here, Daniel Bruns, Nina Jeppesen and Alexander Knobeler should surely be mentioned, who promoted this thesis during their own complementary work. I also want to highlight the fruitful discussions I had with Thomas Weisemöller and Florian Bertram about the analysis and interpretation of XRR and XRD measurements as well as the technical support from Gregor Steinhoff.

For the great working atmosphere during my thesis I would like to thank the whole workgroup and all their members and ex-members. Here, I especially enjoyed my time with my office colleagues Daniel Bruns, Timo Kuschel and Martin Suendorf during several work and afterwork activities.

The last and innermost thanks go to my family and friends who supported me all the way during my thesis and beyond. I especially want to thank my wife and friend Tanja, who was always there to lift me up and to bear my bad moods. You gave me the will to finish this thesis.